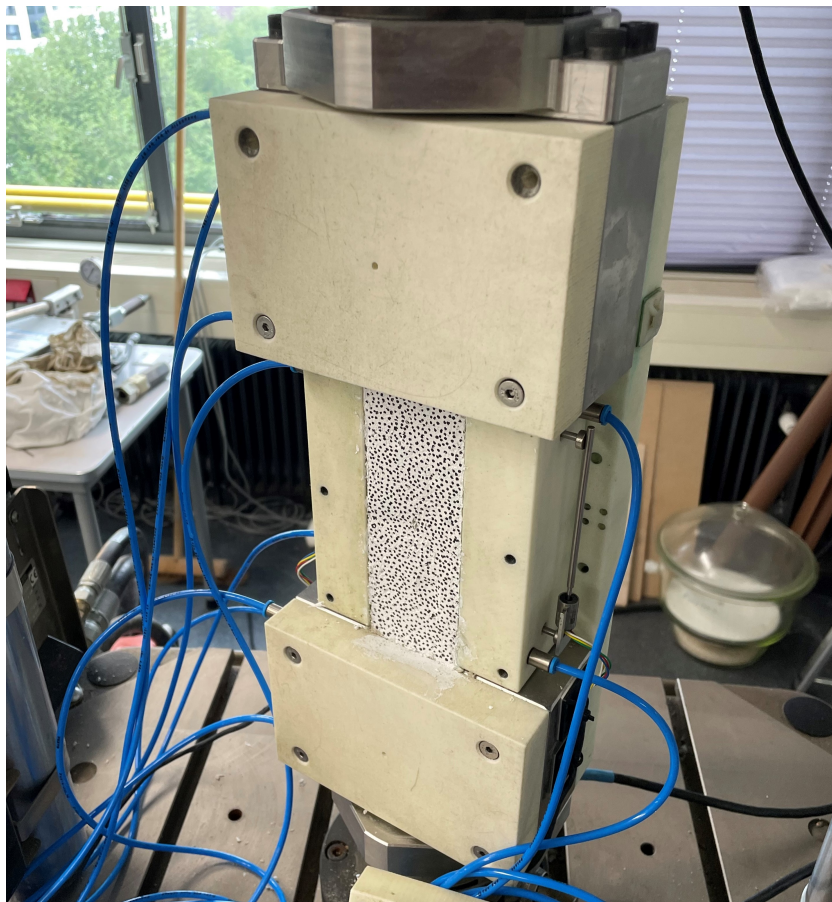# Crack Width of Reinforced Concrete under Combined Imposed Deformation and Mechanical Loading

by

F.N.A. van der Hoeven

to obtain the degree of Master of Science
at the Delft University of Technology,
to be defended publicly on Tuesday the 15th of October, 2024

Student number:	5113687	
Project duration:	February 12, 2024 – October 15, 2024	
Thesis committee:	Prof. dr. ir. E. Schlangen,	TU Delft, chair supervisor
	Dr. ir. M. Luković,	TU Delft, supervisor
	Ir. B. Albers,	BAM Infraconsult, supervisor
	Ir. W.J. van den Bos,	BAM Infraconsult, supervisor

TUDelft   **bam**

Abstract

Cracking in reinforced concrete structures can occur at any stage during their lifetime, and is anticipated for during its design. It is crucial to control crack widths by applying sufficient reinforcement to prevent impairments to the structure's functionality.

Cracks may develop due to external loads applied to the structure or due to imposed deformation. Imposed deformation occurs when movement is restrained, for example due to adjoining structures or internal thermal strain gradients in thick concrete sections. With the increased use of high-strength concrete since the late 20th century, autogenous shrinkage has emerged as a significant source of early-age cracking as well.

In practice, observed crack widths due to a combination of imposed deformation and mechanical loading during the early age of concrete are often smaller than predicted by structural design codes. This suggests that less reinforcement could be used in concrete structures, offering potential durability benefits. However, literature lacks sufficient validation of this observation, as well as an understanding of its origin and how it can be incorporated into design practices.

Liang (2024) developed a mini-TSTM specifically for plain mortar and validated its setup using results from the regular TSTM, which has been extensively documented in the literature. This setup allows for precise control over both deformation and temperature development and is integrated with an Instron loading machine. By restraining the mini-TSTM specimen during its early age, stresses due to autogenous shrinkage and thermal deformation are induced.

The following research question was explored: How do crack widths develop in reinforced concrete under the combination of imposed deformation and mechanical loading?

The first method used to answer this research question was to compare experimentally observed crack widths due to the combination of imposed deformation and mechanical loading to predictions from five structural design codes and guidelines.

Secondly, the impact of increasing the fraction of imposed deformation relative to mechanical loading on crack width in reinforced concrete was investigated.

Initially, the experimental setup and procedure, including reinforcement, were developed, followed by three experiments conducted at different times after the initial setting time and at various levels of imposed deformation. Using data from the Instron and a DIC analysis, experimental crack widths were obtained and compared to predictions from five structural design codes and guidelines.The optical microscope analysis provided further insights into crack locations.

Model Code 2010 proved to be the most accurate and consistent during the crack formation stage, while Van Breugel's method was most accurate and consistent during the stabilized cracking stage. Crack widths due to the combination of loading is generally overestimated by the design codes and guidelines, highlighting the importance of understanding their underlying principles and theories for accurate predictions.

There appears to be a trend indicating that an increase in the fraction of imposed deformation relative to mechanical loading results in a decrease in the final crack width in reinforced concrete. However, the varying weighted maturities across experiments also influence the predicted crack widths, making it difficult to confirm this hypothesis with certainty.

The development of the reinforced mini-TSTM experimental setup opens up new research opportunities. It significantly reduces the required workforce compared to the regular TSTM and, with the addition of the Instron, facilitates mechanical tensile testing of reinforced mortar.

Preface

This thesis is the culmination of my Master's studies in Structural Engineering at Delft University of Technology. The research presented here explores the behaviour of reinforced concrete structures subjected to imposed deformation and mechanical loading, with a particular focus on crack width prediction. This journey began with the development of a novel experimental setup, the reinforced mini-TSTM, which enabled a detailed investigation into structural behaviour under the combined loading.

Throughout this process, I have gained invaluable insights into both the theoretical and practical aspects of structural engineering and early age concrete. This work would not have been possible without the guidance and support of my supervisors: Erik Schlangen, Mladena Luković, Bas Albers, and Jeannette van den Bos, whose expertise and encouragement were instrumental in shaping this research. Erik and Bas provided invaluable support, meeting with me on a weekly basis and, during some periods, even daily. I always felt that my supervisors made time for me whenever I faced challenges or had difficult questions, and their guidance was instrumental in navigating these obstacles. I would also like to extend my gratitude to my colleagues of the Microlab, friends, and family for their unwavering support, especially during challenging periods when their motivation was incredibly valuable to me.

I would like to thank Shan He and Daan Exterkate for their assistance with the DIC analysis and Patrick Holthuizen for demonstrating the optical microscope to me. I am also grateful to Marique Ruijs of BAM for generously sharing her knowledge of concrete maturity and for patiently answering my questions. My thanks also go to Dautse Heimovaara of BAM for helping me with various questions during my thesis. My sincere gratitude goes to the technicians of the faculty, with special thanks to Maiko van Leeuwen and Kees van Beek. Maiko provided daily support as the supervisor of the Microlab, and Kees demonstrated inexhaustible dedication, fixing issues with the Instron and operating system—even during weekends. Kees' commitment was the reason I persevered with the experimental work rather than refocusing my research.

Finally, I am indebted to Minfei Liang, whose development and validation of the mini-TSTM during his PhD program laid the foundation for this research. Minfei's guidance during the initial months of this thesis was crucial to the work presented here and he kept in touch with me throughout the journey.

F.N.A. van der Hoeven
Delft, October 2024

Contents

1

Introduction

When concrete elements are cast, they undergo volumetric changes, mainly as a result of thermal deformations, self-desiccation and autogenous deformations (Liang, Luzio, et al., 2024; Lura, 2003). Thermal deformations are the result of the exothermic reaction between Portland cement and water and due to external factors in most instances. Temperature differentials during the early age of concrete result from the combined contributions of heat generated through cement hydration and heat dissipated to (or absorbed from) its surrounding. If the boundary conditions allow these structures to expand and shrink freely during its early age, no stresses will arise. However, when a concrete element is either externally or internally restrained during its early age, stresses will arise. The most common external restraint in concrete structures are adjoining structures, hindering the deformation of early age concrete. Internal restraints are common in concrete structures with relatively large dimensions. Fresh concrete near the surface loses heat more quickly than the core, creating an internal temperature gradient. This gradient induces strain differences, leading to both compressive and tensile stresses within the cross-section. While compressive stresses rarely exceed the concrete's strength during its early age without external loading, research indicates that when early-age loading exceeds 40% of the concrete's strength, significant deterioration in mechanical properties and increased porosity can occur (Xue et al., 2021).

Cracking during the early age of concrete is far more common and is a consequence of the tensile stresses exceeding the tensile strength. These excessive tensile stresses may arise due to improper curing leading to drying shrinkage. Another reason for early age cracking is restrained thermal deformation, either due to hydration of cement or external sources (Gribniak et al., 2013). Lastly, the introduction of high strength concrete in the last decades has led to the observation of more early age cracks. High strength concrete is obtained by filling the spaces between aggregates with cement and fillers, such as silica fume, and adding less water to the concrete mix design. The lack of water causes the inside of concrete to dry, which is called *self-desiccation* and this causes additional shrinkage. This additional shrinkage is the reason why this relatively novel type of concrete is more prone to early age cracking (Sule, 2003).

1.1. Problem statement

Cracks in concrete are not undesirable, quite the opposite in fact, as flexural members need to crack in order for the reinforcement to be activated and take up tensile stresses potentially exceeding the concrete tensile strength. However, crack widths should be controlled according to structural design codes for a number of reasons (CEN, 2005). EN1992-1-1:2004 states that cracks do not have to be limited, as long as the functioning of the structure is not impaired. In case that the functioning of the structure, its durability or the appearance is impaired, then cracking does have to be limited. It is still debatable whether the size of crack widths affect the durability of a structure. The study conducted by François and Arliguie (1999) showed that crack widths below 0.5 mm do not influence the development of corrosion of rebar. This study rather says, that microcracks occurring during the service loading

increases the chloride ion penetration, which decreases its service life. Schiessl and Raupach (1997) confirms this conclusion and states that the thickness and quality of the concrete cover influences corrosion rate more significantly.

It is however clear, that cracked concrete will result in earlier cracking of its cover induced by corrosion compared to uncracked concrete. This is because cracks cause the reinforcement to be directly exposed to the environment and thus increase the rate at which chlorides ingress the concrete and also promotes carbonation (Angst and Gehlen, 2019).

The discussion regarding the influence of crack widths on aesthetics and water tightness is relatively limited. It is generally agreed upon that larger cracks reduce the appearance of the concrete. Under uncracked conditions, the permeability of concrete is dependent on the porosity of the concrete. When concrete is cracked, the permeability is dependent on the crack characteristics. The flow rate is dependent on the cubed effective crack width, based on fluid mechanics and theory of compressible flow between two parallel and smooth surfaces. A reduction factor can be applied to achieve a more accurate flow through concrete cracks and depends on cross-section thickness and crack width (Edvardsen, 1996).

Calculating crack widths in reinforced concrete structures because of mechanical loading is generally well predictable and clearly formulated in structural design codes. However, crack width determination as a result of imposed deformation is less predictable and many researchers have, and are still analysing the behaviour of concrete under imposed deformation. According to van Breugel, temperature- and shrinkage-induced deformations are regarded as imposed deformations and often sudden and even gradual support settlements as well (van Breugel et al., 2011). Recent studies by Yilmaz and Cornelissen, along with an earlier but still relevant study by Sule, suggest that the field of structural engineering does not yet fully understand crack widths caused by imposed deformation (Yilmaz, 2022; Cornelissen, 2022; Sule, 2003). As a result of the unpredictable behaviour of crack widths due to imposed deformation, construction companies may apply conservative amounts of reinforcement to reduce them. Since structures are always subjected to mechanical loading as well, the combination of imposed deformation and mechanical loading is an interesting combination to study. Overestimation of crack widths will result in unnecessary costs and more importantly, it results in an excessive amount of steel usage and thus unnecessary burdening of the environment.

The goal of this research is to have a better understanding of the combination of imposed deformation and imposed loading on the crack widths in reinforced concrete structures. This will potentially result in more optimal material usage and this is desirable in the light of the European climate goals (European Council, 2024). In addition, the goal is to contribute to the understanding of imposed deformation and potentially create starting points for further research.

1.2. Research questions

The problem statement forms the basis for a set of research questions of which the answer should give more insight to cracking on reinforced concrete due to combined imposed deformation and mechanical loading. Since cracking due to imposed deformation is still unpredictable and structures may be subjected to a combination of imposed deformation and mechanical loading, the following main research question is formulated:

> *How do crack widths develop in reinforced concrete under the combination of imposed deformation and mechanical loading?*

Two research questions are formulated to address the main research question. The first research question focuses on the practical design of structures subjected to a combination of imposed deformation and mechanical loading. If structural codes and guidelines tend to consistently overestimate crack widths, it could suggest that less reinforcing steel is needed to meet crack width requirements. This leads to the first research question:

> *How do the crack width predictions of structural design codes and guidelines compare to experimentally observed crack widths due to the combination of imposed deformation and mechanical loading?*

The axial force caused by a restrained imposed deformation depends on the axial stiffness of the element (in case of an axially loaded element). A cracked reinforced concrete element will have a reduced stiffness compared to an uncracked one, therefore an equal amount imposed deformation will induce less force in a cracked element. For this reason, the fraction of load due to imposed deformation and mechanical loading is expected to partake in the cracking behaviour. The second research question is constructed as follows:

How does an increase in the fraction of imposed deformation relative to mechanical loading affect crack width in reinforced concrete?

The hypothesis is that an increase in the fraction of imposed deformation relative to mechanical loading leads to a reduction in crack width in reinforced concrete. The onset of cracking is supposed to relieve the load due to restrained imposed deformation and therefore result in smaller crack widths.

1.3. Research strategy
To address the research questions, a comprehensive strategy must be established. The primary objectives are to develop a better understanding of cracking behaviour under the combination of imposed deformation and mechanical loading.
Both the first and second research question, mentioned in subsection 1.2, can be answered performing a non-linear finite element analysis (NLFEA) or experimentally. For realism purposes, an experiment has a preference. Experiments can capture complex material behaviours and interactions, such as the actual cracking process, which might be difficult to fully model in FEA due to simplifications or assumptions. The cracking of reinforced concrete due to a combination of imposed deformation and mechanical loading is assumed to be complex, and an experiment can reveal this complex behaviour that might be hard to predict with models. Lastly, a NLFEA is preferred regarding the comparison of observed crack widths to the prediction of structural codes and guidelines. Performing experiments provides real-world data to compare directly with code predictions, while a model might still rely on assumptions that are aligned with the codes and guidelines.

The recent development of the mini Temperature Stress Testing Machine (mini-TSTM) by Liang (2024) is most convenient in order to answer the proposed research questions. Liang (2024) successfully created a significantly downsized version of the Temperature Stress Testing Machine and validated its results against the data obtained from the standard TSTM. Liang used the mini-TSTM to study the early age stress evolution in restrained high-volume ground granulated blast furnace slag concrete induced by autogenous deformation, among other things. The mini-TSTM is able to actively restrain mortar specimens and therefore stresses due to thermal and autogenous deformations occur. The mini-TSTM is housed within an Instron testing machine, facilitating the easy execution of mechanical tensile tests. In contrast, the workforce requirements of the standard TSTM make it unsuitable for this research, whereas the mini-TSTM can be operated independently.
Therefore, developing this setup and the associated procedures will be an integral part of this research before conducting the experiments to address the research questions. In these experiments, cracks due to restrained imposed deformation and mechanical loading will be induced. The fraction of imposed deformation stresses relative to mechanical load stresses can be accurately controlled using the mini-TSTM. The observed crack widths can then be compared to the predictions of structural codes and guidelines to assess their accuracy.

The theory of a tensile member under an axial load is prominently present in this research in order to understand cracking behaviour. The theory of the tensile member is extensively described in literature, such as by van der Veen (1990) and van Breugel et al. (2011). The tensile member model incorporates the concept of reduced stiffness resulting from crack formation in concrete. When an axial force causes the bar to enter either the crack formation stage or the stabilized cracking stage, the additional imposed deformation induces less stress due to the reduction of stiffness. However, if the sequence of loading is reversed, the theory predicts that the strain would not decrease; instead, the strains in the bar caused by both the imposed deformation and the imposed loading would be additive

(van Breugel et al., 2011). This thesis will investigate the validity of the latter prediction as part of the research questions.

1.4. Research structure

The thesis structure is organized around the two research questions, which have guided the chapter layout. The second chapter presents a literature review, providing the necessary background information to understand the principles underlying the mini-TSTM experiment and imposed deformation. Chapter three reviews five structural design codes and guidelines, highlighting their different approaches to predicting crack widths. Chapter four discusses the novel development of the reinforced mini-TSTM, including the experimental procedure. Chapter five presents the experimental results, including a crack width analysis and an overview of key time-dependent variables.

The subsequent chapters will present the conclusion, discussion, and recommendations for future research. A visualization of this research structure is depicted in the figure below:
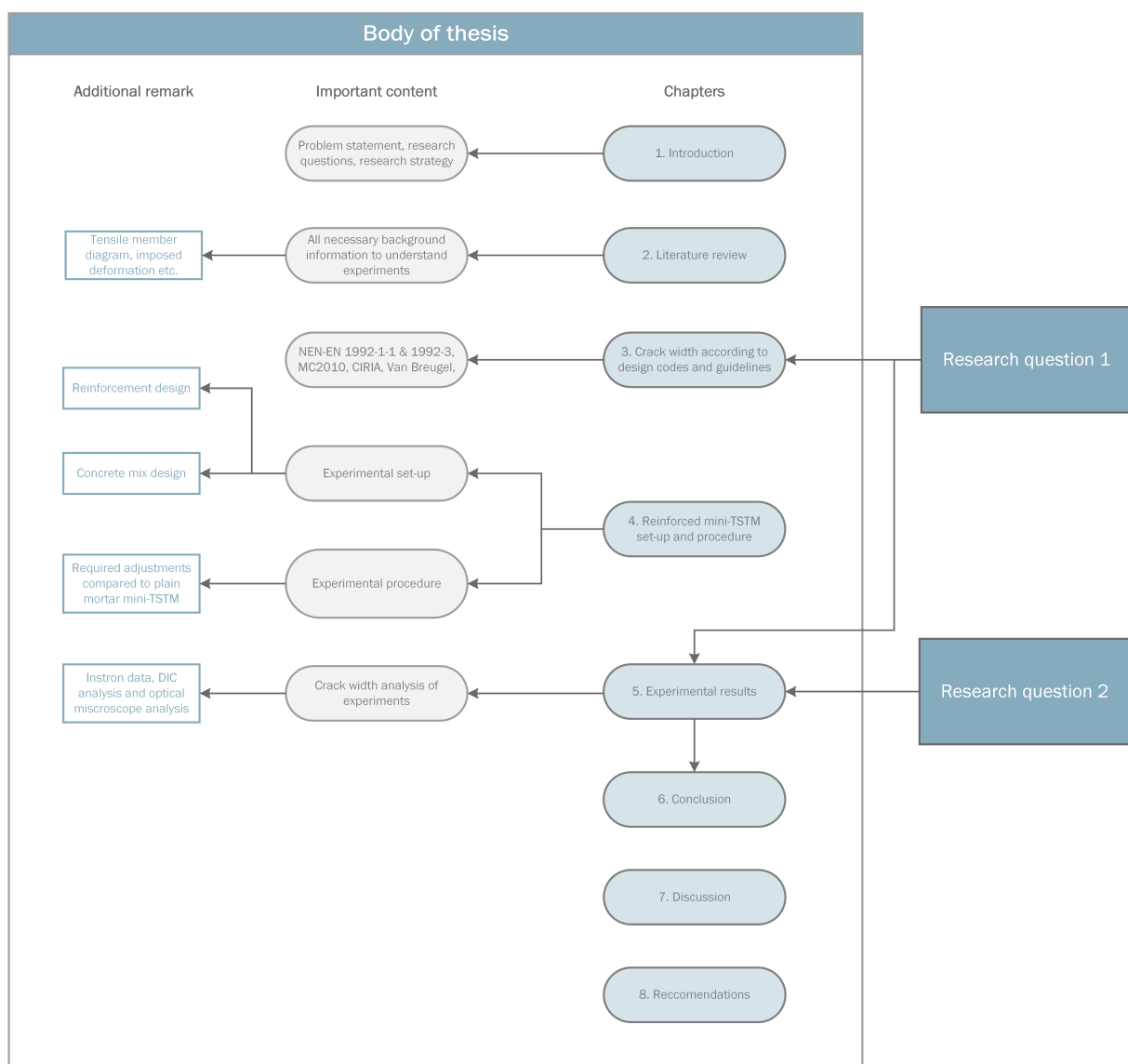
2

Literature review

This chapter describes the current state-of-the-art in the cracking behaviour of reinforced concrete under the combined effects of imposed and mechanical loading. Additionally, it presents relevant background theory necessary to understand the adopted research strategy and analyze the results.

The tensile member model, which describes the cracking behaviour of reinforced concrete, will be discussed first. Next, imposed deformation will be examined to understand how stresses occur without visible deformation of an element and how reinforcement affects this imposed deformation. The third section addresses the time-dependent behavior of concrete, explaining the phenomena that naturally cause concrete to undergo strain over its lifetime. The TSTM, designed in the late twentieth century to better understand the behaviour of early-age concrete, is the focus of the last section. This section also discusses the working principles of the TSTM and introduces its newly designed mini version.

2.1. Tensile member model

Crack widths in reinforced concrete in axially loaded members are described using the tensile member model. This model consists of a reinforced concrete beam which is axially loaded. The model is both valid for imposed deformations and imposed loads (van Breugel et al., 2011). The tensile member model describes the cracking behaviour of the reinforced concrete element and can be used to predict crack widths. The model can be distinguished using three phases, of which the last one can be subdivided into another two phases:

(1) Uncracked phase

(2) Crack formation phase

(3) Stabilized cracking phase

    I) Steel - elastic stage
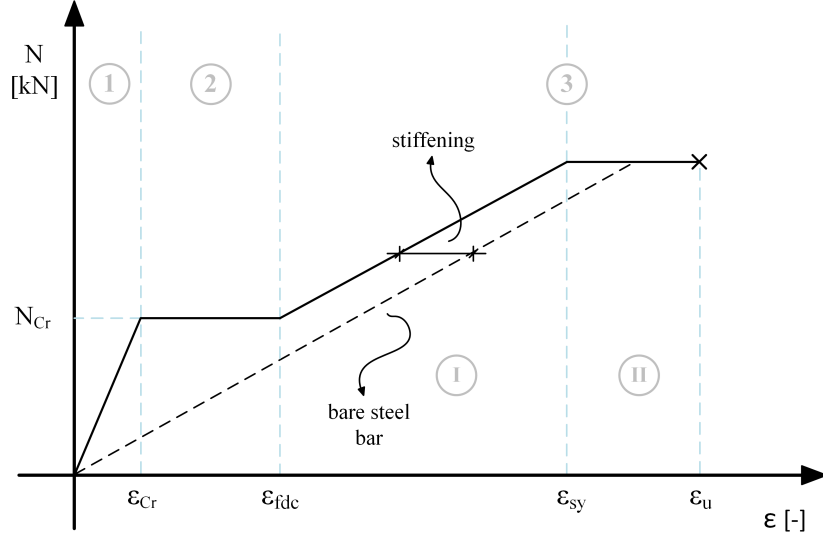   II) Steel - yielding

Figure 2.1: Simplified tensile member diagram

For the determination of crack widths in flexural elements, a hidden tensile member can be determined. Taking a beam for example, the hidden tensile member has a width equal to the width of the beam and an effective height depending on the reinforcement layout and geometry of the beam. This effective height resembles the height over which reinforcement is expected to take up tensile stresses in concrete. Three expressions to determine the effective height can be found in Eurocode 2. The tensile member model can be applied to the hidden tensile member is a flexural element.

Figure 2.1 shows the simplified tensile member diagram. During the first phase, the load and strain increase with a rate proportional to the Young's modulus of concrete. The strain in concrete and the strain in the reinforcing steel are equal in this phase:

$$\varepsilon_c = \varepsilon_s \tag{2.1}$$

The total force in the member equals the strain both the concrete and the reinforcing steel multiplied with their respective axial stiffnesses:

$$N = E_c A_c \varepsilon_c + E_s A_s \varepsilon_s \tag{2.2}$$

The axial force increases until the tensile strength of concrete is exceeded, which is throughout the whole member in the simplified model. In reality, the tensile strength is not constant throughout the member so the tensile strength will be exceeded at the weakest point of the member. Literature shows that this is typically at a capacity significantly lower than the mean tensile strength of concrete. As reported by van Breugel et al. (2011), the concrete stress at the occurrence of the first crack is equal to:

$$\sigma_{cr}(t) = 0.75 f_{ctm}(t) \tag{2.3}$$

The fully developed crack pattern is reached when no cracks are able to form anymore and this marks the third phase: the stabilized cracking phase. According to van der Veen (1990), the force at which the final crack occurs, is 20% larger than the cracking force at which the first crack is formed:

$$\sigma_{fdc}(t) = 1.20 * \sigma_{cr}(t) \tag{2.4}$$

Windisch (2021) describes that, in the case of uniform tensile strength along the length of a concrete element, an infinite number of cracks would form with infinitely small crack widths at infinitely small intervals. However, the tensile strength is not uniform along its length because of its non-homogeneity and geometric imperfections. Therefore, cracks are prone to occur at locations where it is weakest. Wu and Gilbert tested six reinforced concrete members under axial tension until failure. The obtained results indeed show that the load at the first crack is significantly lower than the at last crack, as seen

in figure 2.2. It is difficult to predict at what fraction of the mean tensile strength the specimens begin to crack, but it is evident that it is lower than exactly the mean tensile strength.

The second remark from this experiment, is the influence of time-dependent shrinkage on the cracking force. The specimens which were tested after shrinkage had occurred, cracked at a smaller imposed load than specimens loaded which were not subjected to significant shrinkage (Wu and Gilbert, 2008).
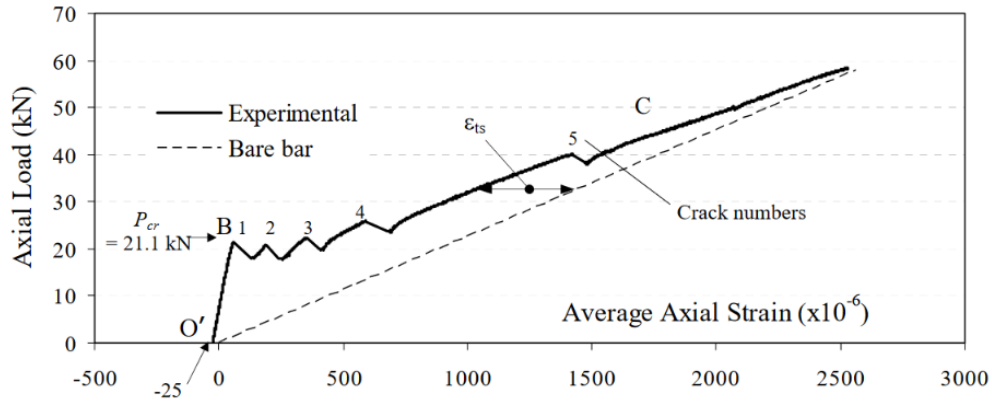
Figure 2.2: Experimental results of a reinforced concrete bar loaded under axial tension (Wu and Gilbert, 2008).

The strains and stresses during the crack formation phase are no longer equal throughout the length of the tensile member. At the location of the crack, the concrete stresses become zero and the surrounding reinforcing steel takes over these stresses. The length of steel which becomes active depends on the transfer length l_t. Figure 2.3 shows that the stresses change at the location of a crack compared to uncracked concrete.
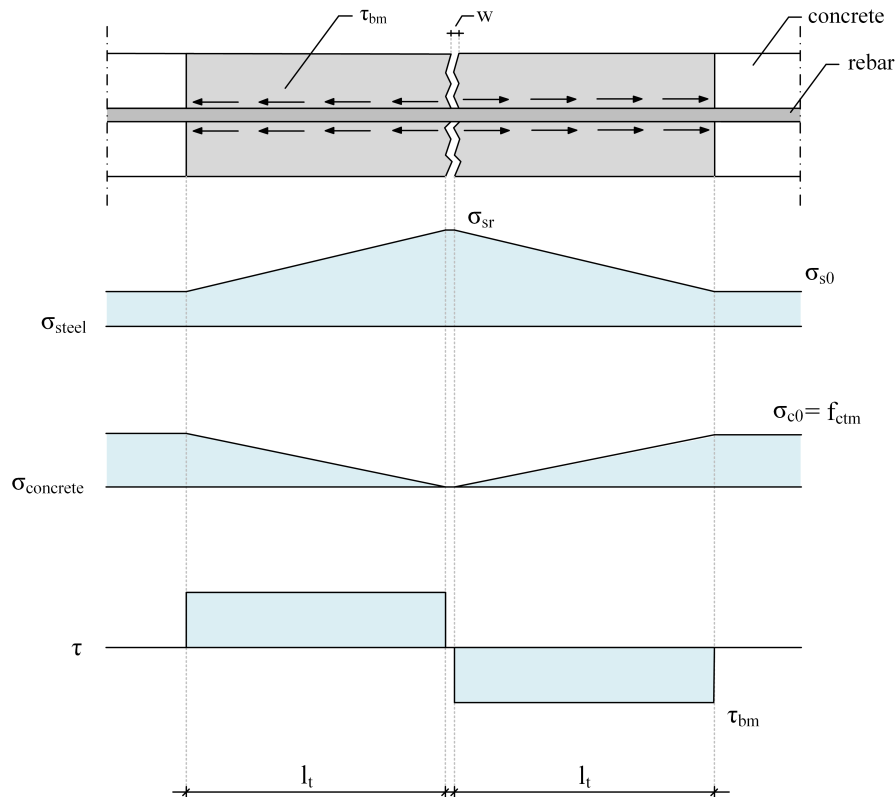
Figure 2.3: Stresses in concrete and reinforcing steel at the location of a crack

The area with distance l_t from the crack is the disturbed region, while uncracked concrete is undisturbed. The Euler-Bernoulli theorem only applies in the undistributed regions. The axial force at the cracking force, as stated in equation 2.2, can be rewritten knowing that the stress in concrete equals f_{ctm} and that the strain in concrete and steel is equal just before cracking. This yields the following equation:

$$N_{cr} = f_{ctm}A_c + \varepsilon_e E_s A_s$$

$$= f_{ctm}A_c(1 + \alpha_e \rho_s)$$

(2.5)

α_e in this equation is the ratio between the stiffness of steel and concrete and ρ_s equals the ratio between the area of steel and concrete. For a frequently used concrete class like C30/37 and a reinforcement ratio of 1.5%, classified as highly stressed concrete, the ratio $\alpha_e \rho_s$ equals 9.6% (CEN, 2005). According to equation 2.5, this indicates that the majority of the tensile force in the member, just before cracking, is carried by the concrete, with only a small portion borne by the reinforcement. Right after cracking, the cracking force is no longer carried by both concrete and steel, but rather by steel only. Using equation 2.2, the stress in the reinforcing steel right after cracking can be determined:

$$N_{cr} = f_{ctm}A_c + \varepsilon_e E_s A_s = A_s \sigma_{sr}$$

$$\sigma_{sr} = \frac{f_{ctm}}{\rho_s}(1 + \alpha_e \rho_s)$$

(2.6)

The stresses in the reinforcing steel get transferred from the concrete via the bond stresses induced by the ribs of reinforcing steel. These bond stresses are constant in figure 2.3 for simplification, but they behave non-linearly in reality. The transfer length can be determined knowing that the force in concrete is transferred to the reinforcing steel. The shear force delivered by the reinforcing steel equals its circumference multiplied with the transfer length times the bond stress:

$$l_t \tau_{bm} \pi \emptyset = A_c f_{ctm}$$

(2.7)

$$l_t = \frac{A_c f_{ctm}}{\tau_{bm} \pi \emptyset}$$

$$= \frac{f_{ctm}\emptyset}{4\tau_{bm}} * \frac{A_c}{A_s}$$

(2.8)

$$= \frac{f_{ctm}\emptyset}{4\tau_{bm}\rho}$$

The deformation of reinforcing steel is equal to the deformation of concrete plus the width of a crack. Based on this logic, the crack width can be determined analytically since the deformation is equal to the mean strain of each material times twice the transfer length.

$$\Delta_s = \Delta_c + w_{cr}$$

$$w_{cr} = (\varepsilon_{sm} - \varepsilon_{cm})2lt$$

(2.9)

The mean strain of concrete and steel can be determined using equation 2.3 and are equal to:

$$\varepsilon_{sm} = \frac{\sigma_{sr} + \sigma_{s0}}{2E_s}$$

(2.10)

$$\varepsilon_{cm} = \frac{\sigma_{c0}}{2E_c} \tag{2.11}$$

Combining the previous three equations yields the expression for the maximum crack width during the crack formation phase:

$$w_{max} = \frac{\sigma_{sr}}{E_s} * l_t$$

$$= \frac{f_{ctm}\emptyset\sigma_{sr}}{4\tau_{bm}\rho E_s} \tag{2.12}$$

The crack formation phase continues until no cracks are able to form in the concrete. This is determined by the length of the tensile member and the transfer length described in equation 2.8. Figure 2.4 shows the minimum and maximum amount of cracks possible, the distance between cracks varies between l_t and $2l_t$.
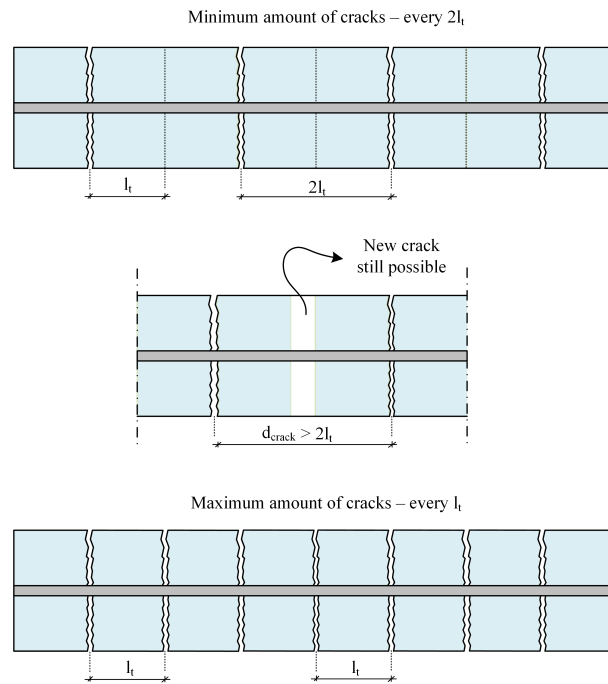
Figure 2.4: Minimum and maximum amount of possible cracks in a reinforced concrete member

If the tensile member is fully cracked, meaning that no other cracks can form, then the third stage commences: the stabilized cracking phase. No more cracks can form as there is no undisturbed region anymore, which is why existing cracks will widen with increasing force. An expression for the crack width in this phase is found by adding the increased steel strain to equation 2.12. The additional increase of steel stress is shown in figure 2.5. The crack width in this stage is equal to:

$$w_{max} = w_{fdc} + \Delta w \tag{2.13}$$

With Δw being the mean strain in steel due to a load $N > N_{cr}$ multiplied with the the disturbed length being $2lt$.

$$\Delta w = (\frac{\sigma_s - \sigma_{sr}}{E_s})2l_t \tag{2.14}$$

The expression for the crack width in the stabilized cracking formation can now be formulated.

$$w_{max} = \frac{\sigma_{sr}}{E_s} * l_t + \left(\frac{\sigma_s - \sigma_{sr}}{E_s}\right) * 2l_t$$

(2.15)

$$= \frac{1}{2} * \frac{f_{ctm}}{\tau_b} * \frac{\emptyset}{\rho} * \frac{1}{E_s} * (\sigma_s - 0.5\sigma_{sr})$$

A visualization of the increase of steel stress leading to an increased crack width is given in figure 2.5. The expression found in equation 2.14 is based on the principle of the reinforcing steel stress increasing in the stabilized cracking stage.
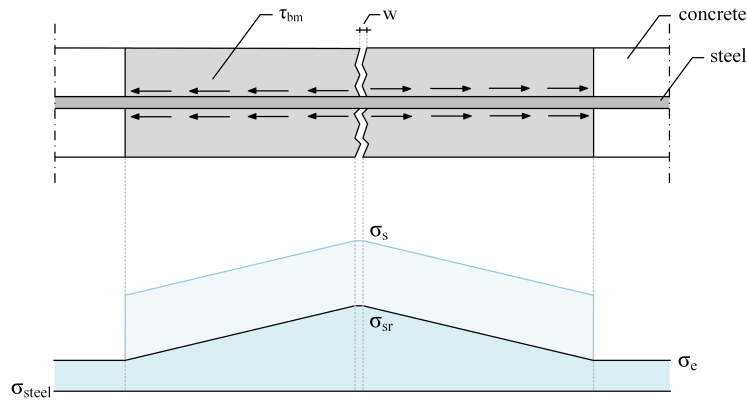
Figure 2.5: Increased steel stress in the stabilized cracking stage

2.2. Imposed deformation

Van Breugel states that the term "*imposed deformation*" leads to confusion and misunderstanding in practice and that a better term would be *"restrained deformation"* (van Breugel et al., 2011). As mentioned earlier, a common case of imposed deformation is because of adjoining structures hindering the deformation of a structure in between. First imagine a beam element, clamped on one side and free on the other side. This beam element is subjected to a temperature decrease ΔT. Due to this temperature decrease, the beam will shrink with an length increment equal to:

$$\Delta L(\Delta T) = \alpha_c \Delta T L \tag{2.16}$$

Now imagine the same beam subjected to a temperature decrease, but now being clamped on both ends. The beam tends to shrink, but is now restrained at both ends. A support reaction is introduced to keep the beam at its original position. The length increment due the temperature differential and due to the support reaction should be equal, resulting in the following support reaction:

$$\Delta L(\Delta T) + \Delta L(F) = 0$$

$$\alpha_c \Delta T L + \frac{FL}{EA} = 0 \tag{2.17}$$

$$F = -\alpha_c \Delta T E A$$
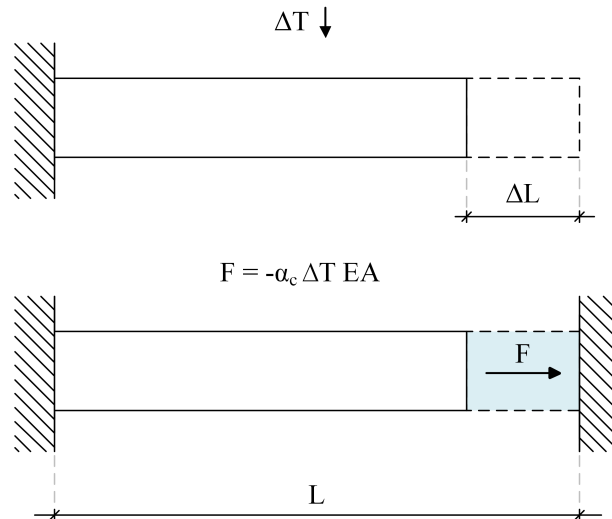
Figure 2.6: Force induced by a temperature differential on a clamped beam

No deformation is visible in the clamped beam, but there is an internal force present. When the beam tends to shrink, then the restoring force causes tensile stresses inside of the beam. And vice versa, when the beam tends to expand, then the restoring force causes compressive stresses in the beam. Reinhardt ([2014](#)) distinguishes three concrete phases: fresh state, young concrete and mature concrete. Concrete in fresh state can crack due to the surplus of water drying, causing water menisci between the cement, sand and aggregate particles. Capillary forces generated by these water menisci can exceed the tensile strength of concrete, leading to cracking. Therefore, curing fresh concrete is essential. Young concrete is especially vulnerable due to heat of hydration causing concrete to expand. When it cools down again, concrete will shrink. At the early stage of concrete, the Young's modulus is low and relaxation is significant which is why stresses are low. However, the stiffness increases after sometime and relaxation decreases as well and for that reason stresses will be significant and may exceed the tensile strength of concrete. The global development of stresses, temperature and tensile strength are depicted in figure 2.7.
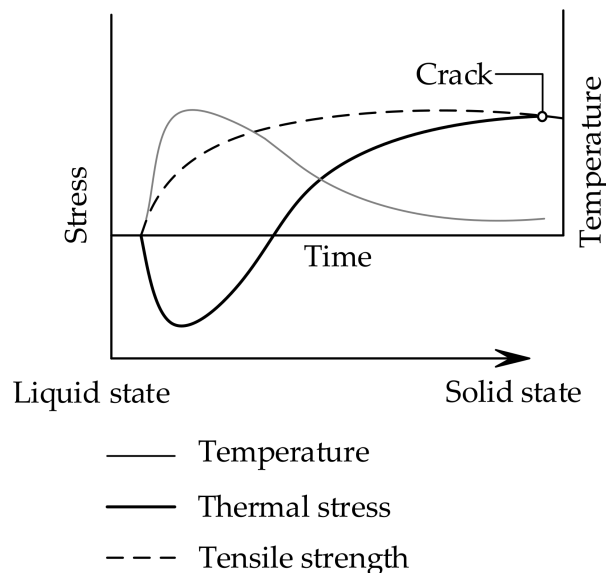
Figure 2.7: Global development of stresses, temperature and tensile strength of early age concrete (Liu et al., [2018](#)).

Mature concrete is not influenced by heat of hydration, but is subject to other influences causing imposed deformations. Examples are: temperature differentials, freezing of water and chemical reactions

such as alkali-silica reaction (ASR) and delayed ettringite formation (DEF). Cracking of restrained structures due to temperature differentials and autogenous shrinkage is common. Prestressing will introduce a negative strain to balance possible positive strains caused by imposed deformations. An increased amount of reinforcement will result in smaller crack widths as described in figure 2.1. Avoiding constrained boundaries, by adding joints at an appropriate spacing for example, is still the easiest way to avoid stresses in concrete due to imposed deformation (Reinhardt, 2014).

Externally unrestrained reinforced concrete elements will still experience imposed deformation as a result of reinforcing still restraining the free movement of concrete. According to Gribniak and Bacinskas, there are four main types of concrete shrinkage, namely: plastic shrinkage, autogenous shrinkage, carbonation shrinkage and drying shrinkage (Gribniak et al., 2008). As concrete tries to shrink, the reinforcing steel will resist this movement. Because of this, the reinforcement steel will be under compression while the concrete will experience tensile stresses. This is visually depicted in figure 2.8.
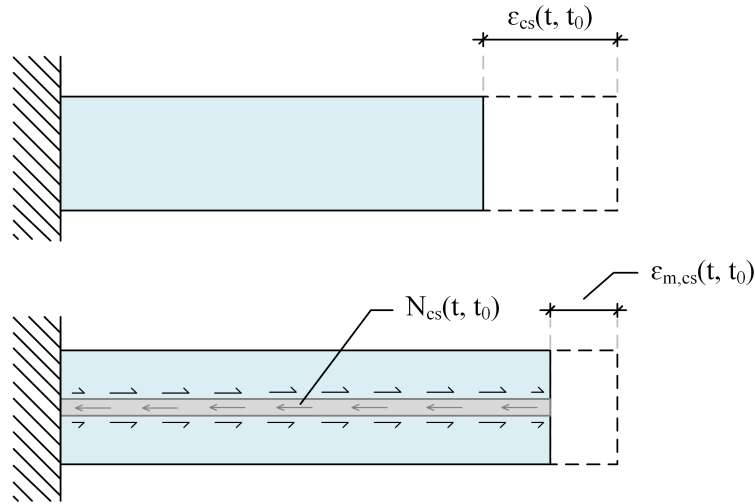
Figure 2.8: Reinforcing steel resisting the shrinkage of concrete

The beam on the top shows the strain of a plain concrete member subjected to shrinkage. The beam below includes reinforcement and this bar gives a restraint to longitudinal motion, which is why the strain of the reinforced member is smaller than the plain concrete member. Computing the strain of concrete is not as straightforward as computing the Young's modulus or strength development over time. There is an interdependence between stress and relaxation and the shrinkage strain is also time dependent. Computing strain under varying stress can be performed using the Trost-Bazant method. This method introduces two time dependent coefficients, namely $\chi(t, t_0)$ and $\phi(t, t_0)$. These are the ageing coefficient and creep factor respectively. The ageing coefficient is included as a gradually applied stress $\Delta\sigma_c(t, t_0)$ will cause less strain than the same amount of stress being applied constantly from t_0 until t. For a non-cracked member with zero initial stress at time t_0, the following strain in concrete is present:

$$\varepsilon(t, t_0) = \frac{\Delta\sigma_c(t, t_0)}{E_c(t_0)} + \frac{\Delta\sigma_c(t, t_0)}{E_c(t_0)}\chi(t, t_0)\phi(t, t_0) + \varepsilon_{cs}(t, t_0) \tag{2.18}$$

In this equation, $E_c(t_0)$ is the modulus of elasticity at time t_0 and $\varepsilon_{cs}(t, t_0)$ is the shrinkage strain of concrete. Equation 2.18 can be simplified using the definition of the age-adjusted effective modulus of elasticity $E''(t, t_0)$ as defined by Bazant (1972).

$$\varepsilon(t, t_0) = \frac{\Delta\sigma_c(t, t_0)}{E_c''(t_0)} + \varepsilon_{cs}(t, t_0) \tag{2.19}$$

The age-adjusted effective modulus of elasticity, present in equation 2.19, is defined as follows:

$$E_c''(t, t_0) = \frac{E(t_0)}{1 + \chi(t, t_0)\phi(t, t_0)} \tag{2.20}$$

In order to get to an expression for the strain as a function of time for the reinforced member, the fictitious axial force $N_{cs}(t, t_0)$ has to be defined, as shown in figure 2.8. This fictitious axial force is required to impose an axial strain $\varepsilon_{cs}(t, t_0)$ to a plain concrete member.

$$N_{cs}(t, t_0) = \varepsilon_{cs}(t, t_0) E_c''(t, t_0) A_c \tag{2.21}$$

The net section of concrete, meaning the area of concrete that remains after subtracting the area of reinforcing steel from the total area, is denoted by A_c. The expression for $\varepsilon_{m,cs}(t, t_0)$, the shrinkage strain including the action between concrete and steel as seen in figure 2.8, is stated below (Gribniak et al., 2008):

$$
\begin{aligned}
\varepsilon_{m,cs}(t, t_0) &= \frac{N_{cs}(t, t_0)}{E_c''(t, t_0) A_c + E_s A_s} \\[2mm]
&= \frac{\varepsilon_{cs}(t, t_0) E_c''(t, t_0) A_c}{E_c''(t, t_0) A_c + E_s A_s} \\[2mm]
&= \frac{\varepsilon_{cs}(t, t_0)}{1 + n(t, t_0) \rho_s}
\end{aligned}
\tag{2.22}
$$

The ratio between the Young's modulus of steel and the age-adjusted effective Young's modulus is denoted by $n(t, t_0)$ and the ratio between the area of steel and concrete is denoted by ρ_s:

$$n(t, t_0) = \frac{E_s}{E_c''(t, t_0)} \tag{2.23}$$

$$\rho_s = \frac{A_s}{A_c} \tag{2.24}$$

2.3. Time-dependent behaviour of concrete

The total strain over time for an uncracked, uniaxially-loaded specimen consists of four components:

- Instantaneous strain $\varepsilon_e(t)$
- Creep strain $\varepsilon_{cr}(t)$
- Shrinkage strain $\varepsilon_{sh}(t)$
- Temperature strain $\varepsilon_T(t)$

For calculation purposes, the instantaneous, creep, shrinkage and temperature strain are independently calculated and summed up, yielding the total strain of a concrete element. A concrete element, which sets at time τ_d and is loaded with a constant stress σ_{c0} under constant temperature, has the following strain development over time:
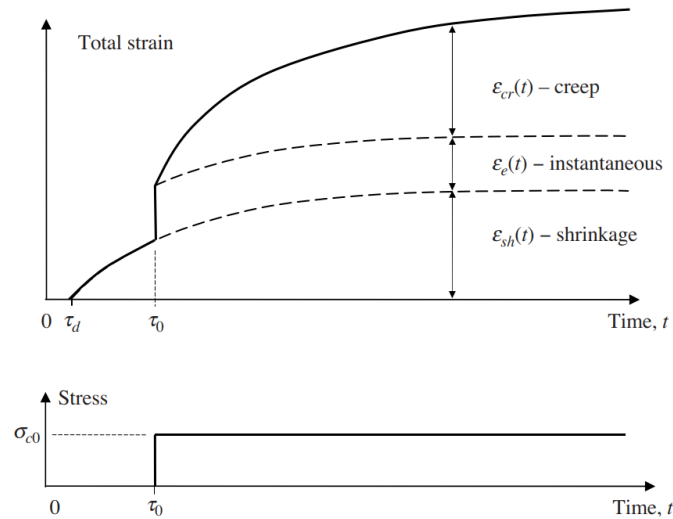
Figure 2.9: Strain development over time of an uncracked and uniaxially loaded concrete element under constant temperature (Gilbert and Ranzi, **2010**).

As seen in figure 2.9, shrinkage occurs in concrete as soon as it starts to set. The rate of this strain progresses with an decreasing rate until an asymptote is reached at a time $t \gg \tau_d$. This shrinkage strain will be further elaborated on later in this paragraph. Then, a load is applied resulting in a stress σ_{c0} at time τ_0 resulting in an instantaneous elastic strain ε_e. Simultaneously, the strain increases with a decreasing rate because of creep. Creep is an interrelated phenomenon with relaxation and is defined as a gradual increase of strain under a constant stress. Similarly, relaxation is the gradual decrease of stress when the strain is held constant.

In reality, no problem can solely be attributed as a creep or relaxation problem as this is determined by the boundary conditions. Completely restrained boundary conditions would result in a pure creep problem and vice versa. In real concrete structures, free deformation is not possible because of internal restraint due to reinforcement and external restraint because of supports as examples. Completely restrained structures are rare to non-existent as this would lead to excessive imposed deformations. This is the reason why concrete structures involve both elements of creep and relaxation (Gilbert and Ranzi, **2010**).

2.3.1. Shrinkage of concrete
Shrinkage of concrete is defined as the unloaded and unrestrained time-dependent strain under constant temperature. It can be subdivided into four main types of shrinkage:

- Plastic shrinkage

- Autogenous shrinkage

- Thermal shrinkage

- Drying shrinkage

Plastic shrinkage occurs in fresh concrete and is the result of bleed water evaporating to the environment. As mentioned earlier, high-strength concretes are more prone to plastic shrinkage causing capillary tension in the pore water. These tensile stresses may cause concrete to crack during the setting process. The stiffness of concrete has not developed enough for reinforcement to bond, meaning that reinforcement is ineffective in controlling these cracks. Cracking due to plastic shrinkage can be prevented by proper curing methods such as membrane or water curing.

Autogenous or chemical shrinkage starts after concrete has set and is caused by the loss of water from capillary pores as a result of the hydration process of cementitious materials. This form of shrinkage exhibits minimal dependence on both environmental factors and the dimensions of the element or structure. Autogenous shrinkage increases with a lower water to binder ratio and at a higher cement content in a concrete mixture, this effect is visible in figure 2.10.
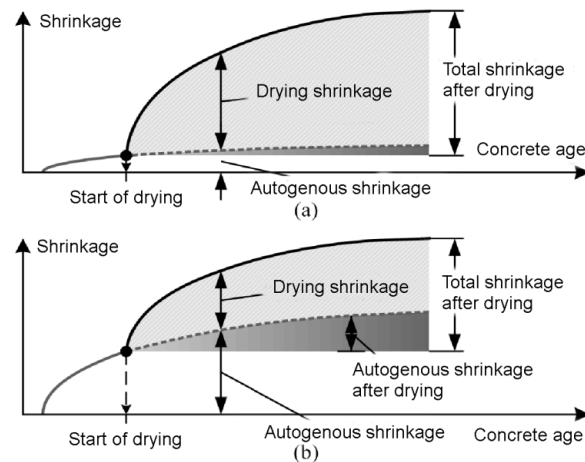
Figure 2.10: Amount of autogenous and drying shrinkage for: (a) normal strength concrete and (b) high strength concrete (Gribniak et al., 2008).

Drying shrinkage is the last main type of concrete shrinkage. Drying shrinkage is defined as the diffusion of water from the capillary pores of hardened concrete to the environment. The humidity within the concrete cell structure is often higher than its surroundings, causing pore water to diffuse in order to establish equilibrium. Drying shrinkage increases in time with a decreasing rate during the months and years after hardening. The factors influencing this type of shrinkage include relative humidity, mixture characteristics, and the size and shape of the concrete element or structure. For thin members such as slabs, drying shrinkage may be completed after several years, while a mass concrete structure may experience drying shrinkage throughout its whole lifetime. Uncracked concrete members typically exhibit negligible drying shrinkage beyond a depth of 300 mm from surfaces exposed to low-humidity environments (Gribniak et al., 2008; Gilbert and Ranzi, 2010).

2.3.2. Thermal shrinkage

Concrete increases in temperature until roughly the first day or couple of days, depending on the concrete mix design, dimensions of the concrete structure, boundary conditions and other external factors such as the initial fresh concrete temperature. This increase in temperature is attributed to the energy released inside of concrete due to the exothermic hydration reaction of binder and water. Concrete starts to cool down again when more energy dissipates to its surrounding compared to the amount of energy generated through exothermic reactions. This happens when the majority of binder has reacted with water, meaning that the degree of hydration is approaching one. During this phase of heating, concrete will expand if the member is unrestrained. When the member is restrained, compressive stresses will arise as explained in figure 2.6.

After reaching the peak temperature, the concrete begins to cool down, causing a temperature differential that leads to shrinkage. This shrinkage results in tensile stresses, particularly for concrete members that are restrained. After reaching its peak temperature, concrete attains significant stiffness, which may lead to tensile stresses surpassing the material's tensile strength. Examples of methods to mitigate thermal shrinkage include cooling the fresh concrete with continuous chilled water, adding supplementary cementitious materials (SCMs) to the concrete mix design, and installing pipes for temperature control. Cooling aggregates prior to casting is another technique, but it primarily helps in reducing the overall temperature rise during hydration. Adding SCMs such as fly ash or blast furnace slag can significantly decrease the hydration heat of concrete. Concrete mixtures including SCMs will still maintain more or less the same or even higher compressive strengths than ordinary Portland cement (OPC) without SCMs (Sarker and McKenzie, 2009; Moon et al., 2018).

The fineness of cement also has influence on the initial heat release. Coarser cement, opposed to cement grounded to a fine powder, has a lower initial heat release. The reason for this, is that the specific surface area decreases with coarser particles, leading to a reduced volume available for reaction and, consequently, less heat being released. The cumulative heat release and degree of hydration of coarse and fine cement are nearly equivalent for low w/c cement pastes (0.30). However, the final

degree of hydration for coarse cement with w/c = 0.50 is significantly lower. Using coarser cement is useful to avoid cracking due to thermal shrinkage (Bentz et al., 1999), however one should consider the potential of a reduced degree of hydration.

Coefficient of thermal expansion

An important parameter for thermal shrinkage is the coefficient of thermal expansion (CTE), α_e. The strain due to a temperature difference is dependent on the CTE and the amount of temperature difference the element experiences, formulated in the equation below:

$$\varepsilon_{th} = \alpha_e \Delta T \tag{2.25}$$

In accordance with EN1992-1-1, a CTE of $1 \cdot 10^{-5}\,°C^{-1}$ may be used for concrete when more accurate information is unavailable. The CTE of concrete is initially higher immediately after placement and gradually becomes constant after approximately 8 to 10 hours as depicted in figure 2.11. Therefore, time dependency only needs to be accounted for during these initial hours (Jeong et al., 2012).
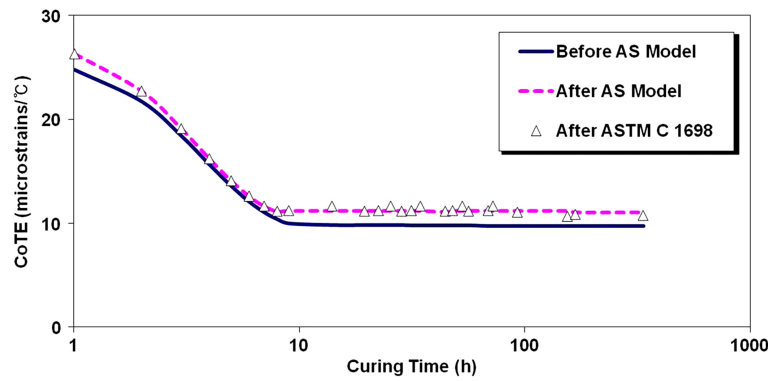
Figure 2.11: Time non-linear behaviour of the CTE with and without consideration of autogenous shrinkage (Jeong et al., 2012).

The CTE of concrete depends on several factors, including air content, relative humidity, aggregate type, and water-to-cement ratio. Increased air voids in concrete result in a lower CTE, which can have a significant effect (Zeng et al., 2012). Relative humidity also impacts the CTE, with the highest CTE observed at 85% relative humidity, while the minimum CTE is found at relative humidities of 100% and below 50% (Jeong et al., 2012).

The CTE of aggregates varies between $0.5 - 1.2 \cdot 10^{-5}\,°C^{-1}$ depending on their mineral composition, which is generally lower than the CTE of cement paste, which deforms $1.5 - 2 \cdot 10^{-5}$ per degree Celsius (Zeng et al., 2012). Additionally, the water-to-cement ratio affects the CTE. Specimens with $w/c = 0.5$ and $w/c = 0.35$ show similar CTE values, while specimens with $w/c = 0.65$ exhibit a significantly lower CTE (Tang et al., 2020).

2.4. TSTM

Discussions arose when the Zillergründl Dam in Austria was to be constructed from 1983 until 1985. This dam, with a height of 186 metres, is 6 metres thick at its crest and 36 metres at the base. This concrete structure can be labelled as a massive concrete structure due to these dimensions. Internal temperature gradients are almost unavoidable and will cause both compressive and tensile stresses. Besides internal restraints, the dam is also externally restrained as it is constructed on a bedrock foundation. Figure 2.12 (a) shows a thick wall during hydration of which the area close to the outside has cooled down. The internal part of the wall tends to expand, while the outer parts restrain this motion. Because of this, the outer parts will be under tension and the core of the wall under compression. Figure 2.12 (b) shows the effect of a bedrock foundation. When the wall, or dam in this case, will shrink because it is cooling down again, tensile stresses will arise in the base of the dam.

Figure 2.12: (a) Internal restraint due to a temperature gradient in the cross-section (b) Stiff foundation externally restraining the cooling wall cast on top
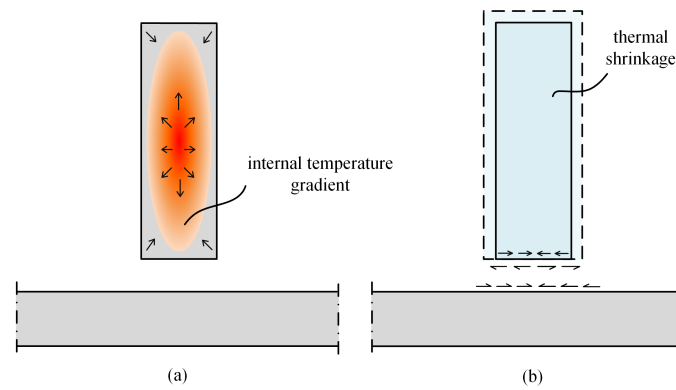
The dam, consisting of $1.37 \cdot 10^6$ m^3 of concrete, was either going to be constructed using blast furnace slag cement with a high slag content, or OPC with an addition of 33% fly ash. In order to measure the susceptibility to cracking of the concrete mix designs, the TSTM was designed by the Institute of Building Materials of the Technical University of Munich. E. Gierlinger and R. Springenschmid constructed the machine such that a deformation of 1 μm would be counteracted by a control machine. This control machine would thus ensure that the dogbone specimen is restrained on both ends to induce early age stresses. In this way, the temperature at which the first crack occurs could be measured. It was regarded that the lower this temperature, the more susceptible the concrete mix design is to early age cracking (Springenschmid et al., 1994).

2.4.1. Principles of the TSTM
Numeral TSTMs have been developed since 1984, including Technion, Hohai University, NTNU, the University of Queensland, the University of Tokyo and TU Delft. The latter was developed by Lokhorst in 2000 and has a cross-section of 150 x 100 mm with a length of 1450 mm. Concrete is cast within a dogbone mold and the test is started when the concrete starts to set. During the test, the temperature inside the concrete can be controlled using a cryostat, which circulates water through pipes running throughout the mold. The strain of the specimen is measured using 4 Linear Variable Differential Transformers (LVDTs) in the straight and narrow part of the dogbone. The TSTM of Technion and Hohai University measure the strain on one end, while it is advisable to measure on both sides to enable the detection of eccentric deformations. The advantage of measuring in the narrow part of the dogbone instead of at the ends of the dove tails, is because there are stress concentrations at these ends. Another way of measuring strain is using the loading grip data. However, this method will include slip between the loading grip and the specimen, which will introduce errors and inaccuracies in the strain measurements. The TSTM can either be placed vertically or horizontally, both having their own advantages and disadvantages. Literature advises to perform the test vertically instead of horizontally. This is because the friction of hardened concrete with the mold can cause errors in the stress measurements (Liang, 2024).
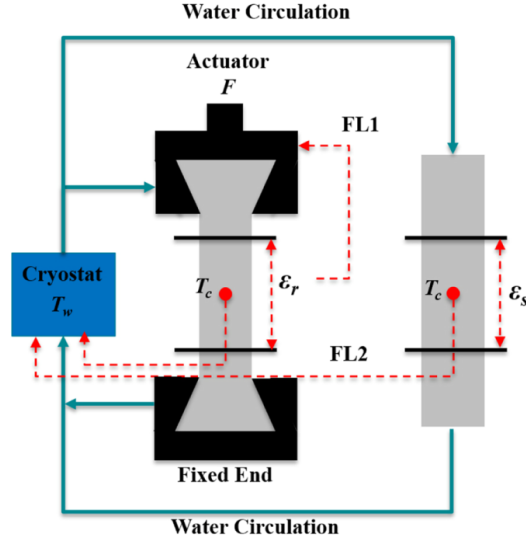
Figure 2.13: Schematization of the working principles of the TSTM system (Liang et al., 2024).

Figure 2.13 shows the schematization of the TSTM with the dogbone shaped specimen in the middle. Two embedded steel bars are visible inside of the specimen which are attached to the LVDTs to measure the strain ε_r. The bottom of the TSTM is fixed, while the top part is moved using an actuator. The actuator of the Instron is controlled by the strain ε_r measured during the test, to counteract any movement with a respective force F. The cryostat is displayed in the blue rectangle on the left of the figure and is controlled via the measured concrete temperature T_c in the middle of the dogbone.

A prismatic concrete specimen is shown on the right of the figure and is also attached to the cryostat. This is the Autogenous Deformation Testing Machine (ADTM) and has two free ends, allowing the concrete to freely expand and shrink during the test. The strain of the ADTM is denoted by ε_s in figure 2.13. Both the TSTM and ADTM are covered with a plastic film to ensure no plastic and drying shrinkage will occur. The strain in the TSTM and ADTM are the sum of the following components:

$$\varepsilon_{TSTM} = \varepsilon_e + \varepsilon_c + \varepsilon_{th} + \varepsilon_s$$

$$= 0$$

$$\varepsilon_{ADTM} = \varepsilon_{th} + \varepsilon_s \tag{2.27}$$

(2.26)

In which ε_e is the elastic strain imposed by the force applied by the Instron, ε_c is the strain because of creep, ε_{th} is the thermal strain and ε_s is the strain due to autogenous deformation. The total amount of strain during the TSTM test is equal to zero as the strain is continuously counteracted by the actuator. In equation 2.27 there is no elastic or creep strain because there is no externally applied load present and the specimen is not restrained so creep does not occur. Subtracting equation 2.26 from equation 2.27 results in the creep:

$$\varepsilon_c = \varepsilon_{TSTM} - \varepsilon_{ADTM} - \varepsilon_e$$

$$= -(\varepsilon_{ADTM} + \varepsilon_e)$$

(2.28)

The creep behaviour of a concrete mix design can be determined using this TSTM setup as shown in equation 2.28. The relaxation can be determined as well, since creep and relaxation are interrelated (Liang, 2024):

$$J(t_0, t_f)R(t_0, t) + \int_{t_0}^{t_f} J(t', t_f)R(t_0, t') \, dt' = 1 \tag{2.29}$$

The creep compliance is denoted as $J(t_0, t)$ and $R(t_0, t_0)$ is the relaxation modulus in equation 2.29.

The TSTM is used to study novel types of concrete and to study the effect of temperature on the early age behaviour of concrete. The first of two examples of recent studies using the TSTM is a study on the autogenous deformation and stress evolution of high-volume ground granulated blast furnace slag (GGBFS) concrete (Liang et al., 2023). The second example is the influence of temperature on the autogenous deformation and stress evolution in cement pastes with low water to cement ratios (Liang et al., 2024).

2.4.2. Mini-TSTM

The regular TSTM system at Delft University of Technology requires 3 to 4 operators for several working days to prepare and initiate a test. This preparation involves mixing over 60 liters of concrete and installing various equipment, including temperature and strain sensors and the cryostat. Additionally, the TSTM test is prone to occasional failures due to its dependence on the loading machine's control system and sensitive LVDTs. These factors, combined with the substantial human resources required, lead to an extended duration for a single research project. Liang recognized both the necessity and the opportunity to enhance the efficiency of the TSTM system by minimizing the need for human resources. Therefore, he developed a scaled-down version of the TSTM, known as the mini-TSTM, with dimensions of 50 x 50 mm and a length of 100 mm. This mini-TSTM was designed to reduce the need for extensive human resources while maintaining precision. Liang validated the accuracy of the mini-TSTM by building a one dimensional uniaxial restraint test predicting the early age stress with the tested autogenous deformation, elastic modulus and creep as the input. Six different tests were performed, demonstrating a good level of accuracy and therefore proving the mini-TSTM as an effective tool for investigating early-age cracking in cementitious materials. (Liang, 2024).

(a) Mini-ADTM during testing   (b) Mini-TSTM during testing   (c) Dimensions of the mini-TSTM dogbone specimen (in mm)
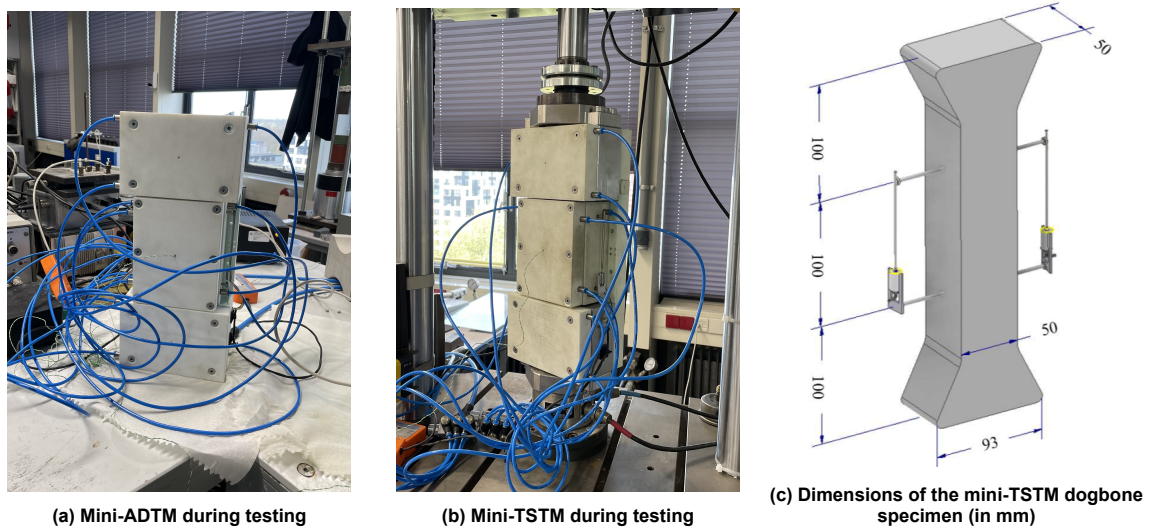
Figure 2.14: Visual representation of the mini-TSTM system (Liang, 2024).

Figure 2.14 shows the TSTM system including the ADTM and TSTM tests including the dimensions of the dogbone specimen. The working concept of the mini-TSTM is the same as the regular TSTM as shown in figure 2.13. The main differences between the TSTM and the mini-TSTM are the following:

(1) Reduced dimensions compared to the TSTM. The volume of the mini-TSTM and mini-ADTM is 0.7 liters compared to 60 liters for the TSTM and ADTM. The cross-section equals 50 x 50 mm and 150 x 100 mm respectively.

(2) The specimens are placed vertically instead of the usual horizontal arrangement. The influence of friction is minimized because of this.

(3) The strain is measured by two LVDTs instead of four. This makes the setup more prone to errors and therefore less robust. The LVDTs are not influenced by stress concentrations in the crossheads as they are placed away from these crossheads as depicted in figure 2.14c.

(4) Other TSTM setups, except for the regular TSTM setup of TU Delft, make use of stepping control. This enholds that a force is applied whenever a certain strain threshold is exceeded. The mini-TSTM is proportional-integral-derivative (PID) controlled, meaning that an algorithm constantly adjusts the load for more accurate controlling of the test.

Due to the smaller dimensions of the mini-TSTM, only small aggregates such as sand can be used. In literature, TSTM tests are often performed without reinforcement as the main interest is the early age behaviour of concrete. The inclusion of reinforcement further reduces the possibility of including large aggregates.

Besides requiring significantly less volume of fresh concrete and reduced human resources, the mini-TSTM can be placed inside of an universal Instron loading machine. Figure 2.14a shows the mini-TSTM being fixed to the base of the Instron and the piston on top. Both the top part and the bottom part of the mold are fixed to the Instron using four bolts. The capacity of this Instron machine is 10 kN which is enough for the failure of unreinforced concrete.

3

Crack width calculation - design codes

In order to compare the structural calculations of crack widths to the true crack widths measured during the construction and use phase of a concrete structure, different structural design codes will be analyzed. These codes provide comprehensive guidelines and recommendations for the design and construction of concrete structures. The codes which will be discussed are NEN-EN 1992-1-1 and NEN-EN 1992-3 belonging to Eurocode 2, fib Model Code 2010, CIRIA C766 and *'Concrete Structures under Imposed Thermal and Shrinkage Deformations'* by Klaas van Breugel. Eurocode 2 is widely used across Europe as a reference for designing safe, reliable, and durable concrete structures. Model Code 2010 is created by International Federation for Structural Concrete (FIB) and serves as a basis for future codes and therefore is deemed interesting to analyze as well. CIRIA C766 refers to a guidance document published by the Construction Industry Research and Information Association (CIRIA). This document provides guidance on controlling the risk of thermal cracking in concrete structures during the early stages of hydration and curing. Since this research focuses on thermal cracking, this document is also selected for analysis. The last document chosen for analysis is *'Concrete Structures under Imposed Thermal and Shrinkage Deformations'* by Van Breugel. This publication addresses the behaviour of concrete structures subjected to thermal and shrinkage deformations and is therefore relevant for this research as well.

3.1. NEN-EN 1992-1-1

Chapter seven of *Design of concrete structures - Part 1-1: General rules and rules for buildings* of NEN-EN1992-1-1 is about serviceability limit states (SLS). The third section discusses crack control and commences with crack width limits for different exposure classes. These exposure classes are assigned to different parts of a concrete structure based on their environment. For example, the XC3 label indicates that concrete at this specific part of the structure is exposed to moderately humid conditions. Because of these conditions, the concrete is more prone to corrosion due to carbonation. Naturally, concrete exposed to more wet conditions has more strict crack width limits in comparison with concrete in dry environments. Figure 3.1 shows the limits as stated in NEN-EN 1992-1-1. These crack width limits are either drawn up because of durability or aesthetic reasons, as mentioned before in section 1.1.

Exposure Class	Reinforced members and prestressed members with unbonded tendons	Prestressed members with bonded tendons
	Quasi-permanent load combination	Frequent load combination
X0, XC1	0,4[1]	0,2
XC2, XC3, XC4		0,2[2]
XD1, XD2, XS1, XS2, XS3	0,3	Decompression

Note 1: For X0, XC1 exposure classes, crack width has no influence on durability and this limit is set to guarantee acceptable appearance. In the absence of appearance conditions this limit may be relaxed.
Note 2: For these exposure classes, in addition, decompression should be checked under the quasi-permanent combination of loads.

Figure 3.1: Concrete crack width limits according to NEN-EN 1992-1-1 for different kinds of exposure classes (CEN, 2005).

3.1.1. Control of cracking without direct calculation

NEN-EN 1992-1-1 defines two methods to control cracking, one without direct calculation and a second method with direct calculation of crack widths. The method without direct calculation prescribes a maximum reinforcing bar diameter and a maximum spacing between reinforcing bars. Based on the steel stress and the critical crack width, the value of these latter parameters is given. The steel stress is calculated on the basis of a cracked section with the relevant combinations of actions acting on the reinforced concrete element. In figure 3.2, the table with maximum reinforcing bar diameter is presented as given in the Eurocode.

Steel stress[2] [MPa]	Maximum bar size [mm]		
	$w_k = 0,4$ mm	$w_k = 0,3$ mm	$w_k = 0,2$ mm
160	40	32	25
200	32	25	16
240	20	16	12
280	16	12	8
320	12	10	6
360	10	8	5
400	8	6	4
450	6	5	-

Figure 3.2: Maximum reinforcing bar diameter for different steel stresses and critical crack widths (CEN, 2005).

The standard states that this table may be used to design prestressed concrete structures and reinforced concrete structures where cracks are likely to occur due to restraint and due to loading. For these three cases, the crack width limit will unlikely be exceeded when the maximum bar diameters in the provided table are complied with. Another way of controlling cracks is utilizing the second table provided in this subsection, giving values for the maximum reinforcing bar spacing for the steel stress just after cracking and critical crack width. This table may be applied to prestressed concrete structures and reinforced ones in which cracking is likely to happen because of loading, but not for cracking which happen due to restraint. Figure 3.3 shows the table with maximum reinforcing bar spacing to prevent excessive cracking.

Steel stress[2]	Maximum bar spacing [mm]		
[MPa]	w_k=0,4 mm	w_k=0,3 mm	w_k=0,2 mm
160	300	300	200
200	300	250	150
240	250	200	100
280	200	150	50
320	150	100	-
360	100	50	-

Figure 3.3: Maximum reinforcing bar spacing for different steel stresses and critical crack widths (CEN, 2005).

It should be noted that the maximum bar diameter ϕ_s^* in figure 3.2 still needs to be adjusted depending on whether the element is in pure tension or bending. The following modification should be made when the member is subjected to a bending moment:

$$\phi_s = \phi_s^*(f_{ct,eff}/2.9)\frac{k_c h_{cr}}{2(h-d)} \tag{3.1}$$

For a reinforced concrete element under uniform axial tension, the modification is as follows:

$$\phi_s = \phi_s^*(f_{ct,eff}/2.9)\frac{h_{cr}}{8(h-d)} \tag{3.2}$$

where:

ϕ_s = is the adjusted maximum bar diameter
ϕ_s^* = the maximum bar diameter as given in figure 3.2
k_c = a coefficient which takes account of the stress distribution within the section immediately prior to cracking and he change of lever arm
$f_{ct,eff}$ = the mean value of the tensile strength of concrete at the time of cracking
h = the overall depth of the section
h_{cr} = the depth of the tensile zone immediately prior to cracking
d = the effective depth to the centroid of the outer layer of reinforcement

3.1.2. Direct calculation of crack widths

The somewhat more sophisticated way of controlling cracks is to directly calculate the crack width w_k. NEN-EN 1992-1-1 does this by taking the strain difference between the reinforcing steel and concrete and multiplying this with the maximum crack spacing:

$$w_k = s_{r,max}(\varepsilon_{sm} - \varepsilon_{cm}) \tag{3.3}$$

where:

$s_{r,max}$ = the maximum crack spacing
ε_{sm} = the mean strain in the reinforcement including the effect of imposed deformations and taking into account the effects of tension stiffening.
ε_{cm} = the mean strain in concrete between cracks

The strain difference between the reinforcing steel and concrete is calculated in the following manner in NEN-EN 1992-1-1:

$$\varepsilon_{sm} - \varepsilon_{cm} = \frac{\sigma_s - k_t\frac{f_{ct,eff}}{\rho_{p,eff}}(1 + \alpha_e\rho_{p,eff})}{E_s} \geq 0.6\frac{\sigma_s}{E_s} \tag{3.4}$$

where:

σ_s = the steel stress assuming a cracked section
k_t = a factor dependent on the load duration
E_s = the Young's modulus of steel
α_e = the ratio E_s/E_{cm}

and

$$\rho_{p,eff} = \frac{A_s + \chi_1^2 A_p'}{A_{c,eff}} \tag{3.5}$$

in which:

A_s = the area of steel
χ_1^2 = the adjusted ratio of bond strength between prestressing and reinforcing steel
A_p' = the area of pre or post-tensioned tendons within $A_{c,eff}$
$A_{c,eff}$ = the effective area of concrete, meaning without the area of prestressing or reinforcing steel

The maximum spacing between cracks is dependent on the concrete cover, the reinforcing bar diameter, the effective ratio of steel and concrete and four coefficients. The formulation of the maximum crack spacing in NEN-EN 1992-1-1 is as follows:

$$s_{r,max} = k_3 c + \frac{k_1 k_2 k_4 \emptyset}{\rho_{p,eff}} \tag{3.6}$$

where:

k_3 = a country dependent coefficient (3.4 in the Netherlands (NEN, 2020))
c = the concrete cover
k_1 = a coefficient dependent on the bond properties of the reinforcing steel
k_2 = a coefficient which takes account of the distribution of strain
k_4 = a country dependent coefficient (0.425 in the Netherlands (NEN, 2020))
$\emptyset$ = the reinforcing bar diameter

The coefficient k_1 is equal to 0.8 for reinforcing bars with high bond properties and 1.6 for bars with an effectively plain surface. The value of k_2 equals 0.5 for elements under bending and 1.0 for elements under pure tension. There are two situations in which a different expression has to be used than equation 3.6, which is when the spacing exceeds $5(c + \frac{\emptyset}{2})$ and when there is no reinforcement in the tension zone. The following expression should be used in these cases:

$$s_{r,max} = 1.3(h - x) \tag{3.7}$$

The distance from most outer fiber in compression to the neutral axis is denoted by x. There is one more exception in which the direction of the principle stress and reinforcement deviates more than 15°. The expression for this situation is irrelevant for this research.

3.2. NEN-EN 1992-3

NEN-EN 1992-3 provides guidelines and standards for the design of concrete structures that are intended to retain liquids and other substances without leakage or failure. This part of Eurocode 2 includes two annexes containing information on the calculation of strains, stresses and crack widths in concrete sections under restrained imposed deformation, namely 'Annex L' and 'Annex M'. The amount of strain and therefore the amount of stress is dependent on the the degree of restraint of an element. NEN-EN 1992-3 distinguishes two different cases of elements with different degrees of restraint: namely a member restrained on both ends and an element of which one of its edges is restrained.
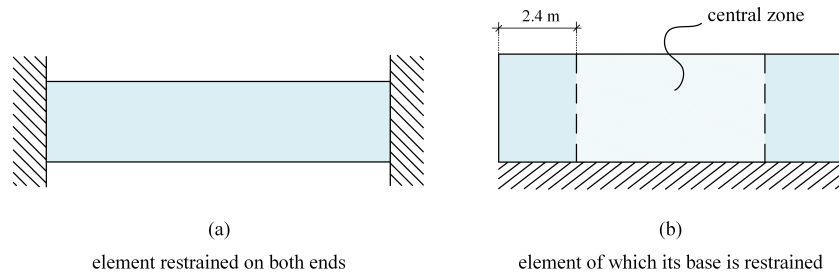
Figure 3.4: Two different types of restrained elements described in NEN-EN 1992-3.

In case (a) where the member is restrained on both ends and an arbitrary imposed deformation only causes an axial force, the degree of restraint R is equal to 1.0. The element is not able to deform by any means. Case (b) is different in the sense that an arbitrary imposed deformation causes both axial stress and bending moments. The amount of restraint of axial force and bending moment differs throughtout the element. Annex L states the expression to calculate the amount of strain for this element, knowing the amount of restraint:

$$\varepsilon_{az} = (1 - R_{ax})\varepsilon_{i_{av}} + (1 - R_m)\frac{1}{r}(z - \underline{z}) \tag{3.8}$$

where:

$\begin{array}{lll}
R_{ax} & = & \text{the degree of (axial) external restraint} \\
R_m & = & \text{the degree of moment external restraint (often 1.0)} \\
\varepsilon_{i_{av}} & = & \text{the average strain of equivalent unrestrained element} \\
\varepsilon_{az} & = & \text{the actual strain at level z} \\
z & = & \text{the height of the section} \\
\underline{z} & = & \text{the height to the section centroid} \\
r & = & \text{the radius of curvature}
\end{array}$

The degree of restraint on the sides of the element (outside of the central zone) is prescribed. The degree of restraint for the central zone is dependent on the ratio between the length and height of the element, L/H. These restraint values can be found in figure 3.5.

Ratio L/H (see Fig L.1)	Restraint factor at base	Restraint factor at top
1	0,5	0
2	0,5	0
3	0,5	0,05
4	0,5	0,3
>8	0,5	0,5

Figure 3.5: Restraint factors for the central zone of an element restrained at its base (NEN, 2011b).

3.2.1. Element restrained on ends - crack width calculation

The approach to calculate crack widths for an element restrained on both ends and subjected to imposed deformation is modified compared to the approach in NEN-EN1992-1-1. The expression found in equation 3.4 is adjusted in the following manner:

$$(\varepsilon_{sm} - \varepsilon_{cm}) = \frac{0.5\alpha_e k_c k f_{ct,eff}}{E_s}\left(1 + \frac{1}{\alpha_e \rho}\right) \tag{3.9}$$

The subsequent steps are the same as in NEN-EN 1992-1-1, meaning that equation 3.6 is used to determine the maximum crack spacing and thereafter the maximum crack spacing is obtained using equation 3.3.

3.2.2. Element restrained at its base - crack width calculation

An element restrained at its base behaves differently than the element restrained at its ends. In this case, the formation of a crack only affects stress distribution locally, unlike the situation with end restraint. Here, the crack width depends on the restrained strain rather than the concrete's tensile strain capacity. Again, the average strain of concrete and steel is adjusted compared to the NEN-EN 1992-1-1 approach:

$$(\varepsilon_{sm} - \varepsilon_{cm}) = R_{ax}\varepsilon_{free} \tag{3.10}$$

where:

R_{ax} =   the degree of (axial) external restraint (see equation 3.9)
ε_{free} =   the strain of an equivalent unrestrained member (see equation 3.4)

The rest of the procedure is again the same, the maximum crack spacing should be multiplied with equation 3.10 to obtain the maximum crack width.

3.3. fib Model Code 2010

The fib Model Code for Concrete Structures serves as a foundational framework for future structural design codes, incorporating advancements in concrete technology and structural engineering. It aims to optimize structural behavior based on new insights and innovations while providing guidance for updating existing codes or developing new ones. The 2010 edition of the Model Code presents an extensive overview of material properties, including concrete up to strength class C120, reinforcing and prestressing steel, and emerging materials like fibre concrete and non-metallic reinforcement. Emphasizing a 'life cycle' approach, it addresses reliability, functionality, durability, and sustainability considerations, with provisions for various loading conditions, environmental factors, and innovative reinforcement types. The document, subject to refinement based on feedback, underscores the importance of robustness, serviceability, and ultimate limit state design for ensuring the safety and performance of concrete structures in diverse conditions (fib, 2013).

Model Code 2010 bases its crack width calculations on a centrically reinforced member subjected to tension, outlining four stages similar to those depicted in figure 2.1. However, it differs from the diagram by identifying two distinct stages: the stabilized cracking stage and the steel yielding stage. Model Code acknowledges the fact that the crack formation stage is not a horizontal line at N_{cr}, as in reality the first crack propagates at the location where the concrete is weakest, assumed to have a strength of $f_{ctk,0.05}$. The last crack is estimated to occur at a location with a strength of $f_{ctk,0.95}$. This results in the behaviour observed in experimental work of which an example is given in figure 2.2. The simplified tensile member diagram is deemed accurate enough according to Model Code because of numeral uncertainties such as the accuracy of positioning reinforcement, the real effective tensile strength of concrete and the influence of construction quality.

3.3.1. Crack width calculation

The design crack width w_d in the last three phases of the tensile member diagram (crack propagation, stabilized cracking and steel yielding) may be calculated using the following expression:

$$w_d = 2l_{s,max}(\varepsilon_{sm} - \varepsilon_{cm} - \varepsilon_{cs}) \tag{3.11}$$

where:

$l_{s,max}$ =   the length over which slip between concrete and steel occurs
ε_{sm} =   the average steel strain over $l_{s,max}$
ε_{cm} =   the average concrete strain over $l_{s,max}$
ε_{cs} =   the strain of concrete due to shrinkage

This equation is identical to the expression of Eurocode (equation 3.3), only the shrinkage of concrete is taken into account explicitly. The length over which slip occurs between concrete and steel may be calculated in the following manner:

$$l_{s,max} = k * c + \frac{1}{4} * \frac{f_{ctm}}{\tau_{bms}} * \frac{\varphi_s}{\rho_{s,ef}} \qquad (3.12)$$

where:

k	=	an empirical coefficient taking the influence of concrete cover into account (may be assumed to be 1.0)
c	=	the concrete cover
τ_{bms}	=	the mean bond strength between steel and concrete
φ_s	=	the reinforcing steel diameter
$\rho_{s,ef}$	=	the effective reinforcement ratio

The relative mean strain, meaning the strain difference between concrete and steel over the length $l_{s,max}$, can be determined as follows:

$$\varepsilon_{sm} - \varepsilon_{cm} - \varepsilon_{cs} = \frac{\sigma_s - \beta * \sigma_{sr}}{E_s} - \eta_r * \varepsilon_{sh} \qquad (3.13)$$

where:

σ_s	=	the steel stress in a crack
σ_{sr}	=	the steel stress right after a crack occurs (see equation 2.6)
β	=	an empirical coefficient dependent on the type of loading
η_r	=	a coefficient considering the contribution of shrinkage
ε_{sh}	=	the shrinkage strain

The empirical coefficients used in equation 3.12 and equation 3.13, depend on two factors: firstly, whether the loading is short-term and instantaneous, or if it is long-term and repeated; and secondly, whether the loading causes the element to be in the crack formation stage or in the stabilized cracking stage. The following table is given in Model Code 2010 for the parameters influencing the strain difference between concrete and steel:

	Crack formation stage	*Stabilized cracking stage*
Short term, instantaneous loading	$\tau_{bms} = 1.8 \cdot f_{ctm}(t)$ $\beta = 0.6$ $\eta_r = 0$	$\tau_{bms} = 1.8 \cdot f_{ctm}(t)$ $\beta = 0.6$ $\eta_r = 0$
Long term, repeated loading	$\tau_{bms} = 1.35 \cdot f_{ctm}(t)$ $\beta = 0.6$ $\eta_r = 0$	$\tau_{bms} = 1.8 \cdot f_{ctm}(t)$ $\beta = 0.4$ $\eta_r = 1$

Figure 3.6: Values for τ_{bms}, β and η_r for calculating the strain difference between concrete and steel (fib, 2013).

3.3.2. Effect of load and imposed deformation on cracking

Model Code 2010 has a short paragraph on the combined effect of load and imposed deformation on cracking. It states that when cracking is caused by the combination of both loading types, the stresses at the cracks should be calculated taking both contributions into account. The quasi-permanent loads acting on the element should be considered for reinforced concrete.

3.4. CIRIA C766

CIRIA, the Construction Industry Research and Information Association, is a neutral and independent not-for-profit organization dedicated to driving collaboration and improvement across the built environment and construction sectors. CIRIA has published three publications about cracking caused by restrained deformation in concrete over the past few decades: CIRIA R91, CIRIA C660 and CIRIA C766,

which is the most recent one. These three publications stem from 1992, 2007 and 2019 respectively. CIRIA C766 addresses concerns about the robustness and lack of design guidance which are present in CIRA C660. The main goal of these publications is to improve on the Eurocode when it comes to restrained deformation. To quote CIRIA on the purpose of the second publication: "*The application of CIRIA C660 has identified a number of concerns with the apparently more onerous requirements of BS EN 1992-3 in some circumstances and less robust design in others.*" (Bamforth, 2019).

3.4.1. External restraint

CIRIA C766 offers essential guidance in estimating the risk of cracking due to external restraints, addressing a gap left by BS EN 1992-3, which lacks such guidance. By making a number of simplifying assumptions, the expression as found in equation 3.14 for determining the restrained strain. It has been estimated by this publication that a safety margin of 10 to 15 per cent is realised (Bamforth, 2019).

$$\varepsilon_r = K_{c1} \left[\alpha_c T_1 + \varepsilon_{ca}(3) \right] R_1 + K_{c1} \left[(\varepsilon_{ca}(28) - \varepsilon_{ca}(3)) + \alpha_c T_2 \right] R_2 + K_{c2} \varepsilon_{cd} R_3 \tag{3.14}$$

where:

T_1	=	the difference between the peak temperature and the mean ambient temperature at the end of the thermal cycle
T_2	=	the difference between the mean ambient temperature at the end of the thermal cycle and the minimum element temperature during its lifetime
α_c	=	the coefficient of thermal expansion of concrete
$\varepsilon_{ca}(t)$	=	autogenous shrinkage after t days
ε_{cd}	=	drying shrinkage
R_1	=	the restraint factor applying to the early thermal cycle
R_2	=	the restraint factor applying to the medium-term deformation
R_3	=	the restraint factor applying to the long-term deformation
K_{c1}	=	a coefficient for the effect of stress relaxation due to creep at early age ($= 0.65$)
K_{c2}	=	a coefficient for the effect of stress relaxation in the long term ($= 0.50$)

Three phases are distinguished resulting in individual components of the restrained strain, namely: the early thermal cycle, the medium- and long-term deformation. The early thermal cycle and the medium-term deformation include the thermal expansion and shrinkage and the autogenous deformation during these periods. The restraint factor R_1 for the early age of the element can be estimated using a table provided in CIRIA C766 as shown in figure 3.7.

A	Base of a wall cast on to a massive base	0.6–0.8
B	Top of a wall cast on to a massive base	0–0.5
C	Edge restraint in box type deck cast in stages	0.5
D	Edge element cast onto a slab	0.8
E	Massive pour cast onto blinding	0.1–0.2
F	Base of massive pour cast onto existing mass concrete	0.3–0.4
G	Suspended slabs	0.2–0.4
H	Infill bays, eg rigid restraint	0.8–1.0

Figure 3.7: Early age external restraint values R_1 for different conditions as stated in CIRIA C766 (Bamforth, 2019).

Values for the restraint factors during the medium- and long-term life of the element are also given in CIRIA C766 and can also be calculated based on the cross-sectional area and stiffness of new elements and adjoining elements. The values for autogenous and drying shrinkage are taken from BS EN 1992-1-1. Autogenous shrinkage is a strength and time-dependent variable. Drying shrinkage is also taken from BS EN 1992-1-1 and depends on the concrete strength class, relative humidity, the notional thickness of the cross-section and time.

3.4.2. Internal restraint

Besides external restraints, internal restraints can cause strains beyond the tensile strain capacity of concrete. Especially for massive concrete structures, internal constraints can have a significant impact on the cracking of concrete as displayed in figure 3.5a. CIRIA C766 addresses this by determining the temperature differential between the centre and surface of the element. Autogenous strain is neglected for internal restraint as it is uniform throughout the element and will not cause an additional strain differential. The internal restrained is determined as follows:

$$\varepsilon_r = K_{c1}\Delta T\alpha_c R_1 \tag{3.15}$$

where:

ε_r =   the amount of restrained strain
K_{c1} =   a coefficient for the effect of stress relaxation due to creep at early age ($= 0.65$)
ΔT =   the temperature differential between the centre and surface of an element
α_c =   the coefficient of thermal expansion of concrete
R_1 =   the restraint factor applying to the early thermal cycle

The restraint factor R_1 may be assumed to be 0.42 in the case of internal restraint. It should be noted that any long-term effects are disregarded since the greatest temperature differential typically occurs during the early thermal cycle, which is transient in nature.

3.4.3. Crack width calculation

The internally and externally restrained strain, as given in equation 3.14 and equation 3.15, are not directly used to determine crack widths in CIRIA C766. Rather, it takes into account that the restrained strain is partially relieved when a crack occurs. The following assumption is made for the crack-inducing strain:

$$\varepsilon_{cr} = \varepsilon_r - 0.5\varepsilon_{ctu} \tag{3.16}$$

where:

ε_{cr} =   crack-inducing strain
ε_r =   restrained strain
ε_{ctu} =   tensile strain capacity of concrete

Chapter 3.7 of CIRIA C766 defines the tensile strain capacity of concrete under sustained loading for both early-age and long-term conditions:

ε_{ctu} =   70 μm for early-age conditions
ε_{ctu} =   100 μm for long term conditions

Complementary expression - edge restraint

CIRIA C766 make the distinction between the true restraint and creep which is associated with this level of restraint. The following expression is given:

$$R_{ax} = R_n K_{cn} \tag{3.17}$$

where:

R_{ax} =   the restraint of the element
R_n =   the true restraint
K_{cn} =   the creep

Naturally, the age of concrete affects the restraint and creep of the element. The subscript 'n' indicates the age of concrete, being 1 for early age concrete and 2 or 3 for concrete over the long term. The crack-inducing strain for an element restrained on one edge, is obtained by combining equation 3.14 and equation 3.16.

$$\varepsilon_{\mathrm{r}} = [K_{\mathrm{c1}} [\alpha_{\mathrm{c}} T_1 + \varepsilon_{\mathrm{ca}}(3)] R_1 + K_{\mathrm{c1}} [(\varepsilon_{\mathrm{ca}}(28) - \varepsilon_{\mathrm{ca}}(3)) + \alpha_{\mathrm{c}} T_2] R_2 + K_{\mathrm{c2}} \varepsilon_{\mathrm{cd}} R_3] - 0.5 \varepsilon_{ctu} \qquad (3.18)$$

The ultimate tensile strain of concrete is a time-dependent variable. Therefore, it is important to determine the crack-inducing strain for both early age and long-term conditions, utilizing the corresponding ultimate tensile strain. CIRIA C766 advises to use the three-day tensile strain of concrete for the early age and 28-day value in the long term.

The crack width is obtained by multiplying the crack-inducing strain ε_{cr} with the maximum crack spacing $s_{r,max}$, in the same manner as NEN-EN 1992-1-1. CIRIA C766 also proposes a change to the calculation of the maximum crack spacing compared to the latter named code. A clause in NEN-EN 1992-1-1 states to reduce the coefficient k_1, accounting for bond strength, by a factor of 0.7 when good bond cannot be guaranteed. The instances where poor bond should be assumed are outlined in figure 8.2 of NEN-EN 1992-1-1. However, CIRIA C766 suggests assuming poor bond during the early age of concrete for elements thicker than 300 mm with a concrete cover $c \leq 50\ mm$. In this case the coefficient k_1 becomes $0.8/0.7 = 1.14$.

Complementary expression - end restraint

For the situation in which an element is restrained at both ends, the expression for the the crack-induced strain is given in equation 3.9. This expression of NEN-EN 1992-3 uses the mean tensile strength of concrete at the time of interest $f_{ctm}(t)$ for the calculation of this crack-induced strain. However, CIRIA C766 explains that early age thermal loads have a duration of multiple days and that the cracks will likely develop at the location where concrete is weakest. Therefore, it is proposed to use only 70% of the mean tensile strength for calculation purposes. For normal weight concrete up to C90/105, this value is equal to $f_{ctk,0.05} = 0.7 f_{ctm}$ (NEN, 2020). The crack-induced strain is therefore slightly different compared to NEN-EN 1992-3:

$$\varepsilon_{cr} = (\varepsilon_{sm} - \varepsilon_{cm}) = \frac{0.5 \alpha_e k_c k f_{ctk,0.05}}{E_s} \left(1 + \frac{1}{\alpha_e \rho} \right) \qquad (3.19)$$

3.4.4. Effect of tension stiffening and element length

The expressions for the crack-inducing strain in NEN-EN 1992-3 (equation 3.9) and the adjusted one given in equation 3.19 for elements restrained on both ends, do not include the effects of tension stiffening and length. Tension stiffening refers to the additional stiffness imposed on reinforced concrete elements by the concrete, as depicted in section 2.1. Equation 3.19 is based on the assumption that the load remains the same during the crack propagation phase. In reality however, when the stress in an end restrained element exceeds the tensile strength of concrete anywhere throughout the element, the stress is partially relieved due to tension stiffening. Due to this partial relieve of stress, the crack widths will reduce, this reduction becomes smaller after each subsequent crack. When the load after the first crack increases, the crack will increase in size again until the second crack occurs. Both cracks will then reduce in width again, but to a lesser extent than when the first crack occured. Following this logic, the final crack width is inversely proportional to the length of the element. CIRIA C766 gives an equation to include these effects:

$$\varepsilon_{smr} = 0.5(B+1)\varepsilon_{ctu} \left[\frac{L + 0.5S(n-1)(B-1)}{L - S*n + 0.5S*n(B+1)} \right] \qquad (3.20)$$

where:

ε_{smr}	=	the mean residual strain in the steel after cracking
ε_{ctu}	=	the tensile strain capacity of concrete
L	=	the length of the element restrained on both ends
S	=	the length over which the reinforcement is debonded, which is assumed to be $s_{r,max}$
n	=	the number of cracks that have formed

and

$$B = \left(\frac{k*k_c}{\alpha_e \rho} + 1 \right) \qquad (3.21)$$

The expressions for crack width found in NEN-EN 1992-3, the equation using $f_{ctk,0.05}$ and the equation including tension stiffening and length, are used for an arbitrary example with thermal loading on a restrained element. The results are visualized in figure 3.8:
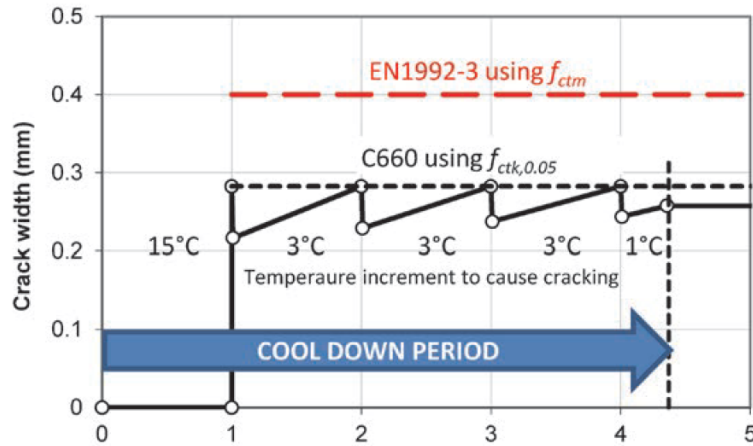

Figure 3.8: Crack width values for a reinforced element subject to imposed thermal loading using EN1992-3, C660 and C766 including tension stiffening (Bamforth, 2019).

The most conservative approach is the one using the mean concrete tensile strength of the element. A constant crack width of 0.4 mm is observed, as there is no stress relief due to tension stiffening. CIRIA C600 (equivalent approach compared to CIRIA C766) uses only 70 % of the mean tensile strength and therefore the crack width is reduced to 0.28 mm. The solid black line represents the approach of CIRIA including tension stiffening and it is clear that he crack width immediately after the first crack is significantly lower compared to the equation without tension stiffening. The crack width after the first crack equals 0.22 mm and just after the fourth crack there is an expected crack width of 0.24 mm. This illustrates the effect of the element length on the crack width.

3.5. Van Breugel

'Concrete Structures under Imposed Thermal and Shrinkage Deformations' by Klaas van Breugel explores the complex behavior of concrete structures subjected to thermal and shrinkage deformations. The book delves into the fundamental principles governing the response of concrete elements to changes in temperature and moisture, offering insights into how these factors influence the overall performance and durability of structures.
Van Breugel distinguishes three phases in the tensile member diagram, as shown earlier in section 2.1. For the second and third stage, the crack formation stage and stabilized cracking stage respectively, there are expressions to determine the crack width.

An interesting remark from the book of Van Breugel is the effect of the load duration on the cracking of concrete. For ordinary concrete made with gravel, the stress at which the concrete cracks at any moment is defined as:

$$\sigma_{cr}(t) = 0.75 f_{ctm}(t) \tag{3.22}$$

The parameter $f_{ctm}(t)$ represents the mean axial tensile strength at the time of cracking. It is assumed in this study that the mean axial tensile strength is equivalent to the mean tensile splitting strength $f_{ctm,sp}$.
For loads with a long-term duration, such as drying shrinkage, the cracking stress is significantly lower than equation 3.22 suggests. For a sustained tensile load the cracking stress equals:

$$\sigma_{cr} = 0.60 f_{ctm} \tag{3.23}$$

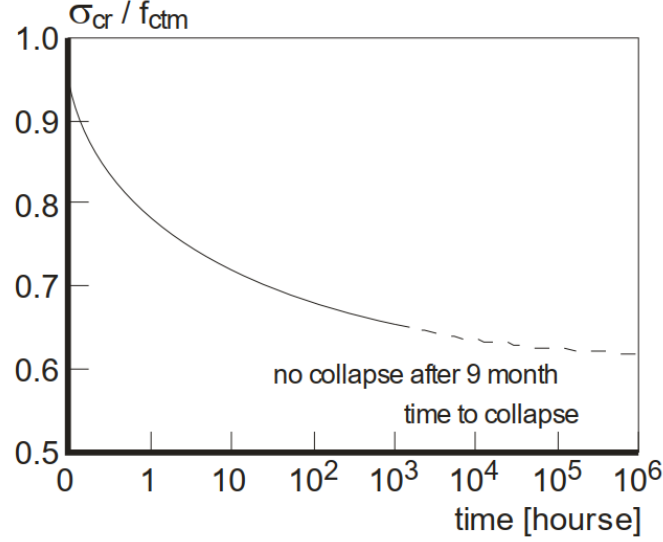The following figure of Van Breugel's book illustrates the effect of time on the cracking load of concrete:

Figure 3.9: Concrete tensile strength as a function of the load duration (van Breugel et al., 2011).

3.5.1. Crack width calculation - crack formation stage

The crack formation stage is characterized by the force acting on the element being equal to the cracking force N_{cr} (in case the simplified tensile bar model is assumed). The second stage lasts until no more cracks can form in the element and this point is characterized by the strain at which the fully developed cracked pattern ε_{fdc} is reached. Van Breugel gives the following mean crack width w_{m0} equation to be used during the crack formation stage:

$$w_{m0} = 2 * \left(\frac{0.4\text{Ø}}{f_{cm,cube}E_s} * \left(\frac{\sigma_{cr}}{\rho} \right)^2 * (1 + \alpha_e \rho) \right)^{0.85} \tag{3.24}$$

One should ensure that the loading on the reinforced element indeed causes the element to enter the crack formation stage, otherwise the latter expression is not valid. In case of an imposed load ε_{imp} it should thus be smaller than the strain at which the fully developed crack pattern ε_{fdc} is reached. The latter value can be determined using the following formula according to Van Breugel:

$$\varepsilon_{fdc} = (60 + 2.4\sigma_{s,cr}) * 10^{-6} \tag{3.25}$$

In this formula, the steel stress immediately after cracking is denoted by $\sigma_{s,cr}$. Equation 3.25 should only be used when the cracks occur in a relatively short period of time. When cracking occurs after a longer period of time, for restrained shrinkage for example, then the following expression should be used:

$$\varepsilon_{fdc\infty} = \gamma_\infty * \varepsilon_{fdc} \tag{3.26}$$

The term γ_∞ is a factor accounting for the long-term effect, being 1.3 at maximum.
Another difference between the book of Van Breugel and the structural codes discussed before, is that Van Breugel also specifies the mean transfer length and crack width instead of only the maximum values. The transfer length in the crack formation stage is a function of the mean crack width w_{m0}:

$$l_{st} = 1.2w_{m0}\frac{E_s}{\sigma_{s,cr}} \tag{3.27}$$

Van Breugel underscores the significance of concrete tensile strength, as it dictates the stress level, σ_{cr}, at which initial cracks form, and notably affects crack width. A higher concrete tensile strength will result in higher stresses in reinforcing steel directly after cracking $\sigma_{s,cr}$ and therefore increases crack widths (van Breugel et al., 2011).

3.5.2. Crack width calculation - stabilized cracking stage

The crack spacing in the third stage of the tensile member diagram, the stabilized cracking stage, varies from l_{st} to $2l_{st}$ as depicted in figure 2.4. The average crack spacing is assumed to be $1.5l_{st}$ so the mean crack spacing over the length of the tensile member equals (see equation 3.27:

$$l_m = 1.8w_{m0}\frac{E_s}{\sigma_{s,cr}} \tag{3.28}$$

The mean crack width during the stabilized cracking stage is a function of the mean crack spacing among other variables:

$$w_{mv} = \frac{l_m}{E_s} * (\sigma_s - 0.5\sigma_{s,cr}) \tag{3.29}$$

The mean crack width during the stabilized cracking stage can also be expressed using the mean crack width for the cracking stage in the following manner:

$$w_{mv} = 1.8w_{m0}\left(\frac{\sigma_s}{\sigma_{s,cr}} - 0.5\right) \tag{3.30}$$

<div style="text-align: right; font-size: 3em;">4</div>

Reinforced mini-TSTM set-up and procedure

To test the hypothesis outlined in section 1.2, an experiment using the mini-TSTM was designed. The objective of the experiment is to measure whether the crack widths, due to the combination of an imposed thermal load due to hydration and a mechanical load, are smaller than the calculations based on theory used in structural design codes would suggest.

Unlike the standard TSTM, the mini-TSTM, with dimensions of 50 mm x 50 mm, has not yet been equipped with reinforcement. Its smaller size limits the possible combinations of bar diameter and the number of bars. According to Eurocode 2, the maximum steel ratio is 4% of the concrete area A_c, meaning that reinforcing bars with a diameter of 12 mm and larger cannot be used as the maximum steel ratio would be exceeded. Concrete containing higher amounts of steel reinforcement will cause the concrete to reach its ultimate strain before the reinforcement starts to yield. As a result, a brittle failure occurs instead of a ductile one, which is undesirable due to safety reasons. There is one more important aspect for the reinforcement layout: the transfer length of the reinforcement should be small enough to allow multiple cracks to form, the reason for which will be explained later.

4.1. Experimental set-up

The mini-TSTM experiment was designed to test novel types of cementitious materials on their early age characteristics such as creep, relaxation and autogenous deformation. The experiment consists of a mold which is placed inside of a uniaxial loading machine, the TSTM and a mold which is unrestrained, the ADTM. The procedure starts preparing the molds (including reinforcement), mixing the mortar and thereafter filling the molds, attaching the cryostat to the mold and then start the experiment when the concrete starts to set.

4.1.1. Reinforcement layout

To analyze crack widths, a reinforcement layout must be designed. Without reinforcement, concrete fails when the load exceeds its tensile strength at any point in the section. There are various geometrical constraints on reinforcement layouts and practical considerations to address. Figure 2.14c depicts a dogbone specimen used in both ADTM and TSTM tests, featuring two embedded bars. Two LVDTs are attached to the ends of these embedded bars to measure the strain between these bars during testing. The steel bars cannot pierce these bars, so the design should account for this. Secondly, the steel bars should be placed symmetrically in order to avoid any eccentricity and therefore undesired bending moments when the specimen is subjected to an axial load. Proper spacing between reinforcing bars and the concrete cover is crucial to ensure effective mortar bonding. Furthermore, the radial bond stress exerted by a reinforcing bar on the concrete should not disrupt adjacent reinforcing bars, as this may invalidate cracking models. Analytical formulations for radial bond stress, found in the literature, depend on whether the concrete is cracked or in the pre-cracking stage (Chang et al., 2021).

Eurocode specifies values for the minimum cover c_{min} with regard to durability depending on the exposure class and structural class of the element (NEN, 2020). Since the TSTM is a scaled down structural element and is not meant as a long-lasting structure in service, this durability requirement is disregarded. The same standard states minimum bond requirements to ensure the safe transmission of bond forces and achieve adequate concrete compaction. For separated bars the minimum cover $c_{min,b}$ equals the diameter of the bar. It is deemed improbable that this requirement will be governing, whereas Model Code 2010 mentions minimum cover requirements in the section about bond stress-slip relationship, which are more strict. For concrete to be considered well-confined, the concrete cover c should be at least five times the bar diameter, and the clear spacing between bars should be at least ten times the bar diameter (fib, 2013).

The reinforcement layout must ensure that multiple cracks can form within the measurement length between the LVDTs, which is 100 mm. If only a single crack forms over this length, it becomes ineffective for the experiment's purpose. The objective is to investigate crack width under the combination of imposed deformation and mechanical loading. To capture the crack formation phase accurately, at least two cracks are required otherwise the stabilized cracking stage starts immediately after the first crack. Ideally, three cracks should form to minimize uncertainty in determining crack widths. Since each measurement is subject to errors, having three cracks rather than one or two will provide more reliable insights into the behaviour of reinforced concrete under a combination of thermal imposed deformation and additional mechanical loading.

The final requirement addresses the stress levels that the steel can achieve during testing. Given that the Instron loading machine has a capacity of 10 kN, reaching ultimate stress levels in the steel is unlikely. Therefore, the reinforcement ratio should be moderate to ensure that crack widths are sufficiently representative and that the steel stresses in the cracks reflect those typically observed in reinforced concrete structures under ultimate or serviceability limit states. An arbitrary maximum steel stress of 300 MPa was selected for the testing. Based on these criteria, the following three reinforcement layouts were designed to meet the outlined requirements:
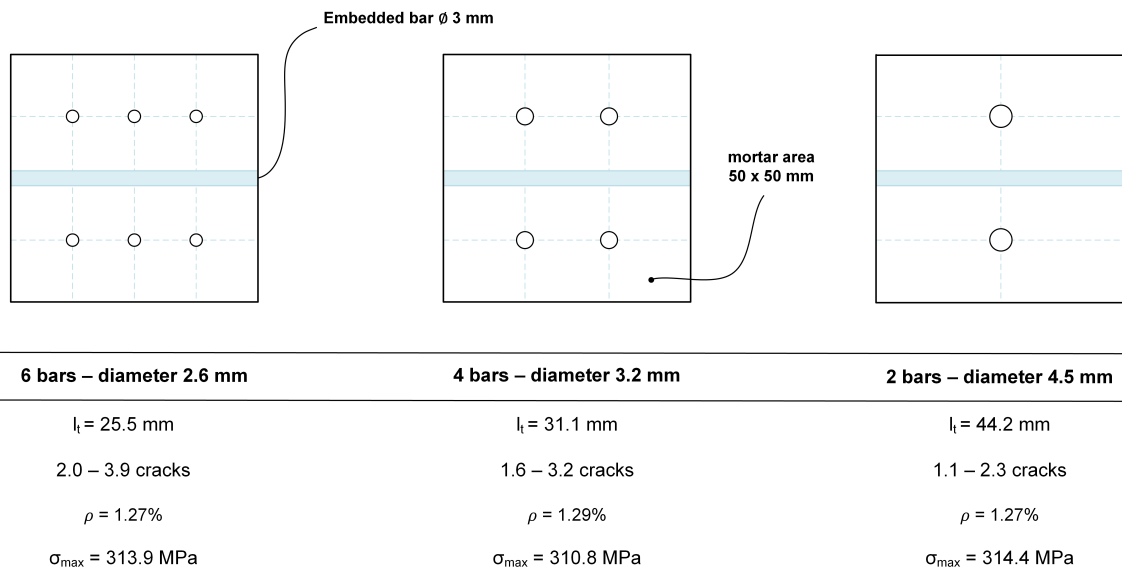

6 bars – diameter 2.6 mm	4 bars – diameter 3.2 mm	2 bars – diameter 4.5 mm
l_t = 25.5 mm	l_t = 31.1 mm	l_t = 44.2 mm
2.0 – 3.9 cracks	1.6 – 3.2 cracks	1.1 – 2.3 cracks
ρ = 1.27%	ρ = 1.29%	ρ = 1.27%
σ_{max} = 313.9 MPa	σ_{max} = 310.8 MPa	σ_{max} = 314.4 MPa

Figure 4.1: Three possible reinforcement layouts complying to the set requirements.

The three reinforcement layouts depicted in figure 4.1 with 6, 4 and 2 steel bars respectively, mainly differ regarding the possible amount of cracks, spacing and concrete cover. A rough estimation for the amount of cracks has been calculated using equation 2.8 and using an assumption of the mean bond strength. Model Code 2010 assumes a mean bond strength of $\tau_{bms} = 1.8 * f_{ctm}(t)$, whereas Van Breugel states that $\tau_b = 2 * f_{ctm,0}$ which shows the best results when comparing theory with experimental results. Combining the latter assumption with equation 2.8, gives the following simplified expression for the transfer length:

$$l_t = \frac{f_{ctm}\emptyset}{4\tau_{bm}\rho}$$
$$= \frac{\emptyset}{8\rho}$$

(4.1)

The amount of cracks is based on the principle depicted in figure 2.4 where the distance between cracks varies between l_t and $2l_t$. Based on this information, the reinforcement layout using six steel bars was chosen. It is expected that three cracks will consistently form during different tests and using more bars would reduce the bar spacing too much. For the configuration using six bars, both the concrete cover and spacing equals 12.5 mm. This does not satisfy the Model Code 2010 requirements to ensure well-confined concrete, however this will be ensured during trial tests.

An important remark is that the bar diameters in figure 4.1 are smaller than the smallest standard steel reinforcing bars, having a diameter of 6 mm. A solution to this problem is using steel threaded bars. These are not commonly used in the construction industry because the distance between each individual rib is relatively small and they have different strength classes than standard reinforcing bars. Strength class B500B is used by practice, whereas threaded bars are classified using the strength classes of bolts and screws. These typically have a lower yield and ultimate strength compared to steel reinforcing bars. Threaded bar M3 is used with a major diameter of 3.0 mm, a minor diameter of 2.459 mm and has a steel grade of 4.8. The mechanical properties are given in table 4.1 below:

Table 4.1: Mechanical properties of steel grade 4.8 (NEN, 2013).

	Steel grade 4.8
Ultimate strength [MPa]	400
Yield strength [MPa]	320
Ultimate strain [%]	22
Young's modulus[1] [GPa]	205

[1] According to EN1992-1-1 (NEN, 2020)

The small rib distance can cause concrete containing coarse aggregates to not provide the expected bond strength with threaded bars. Threaded bar M3 has a pitch of 0.50 mm (the distance between individual ribs), meaning that aggregates larger than this are unable to fit between these ribs to ensure bond strength. Although specific literature on the effect of maximum aggregate size on the bond strength of reinforcement with concrete is lacking, it is anticipated that large aggregates will not bond well with threaded bars. A German company that produces steel anchors for concrete has documented the bond strength of threaded bars under tension loads in C20/25 concrete. Threaded rod M8 up and including M30 were tested, resulting in a bond stress of 6.5 MPa for M30 and 4.0 MPa for M8. Thus, showing that the bond strength decreases for smaller bar diameters in regular concrete containing coarse aggregates (MKT, 2015).

Validation of threaded bar

The information in the previous paragraph is not deemed enough to perform a test and assuming that the bond strength is enough to provide the necessary amount of cracks. Therefore, a trial test is performed using the reinforcement and the concrete (mortar) mix design specified in the next paragraph. A tensile test until the capacity of the Instron, 10 kN, is performed on a specimen which has been cured in a high humidity chamber and expected to have reached its final strength. Using displacement controlled increments, the load was increased to 10 kN and afterward the load was gradually reduced to zero. Digital Image Correlation (DIC) is used to determine the amount of cracks and their widths. The specimen is painted white and afterwards black dots were applied. GOM Correlate 2019 is a software package, able to measure the movement between individual black dots to measure the displacements and strain during the test. Each ten seconds during the test, a photo was taken, and the area between the LVDTs was analyzed using the software. The results of the test are displayed in figure 4.2
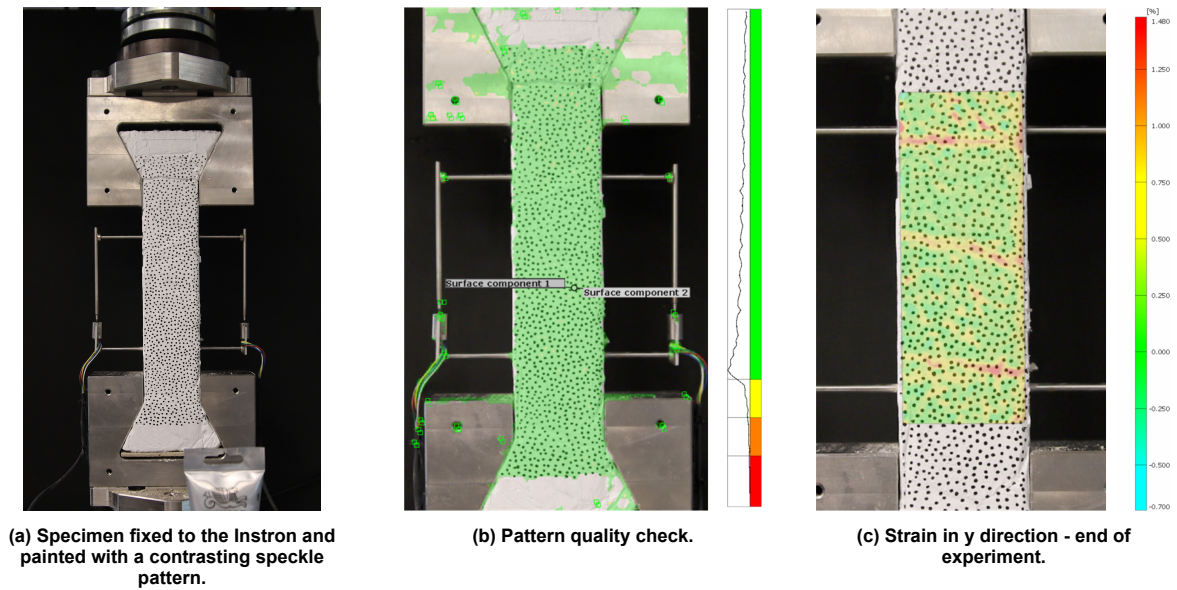
(a) Specimen fixed to the Instron and painted with a contrasting speckle pattern.

(b) Pattern quality check.

(c) Strain in y direction - end of experiment.

Figure 4.2: DIC analysis on a hardened reinforced concrete specimen.

From figure 4.2b, it can be observed that the speckle pattern quality is good as the area of interest is coloured green. The figure on the right, figure 4.2c, displays the strain when the load applied by the Instron on the specimen is equal to 10 kN. Clearly, there are three cracks visible between the LVDTs, which are coloured red. The worst case scenario would be no bond stress between the threaded bar and the concrete, in this case there would be only one crack and the specimen would fail. From the figure, it can be concluded that the threaded bar and the concrete bond well as multiple cracks occurred, in line with the desired amount of three cracks.

4.1.2. Concrete mix design

It was chosen to use mortar instead of concrete for the test, as spaces in the mold including the reinforcement are tight (12.5 mm) and because of the small ribs of the threaded bar reinforcement. The standard mortar mix design is used and the composition as described in EN 196-1 is given in table 4.2.

Table 4.2: Composition of mortar according to EN 196-1 (EN, 2016).

	EN196-1 mortar
Cement [g]	450 ±2
CEN standard sand [g]	1350 ±5
Water [g]	225 ±1

CEN Standard Sand is characterized by a specific grain size distribution, ranging from 0.08 to 2.00 mm, with rounded particles. This sand has a silica content of at least 98%, and a maximum moisture content of 0.2%. It is packaged in bags of 1350 (± 5) grams and for each dogbone one of these bags is used. The particle size distribution is shown in figure 4.3.

Square mesh size (mm)	2,00	1,60	1,00	0,50	0,16	0,08
Cumulative sieve residue (%)	0	7 ± 5	33 ± 5	67 ± 5	87 ± 5	99 ± 1

Figure 4.3: Particle distribution of CEN standard sand (EN, 2016).

In the Netherlands, CEM III/B is a common type of cement used in the construction industry. This cement type includes blast furnace slag to replace a portion of clinker, with the Dutch practice typically

using 65-75% slag. This is labeled as CEM III/B according to NEN 197-1 standards and has been the dominant cement type since the 1970s (NEN, 2011a; Polder et al., 2014). The slag acts as a binder and helps to reduce CO_2 emissions and lower the embedded energy compared to Portland cement, which consists entirely of clinker. The composition of CEM III/B cement is detailed in table 4.3.

Table 4.3: Specified composition of used cement (ENCI, 2020).

	CEM III/B 42.5 N-LH/SR
Clinker[1] [%]	27
Blast furnace slag[1] [%]	71
Secondary components[1] [%]	2
Setting time adjuster[2] [%]	4.8
Grinding aid[2] [%]	0.04
Reducing agent[2] [%]	0

[1] As a percentage of the sum of the primary and secondary components
[2] As a percentage of the cement

Cement hydration is a chemical process that begins as soon as water is added to the cement powder. The hydration reactions involve various clinker minerals, most notably tricalcium silicate (C3S), dicalcium silicate (C2S), tricalcium aluminate (C3A), and tetracalcium aluminoferrite (C4AF). Among these, C3A reacts most rapidly with water, which can lead to flash setting—an almost immediate stiffening of the cement paste that is undesirable for practical construction purposes. To control this rapid reaction and provide a workable time frame, setting time adjusters such as gypsum ($CaSO_4 \cdot 2\,H_2O$) and anhydrite ($CaSO_4$) are added to the cement.
A grinding aid in cement is a chemical additive that is used during the milling process to improve the efficiency and effectiveness of the grinding of cement clinker and gypsum. A reducing agent added to reduce the emission of harmful oxides, such as nitrogen oxides (NO_x) and sulfur oxides (SO_x).

The table containing the chemical and mineralogical characteristics of the CEM III/B used for the experiment can be found in table 4.4. Additionally, the Blaine fineness is provided, which quantifies the total surface area of all particles in a given mass of material and is a crucial parameter for determining the reactivity and strength development of cement.

Table 4.4: Chemical and mineralogical characteristics of used cement (ENCI, 2020).

	CEM III/B 42.5 N-LH/SR
CaO [%]	44
SiO_2 [%]	29.71
Al_2O_3 [%]	11
SO_3 [%]	1
SiO_2 [%]	2.79
Insoluble residue [%]	0.88
Loss on ignition [%]	0.6
Chloride [%]	0.07
Chromium [%]	0.07
Na_2O equivalent[1] [%]	1.15
Blaine fineness [m^2/kg]	457.2

[1] The calculated value is based on the average of the 2019 cement production plus two times the standard deviation.

The coefficient of thermal expansion (CTE) for this mortar mix design is expected to be slightly higher than the standard $1 \cdot 10^{-5}\,°C^{-1}$ as specified in the Eurocode for concrete. Coarse aggregate has a lower CTE compared to cement, as been discussed in subsection 2.3.2. Since mortar includes no coarse aggregate opposed to concrete, the CTE of mortar compared to concrete is expected to be higher. A particular study has measured the CTE of mortar made of CEM I using a dilatometer and

measured a value of $1.45 \cdot 10^{-5} \, °C^{-1}$ (Jeong et al., 2012).

4.1.3. Concrete mold

The mold for both the ADTM and TSTM consists of a back plate, two side plates, two dovetails at the ends and a front plate. These parts can be assembled using bolts. For the ADTM, all of these parts are 3D printed using stereolithography with white powder-based polyamide (PA 2200). The dovetails of the TSTM are made of steel as they must transfer the load applied to the specimen by the Instron. The temperature of the concrete during the test can be regulated using the cryostat. The cryostat circulates heated or cooled water through polyvinyl chloride (pvc) tubes which are connected to the polyamide mold parts. Water channels are present throughout all of these parts (except the dovetails) and a layer of copper is applied to the surface in contact with the concrete. This ensures that the concrete can be cooled or heated effectively because of the relatively high thermal conductivity of copper. Figure 4.4a shows the polyamide mold parts including water tube connections and copper contact surface. Figure 4.4b displays the polyamide and steel dovetail for the ADTM and TSTM respectively.

(a) Polyamide mold parts including water tube connections and copper contact surface

(b) Polyamide and steel dovetail
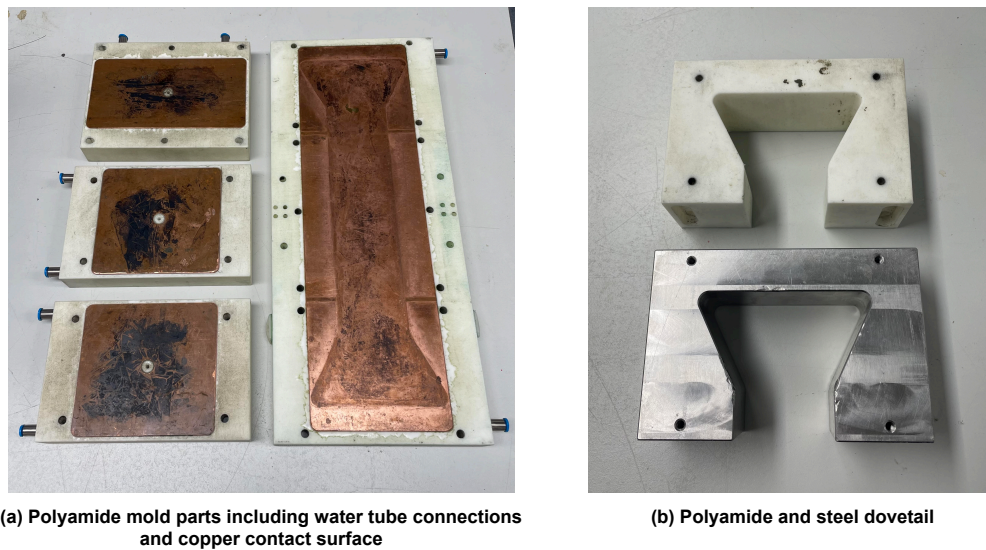
Figure 4.4: The ADTM and TSTM mold parts including steel dovetail and water tube connections

4.1.4. Instron and cryostat

During an experiment, the displacement of the specimen should be zero to simulate fixed boundary conditions. One method to achieve this is by directly controlling the deformation of the loading grip and keeping it at zero. However, slip between the specimen and the loading grip may occur, unintentionally allowing the specimen to expand or shrink. To eliminate the influence of slip, LVDTs are attached to the embedded bars, as shown in figure 4.2a, to measure the strain between these two bars. The measurement range equals ±1 mm with a precision of 1 μm. The deformation is then kept at zero using a PID control algorithm, which applies a counteracting load to the measured deformation.

Both the ADTM and TSTM molds have a small hole in the middle to allow for the installation of a temperature sensor. A thermocouple, consisting of two intertwined wires made of different types of metal, is fitted through this hole and measures the core temperature of the concrete with a precision of 0.05 °C. An objective function for the temperature over time can be set and regulated with a PID controller and a cryostat. The cryostat, which has a reservoir of water that can be heated or cooled, circulates this water through the channels of the molds. This ensures that the temperature at the center of the specimen follows the set temperature profile (Liang, 2024).

4.2. Experimental procedure of mini-TSTM test

Preparatory work for conducting a mini-TSTM test includes assembling the reinforcement. First, twelve threaded bars should be cut to a length of 300 mm and then be placed and fixed inside of the mold. Following standard construction practices, concrete spacers are used to fix the reinforcement at a specific distance from the surface. However, once the mold with fresh concrete is positioned vertically after the initial setting time, the reinforcement no longer rests on top of the spacers. The initial idea was to make end plates out of wood, drill holes through them, and fit the end plates and reinforcement inside the mold. Two problems arose during trial tests. The first issue occurs when the specimen is under compression. The reinforcement protrudes from the wooden end plates, causing the Instron to apply the load directly onto the reinforcement. Due to the threaded bars not being perfectly centered and of varying lengths, bending moments were introduced during the test. These bending moments can lead to instability. The second problem occurs when the specimen is under tension. Since the bars are not fixed to the end plates, pull-out of the threaded bars was observed. The force distribution difference between fixed and loose reinforcement is depicted in figure 4.5.

Another idea was to put plates or another contraption anywhere else inside of the mold to avoid any instability because of plates at the ends of the mold. The difficulty with this solution is keeping the mortar continuous at these locations.
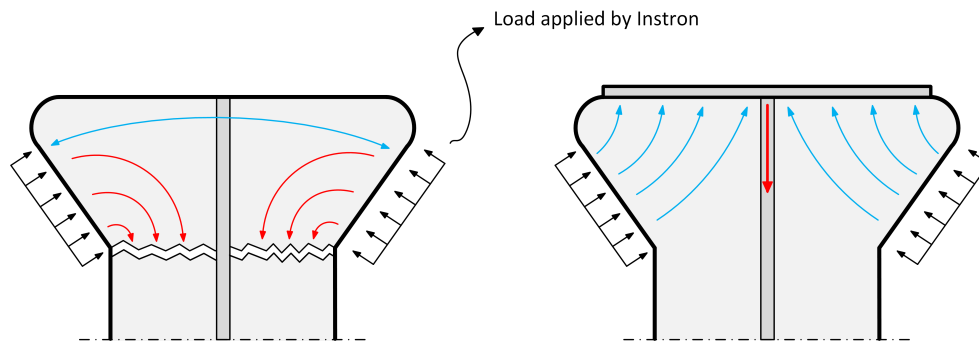
Figure 4.5: Force distribution in concrete dovetail with (right) and without (left) fixing reinforcement.

It should be noted that six threaded bars are used during the test, but the figure above simplifies this to a single bar. To address the issues with wooden end plates, a different method for fixing the reinforcement was implemented. Steel plates with a thickness of 2 mm were used, and the reinforcement was attached to the plates rather than passing through them. Applying a nut to the threaded bars and soldering them to the steel plate was unsuccessful because the tin did not adhere to the steel. Instead, an adhesive was used called Pedikit 860, a two-component adhesive manufactured by Permacol B.V. Industrial Adhesives. Figure 4.6 illustrates how the wooden and steel end plates are fitted inside the mold.
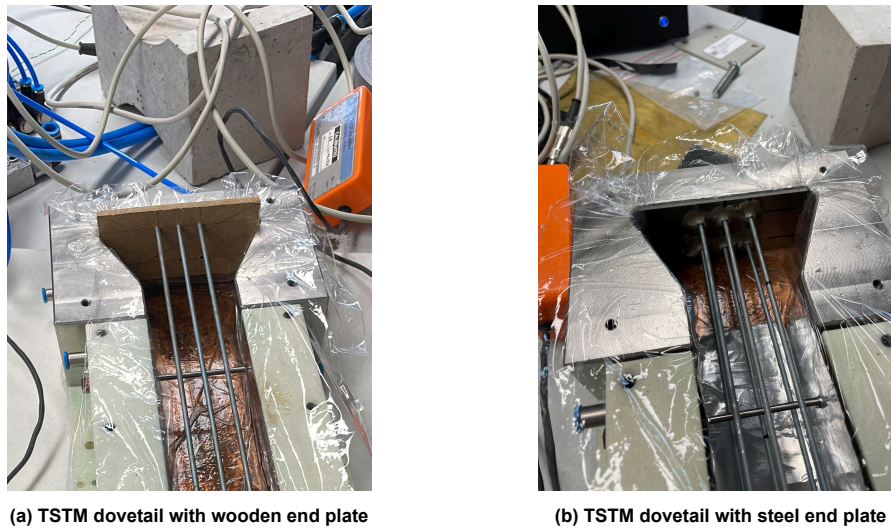
(a) TSTM dovetail with wooden end plate

(b) TSTM dovetail with steel end plate

Figure 4.6: Difference between wooden and steel end plate, respectively loose and fixed connection, including reinforcement.

The steel end plates effectively prevent the concrete dovetails from being pulled off the concrete, as observed in trial tests. This contrasts with the performance of the dogbone specimen fitted with wooden end plates. In the trial tests, the maximum force observed did not exceed the limit of the Instron loading machine, reaching only around 8 kN. It was noted that the concrete dovetail was pulled off the reinforcement, as it is not fixed to the end plate. Figure 4.7 illustrates the dovetail being pulled off the reinforcement. The observed cracks suggest that the stress distribution shown in figure 4.5 is accurate. The conclusion drawn from these trial tests, is that the actual mini-TSTM experiments should be equipped with steel end plates with the reinforcement glued to these plates. This should be done to prevent the dovetails from being pulled of the reinforcement and not reaching the Instron loading capacity.

Figure 4.7: The dovetail pulled off the reinforcement during a trial test.

To initiate a test, one needs to first assemble the back plate of the mold, the dovetails and the two sides of the mold using bolts. Then, the inside of the mold is lubricated using oil after which a sheet of plastic film is applied. This helps minimizing the friction between the mold and the specimen, prevents concrete or mortar from entering the crevices of the mold and prevents drying shrinkage. During trial tests, it was observed that the surface of the mortar specimen was wrinkled due to do the wrinkles in the plastic film. These wrinkles reduce the effective concrete area and will cause cracks to form at sections where this area is smallest. Thin aluminum tape is placed on all four side of the narrow part

of the specimen, as shown in figure 4.8, to ensure that the mortar is smooth on these surfaces.
The next step involves the assembly of the reinforcement. The threaded bars and steel plates should
be cut to the right length and then attached to one another using the two-component adhesive. The
reinforcement is then placed inside of the mold along with the embedded bars which should be pierced
through the plastic film and aluminum tape.

The mold is then ready to be filled. The first step involves dry mixing the cement and sand for one
minute using a Hobart mixer. Next, the water should be gradually added to the dry mix, and the entire
mixture should be mixed for another minute. Since the blade of the Hobart mixer does not reach the
bottom and sides of the bowl, the bowl should be scraped and then mixed briefly again to homogenize
the mortar. Subsequently, the mortar is added into the mold in stages. During each stage, the mortar
should be compacted, as good bond strength between the steel and mortar cannot be guaranteed oth-
erwise. In this experiment, the entire mold is placed on a vibration table to ensure proper compaction.
Once this step is done, another piece of aluminum tape is put on top of the straight part of the dogbone
after which the plastic film is closed.
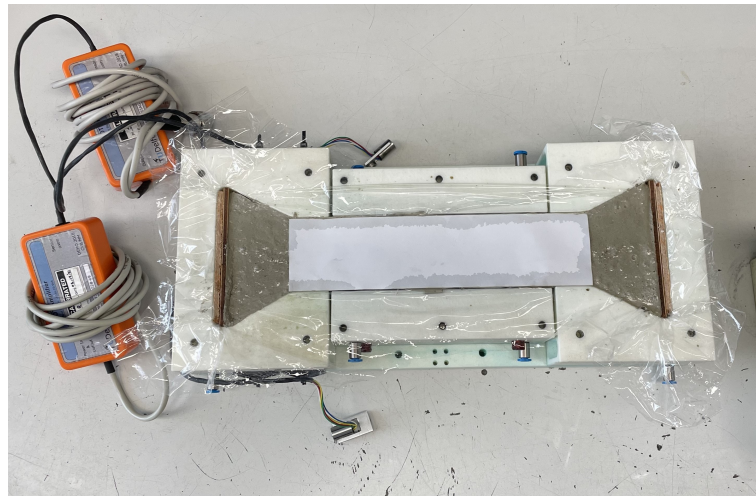
**Figure 4.8: The ADTM mold after casting, compacting and putting a piece of aluminum tape over the narrow part of the
specimen.**

Then, a hole is made in the middle using a screwdriver to insert the thermocouple. The thermocouple
should be threaded through the mold and then inserted inside of the fresh concrete. The three plates
forming the top of the mold are secured using bolts and then both the TSTM and ADTM are ready for
the next stage of the experiment. Still in horizontal position, six inlet and outlet tubes of the cryostat
should be connected to the plates, ensuring that each plate is connected to an inlet tube and an outlet
tube. The cryostat can be turned on afterwards and will start to circulate water through the plates. If
there are no leakages, a temperature curve can be initialized and one should ensure that the feedback
loop is activated so that the temperature of both the ADTM and TSTM follow the specified temperature
curve.
During the previous steps, the mold is in a horizontal position because the concrete is still fresh. The
molds can be put vertically after its plasticity is lost which corresponds to the initial setting time. This
should not be confused with the final setting time, this is when the mixture is starting to gain strength
(Zhang, 2011). The initial setting time is around $3 - 4$ hours and after this period both the ADTM and
TSTM are put in the vertical position. The TSTM mold is fixed inside of the Instron and the ADTM on
any flat surface. The four bolts at the top of the back plate are removed on both the ADTM and TSTM
and the six bolts at the middle are loosened. This is done to allow the dovetail to move freely and
removing the lateral constraint of the middle part as described by Liang (2024). The LVDTs are then
attached to the embedded bars, calibrated using a computer and it should be checked whether their
measurements behave as expected using the Instron. The setup of the ADTM and TSTM after these
steps is illustrated in figure 4.9.
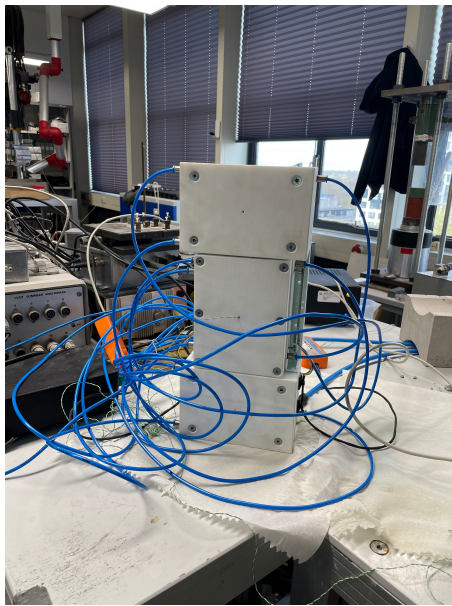
(a) ADTM with cryostat tubes connected and installed LVDTs.
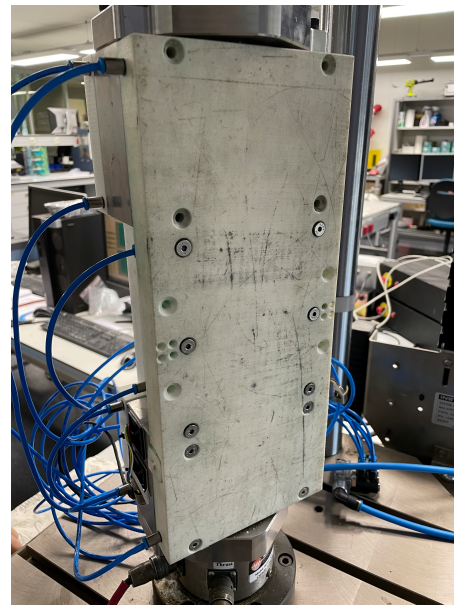
(b) TSTM back plate with removed bolts at the top and loosened bolts in the middle.

Figure 4.9: Setup of the ADTM and TSTM after the initial setting time has passed.

Once the setup is complete, the experiment can begin by setting the Instron to strain control mode. The Instron will then actively maintain zero strain between the LVDTs by applying counteracting loads when any strain is detected. It is important to verify that this is happening; the force and measured strain should behave in opposite ways. If they do not, the experiment is unstable.

A day after the mortar has been mixed, the front plate can be removed to paint the front surface white for DIC analysis. First, the plastic sheeting is opened and then the aluminium tape is removed. The concrete surface is then smoothened using a putty knife to ensure the speckle pattern can be applied correctly. With the front plate removed, the specimen will rapidly lose heat to the surrounding air, as it has already reached a significant temperature. Although no significant tensile stresses will occur since the specimen is under compression during the heating process, this situation is still undesirable. The maturity of both specimens should be comparable, and the cryostat will try to compensate and heat up as the average temperature of both specimens decreases.

The drying process can be accelerated by using a heat gun on the painted surface. Once the white paint layer has dried, a black speckle pattern can be applied with a black permanent marker, ensuring the dotted pattern is sufficiently dense. After completing the speckle pattern, the plastic sheeting is put back in place and the front plate is refitted. The next step is to wait for the moment to apply the mechanical load, the front plate is then taken off again to perform the DIC analysis. At this point, the camera is set up with adequate resolution and correctly focused on the dogbone specimen. The camera is programmed to take images at specific intervals, synchronized with the application of the load on the specimen. Displacement control is used to allow the force to decrease at the onset of each crack.

The final step is to stop the experiment, which involves several actions: the Instron is set to position control, the LVDTs are disconnected, the bolts connecting the Instron to the TSTM are removed, the bolts securing the mold parts are removed, the cryostat tubes are disconnected, and the mold parts are cleaned. Afterward, the DIC data is analyzed for further investigation.

$$5$$

Experimental results

The experimental results are divided into two main parts: the general mortar properties and the cracking analysis of the mini-TSTM experiments. Given that time is a crucial variable and varies significantly across different experiments, a maturity method will be used to establish a link between time and the development of the mortar's strength and elastic modulus. Various maturity methods are available, with some being more accurate than others, depending on the underlying principles. The CTE is an unknown but critical constant, as it governs the imposed deformation force during the experiments. The ADTM data can provide an estimate of this quantity by analyzing the free deformation and the temperature differential during the test. Autogenous shrinkage can then be determined, as the total deformation is the sum of thermal deformation and autogenous shrinkage.

The second part of this chapter focuses on the cracking behavior observed during the various experiments. This analysis involves examining the data collected from the Instron machine alongside the results from the DIC analysis and optical microscope images. The observed crack widths will then be compared to the predicted crack widths derived from the structural design codes and guidelines discussed in chapter 3.

5.1. General mortar properties

5.1.1. Weighted maturity

Three distinct mini-TSTM tests were performed in this thesis, each subjected to a 10 kN load at different time intervals relative to the initial setting time. Consequently, the mortar properties differed across these three tests. To relate these tests to each other, the maturity of the mortar was determined. There are various maturity methods, each based on different principles. Examples include the Nurse-Saul, Rastrup, Weaver and Sadgrove, Arrhenius, and Dutch weighted maturity method. These methods assess the maturity of concrete, which indicates the development of its material properties. While maturity is naturally time-dependent, it is also influenced by temperature. In this research, the Dutch weighted maturity function was chosen, as expressed in equation 5.1 (Borsje and Prins, 2002).

$$R_g = \frac{10\left(C^{0.1T-1.245} - C^{-2.245}\right)}{\ln(C)} \tag{5.1}$$

where:

R_g = the weighted maturity during a period of 1 hour (°Ch)
T = the average temperature of concrete during the specific hour
C = cement specific constant

The term $0.1T - 1.245$ in the above equation accounts for the non-linear effect of temperature on maturity. The cement-specific constant C varies for each mortar or concrete mixture and must be determined experimentally. For CEM III/B 42.5, this constant has been established as 1.55 by Borsje and Prins (2002) and will be used in this research. Although this method considers mixture dependency, unlike the Nurse-Saul, Rastrup, and Weaver and Sadgrove methods, it does not account for activation energy

dependency. The Arrhenius method does include activation energy in its calculations, but implementing it would require additional testing, which is not deemed necessary for the scope of this research (Soutsos et al., 2018).

The weighted maturity curve can be constructed once the temperature profile is known. In this research, it is essential for the specimen to reach a fully developed crack pattern. An estimation for the required strain to achieve this pattern is provided in equation 3.25. By assuming a conservative value for the mortar's tensile strength, an approximate coefficient of thermal expansion, and neglecting autogenous shrinkage, a required temperature differential ΔT of 46.7 °C is estimated. However, the developer of the mini-TSTM advised against exceeding a temperature of 50 °C to avoid negatively impacting the cryostat system. Consequently, a temperature profile for a real structure was adjusted to start at 20 °C, peak at 50 °C, and then cool down to 10 °C. Although the estimated temperature differential is not fully reached with this profile, the assumptions made are conservative. Therefore, it is still expected that the fully developed crack pattern will be achieved using this temperature curve. The temperature profile used during the experiments is shown in figure 5.1.
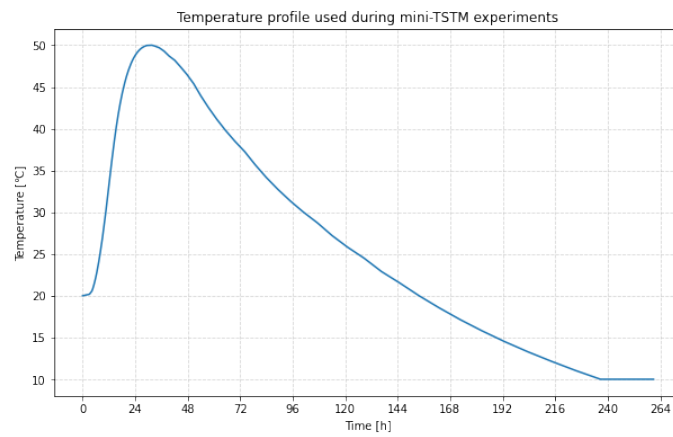
Figure 5.1: The temperature profile used for the experiments to be performed for this research.

The weighted maturity over time can be computed using Python by taking the hourly average mortar temperature and a *C* value of 1.55. The results of this computation is found in figure 5.2.
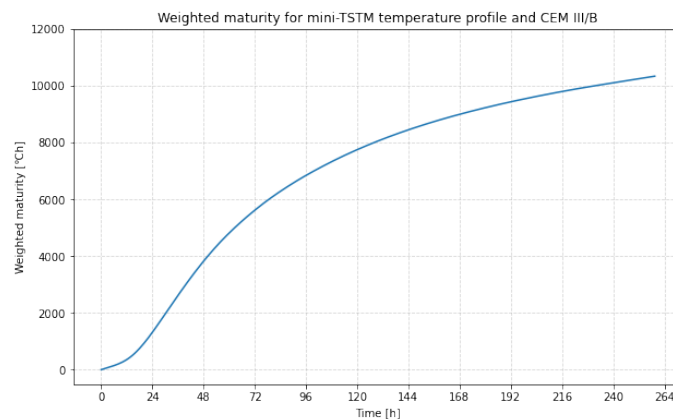
Figure 5.2: The weighted maturity for the specific temperature profile and cement used.

Four different experiments were conducted, each with an ADTM specimen and a TSTM specimen. Three of those experiments had steel end plates and one of them with wooden end plates. The ADTM mechanical test of one of the three test with steel end plates failed which is why the test using wooden end plates is used. This test in not usable for crack width analysis, but is useful for maturity analysis. The experimental procedures of the three usable experiments were as follows:

1. **Experiment no. 1:** This experiment has the wooden end plates and was stopped when the imposed deformation in the TSTM caused one crack between the LVDTs. This ensured that the crack propagation phase was reached, but not yet the fully developed crack pattern. After this point, both specimens were gradually loaded to 10 kN using the Instron loading machine. The TSTM specimen started at the load caused by the imposed deformation, while the ADTM started at zero load.

2. **Experiment no. 2:** This experiment was stopped when the TSTM specimen remained in the uncracked phase. Subsequently, both the ADTM and TSTM specimens were gradually loaded to 10 kN.

3. **Experiment no. 3:** This experiment concluded after two cracks had formed in the TSTM specimen and similarly to the other experiment, mechanically loaded.

From these tests, three different maturities were recorded along with six tensile strengths at which the first crack occurred. Typically, calibration lines are constructed using the compressive strength of specific concrete mixtures at different maturities. Although it is not possible to retrieve the compressive strengths of the ADTM and TSTM specimens from the obtained results, it is feasible and potentially more useful to construct a calibration line using the tensile strengths at different maturities.

Table 5.1: Tensile strength at onset of cracking with corresponding weighted maturities

Test no.	ADTM strength [kN]	TSTM strength [kN]	Weighted maturity [°Ch]
1	3.124	6.373	4445
2	1.490	5.872	2175
3	4.960	7.954	5781

From the data listed in table 5.1 it is apparent that the first crack in the ADTM specimens is structurally at a lower force compared to the TSTM specimens. One of the differences between the ADTM and TSTM is the loading duration. The ADTM experiences no load as it is free to shrink and expand, while the imposed deformation load in the TSTM is gradually increasing for a duration ranging from hours to even days. However, it is known that the strength of concrete is higher for loads applied in a short duration compared to loads applied over a long term. This contradicts the observed data.

The reason could be due to the variability of the strength of concrete. The reason is however deemed more likely to be the attributed to the way how the first crack is registered in the ADTM and TSTM tests. For the TSTM, the first crack has to be between the LVDTs as this is the region of interest for this research. It should be noted that stress peaks occur in the disturbed region between the dovetail and the narrow part of the specimen. It is likely that the first crack in both the ADTM and TSTM occurs at these disturbed regions and that the first registered crack between the LVDTs in the TSTM, is not truly the first crack in the entire specimen.

Therefore, averaging the tensile strength of the ADTM and TSTM would not be valid. A calibration line for both the ADTM and TSTM is constructed and the results are visualized in figure 5.3.
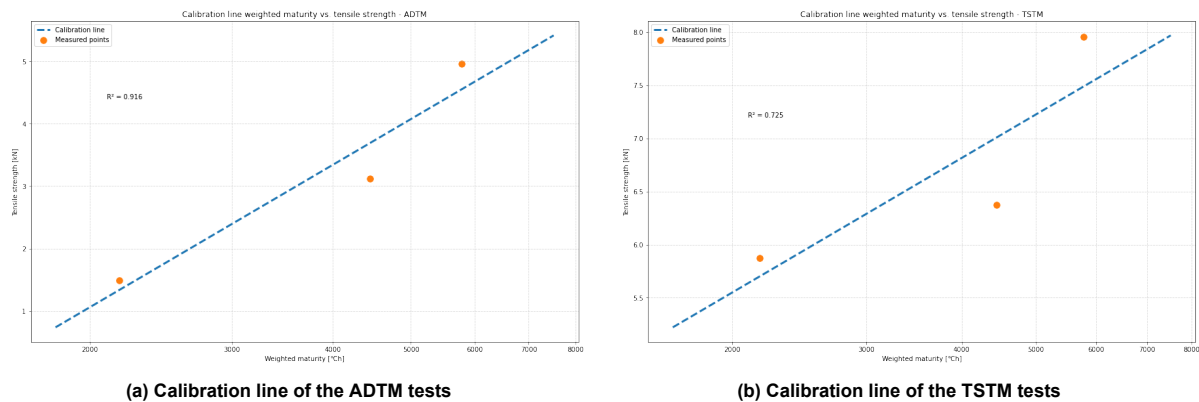

(a) Calibration line of the ADTM tests   (b) Calibration line of the TSTM tests

Figure 5.3: Calibration line linking the maturity of the used mortar and its tensile strength.

5.1.2. Coefficient of thermal expansion

Thermal deformation is directly linked to the coefficient of thermal expansion as discussed in subsection 2.3.2. The CTE determines the strain imposed by a temperature increase ΔT. It is largest directly during curing and decreases linearly until a stable value after 8-10 hours of curing. The deformation measured by the ADTM consists of two components; thermal deformation and autogenous shrinkage. Drying shrinkage is not present as the whole mortar specimen is concealed with plastic sheeting. The influence of autogenous deformation can be eliminated by conducting a test under a cyclic temperature profile. These short temperature changes result in measurable deformations, autogenous shrinkage is negligible in these short intervals (Liang, 2024).

Another experiment could be performed to accurately predict the coefficient of thermal expansion, however it is deemed sufficiently accurate for the research objectives of this research to predict the CTE using the obtained data. The CTE is non-linear during the first 8-10 hours making it an inadequate period to determine the CTE. Autogenous shrinkage supposedly decreases with time as figure 2.10 suggests, which is why the last stage of the experiment is most suitable to determine the CTE.

Data from two arbitrary ADTM tests are taken and the temperature and displacement measurements of the last three hours are analyzed. The linear CTE can be determined by determining the linear strain and temperature in the analyzed period. This is done by taking the least-squares linear fit through the measurements. The temperature and displacement of one of those tests are displayed in figure 5.4.

(a) Linear fitted temperature development

(b) Linear fitted deformation of the ADTM specimen
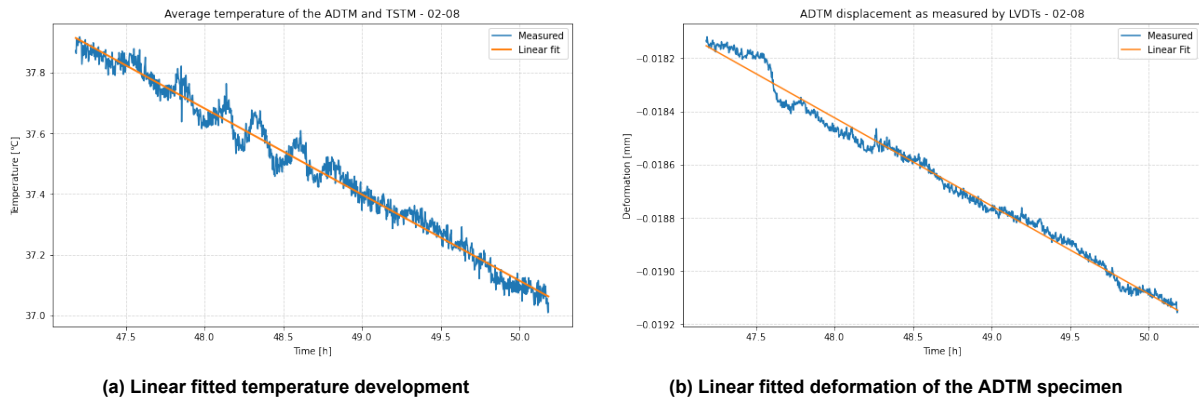
Figure 5.4: Temperature and deformation measurements of roughly the last three hours of the ADTM test on the 2nd of August.

The strain differential equals the deformation differential divided by the length of the specimen between the LVDTs:

$$\Delta\varepsilon = \frac{\Delta w}{l}$$

$$= \frac{\Delta w}{100\ [mm]}$$

(5.2)

The linear CTE is then determined by dividing the strain differential by the temperature differential. The average of the two ADTM tests is taken and equals to the following value:

$$\alpha_c = \frac{\Delta\varepsilon}{\Delta T}$$

$$= 1.2050 \cdot 10^{-5}\ [°C^{-1}]$$

(5.3)

The calculated value for the CTE α_c aligns with the expected values mentioned in subsection 2.3.2. It is higher than the value specified in NEN-EN 1992-1-1, which is $1 \cdot 10^{-5}\ °C^{-1}$ (NEN, 2020). It should be

noted that the value based on the obtained data does not account for autogenous shrinkage occurring during the considered period. The CTE can either be smaller or larger when autogenous deformation is considered, as the measured deformation is influenced by both thermal and autogenous deformations. As will become clear in the following subsection (see figure 5.5), autogenous deformation can result in either expansion or shrinkage during certain intervals. Depending on whether expansion or shrinkage occurs in the interval during which the CTE is determined, the CTE value will be either smaller or larger.

5.1.3. Autogenous shrinkage

The total deformation measured by the ADTM consists of thermal and autogenous deformation. This means that the autogenous deformation can be determined based on the determined CTE in the latter subsection. The thermal strain at any point during an experiment can be calculated by taking the temperature at that moment, subtracting the initial temperature and then multiplying this value with the linear CTE:

$$\varepsilon_{T,j} = (T_j - T_{initial}) \cdot \alpha_c \tag{5.4}$$

The results of computing the autogenous deformation for each of the three successful TSTM experiments are found in appendix A. Figure 5.5 displays the autogenous deformation for the TSTM experiment finished on the second of August.
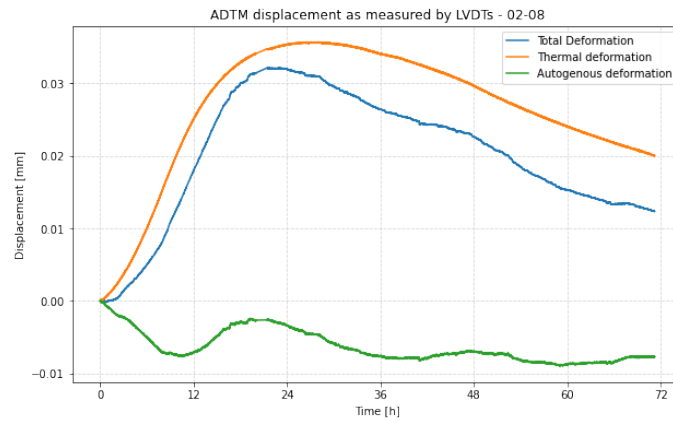
Figure 5.5: The autogenous deformation based on the total deformation of the ADTM and the determined CTE.

The autogenous deformation development observed in the figure above is not in line with figure 2.10 where the curve is concave, starting at the final setting time. Figure 5.5 shows that the specimen is shrinking in roughly the first ten hours, then it expands until hour twenty and finally the concave shrinkage is visible. These characteristics have also been observed by Liang (2024), looking at figure 6-3e, almost the exact same autogenous shrinkage characteristics can be observed.

The main difference between the latter mentioned figure and figure 5.5 is the magnitude of the autogenous shrinkage. Figure 6-3e of Liang (2024) has a maximum of 110 µstrain after 45 hours of curing at 30 °C. This would be 0.0110 mm compared to a maximum of 0.0080 mm observed in figure 5.5. This is because of the different types of cements and different water to cement ratios. Moreover, the linear CTE determined in this research is likely less accurate because no specific test was performed.

Liang (2024) distinguishes four phases of autogenous shrinkage, known as the four-stage process, thus owing its name to this classification. The material is still plastic during the first stage and experiences high creep. The deformation in this stage is highly uncertain as observed in different tests and this is also seen in the graphs in appendix A. The second stage in which the mortar expands is characterized by crystal growth such as ettringite and calcium hydroxide. The third stage denotes the stage of transition from autogenous expansion to self-desiccation shrinkage. This stage is significant for low curing temperatures (< 30 °C) and is not present at higher temperatures. Figure 5.5 does not show this stage and is in line which the observation that the third stage is not present at high curing temper-

atures. The fourth and final stage is where autogenous shrinkage occurs and due to the developed elastic modulus, cracking may happen.

5.2. Cracking analysis - mini-TSTM experiments

5.2.1. Experiment 1 - no imposed deformation cracks

The goal of the first experiment is to ensure that the specimen remains uncracked before the mechanical tensile test is performed. Although some stress from imposed deformation will be induced, the mechanical test should occur before any cracking results from this deformation. The imposed deformation is driven by autogenous shrinkage and thermal shrinkage, as the TSTM specimen cools down after reaching peak temperature.

Initially, the TSTM is set to strain control directly after the initial setting time in accordance with Liang (2024). However, the test did not reach a stable situation. This is likely due to the low elastic modulus of the concrete causing the specimen to compress due to its own mass. A compressive strain is registered by the LVDTs meaning that a tensile force is delivered by the Instron to counteract the compression of the specimen. Another reason for instability is because the mortar has a low elastic modulus during this stage and the steel reinforcing bars have a relatively large elastic modulus (205 GPa). This means that the force of the Instron is acting purely on the reinforcing bars as the mortar hardly has any load bearing capacity yet. The steel bars will always have some eccentricities, meaning that bending moments will occur. Without setting a limit to the tensile force of the Instron, this would cause the Instron to suddenly apply its maximum force onto the specimen, essentially failing the experiment.

Therefore, it was decided for this experiment and the experiments to come, to start strain controlling after around 24 hours after casting the mortar. This ensures that the mortar has a sufficient elastic modulus to not decompress under its own mass and to have load bearing capacity. The Instron was then set to position control after which strain control was started after 24 hours.

An assessment of autogenous shrinkage, force development, and tensile strength of the mortar was conducted through preliminary experiments. Although autogenous shrinkage was anticipated to be negligible, the experimental results indicated otherwise. The mechanical loading test was initiated the day after the mortar for the ADTM and TSTM specimens was mixed.

(a) Temperature over time of the ADTM and TSTM
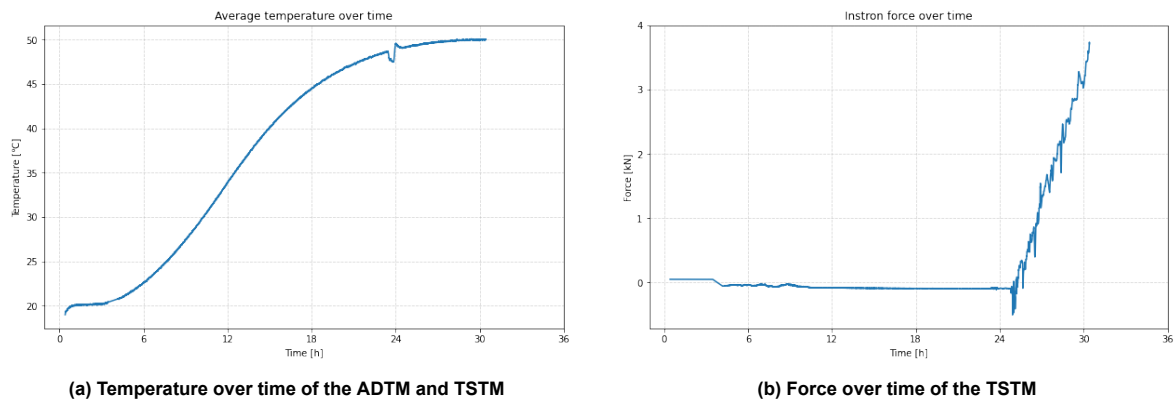
(b) Force over time of the TSTM

Figure 5.6: Temperature and force development of the TSTM experiment started on July 24.

The force on the TSTM specimen was allowed to increase up to approximately 3.5 kN, ensuring that the specimen remained in the uncracked phase. Figure 5.6a shows the temperature over time during the test and points out the temperature decrease at t = 23 hours which is credited to the front plate being removed for the speckle pattern application. The figure next to it, figure 5.6b shows the force development over the duration of the test. Interestingly from both figures, the 3.5 kN was reached while the test was still in the heating phase. The force increased from t = 25 hours until t = 30 hours because of autogenous shrinkage in combination with a relatively low temperature increase (~1 °C). The maturity of the mortar after 3.5 kN had been reached equals 2175 °Ch.
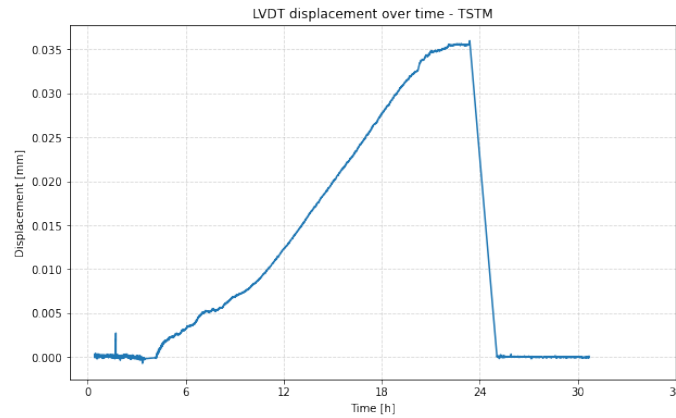
Figure 5.7: TSTM displacement over time measured by the LVDTs

Figure 5.7 shows the TSTM displacement between the LVDTs over time. From t = 0 until t = 24 hours, the loading grip of the Instron was set at a fixed position. Figure 5.7 reveals that the displacement between the LVDTs is not constant, in contrary to the loading grip. At t = 25 hours, the displacement was manually set to zero and the Instron was set to strain control, meaning that the loading grip actively counteracts any measured strain to keep the strain at zero. This is indeed the case, as the displacement is 0.000 mm from t = 25 hours until t = 31 hours when the long term test was stopped. Figure 5.6b shows a gradual increase in force with no significant drops, indicating that cracking has not yet occurred. Additionally, Figure 5.7 demonstrates a consistent displacement pattern from t = 25 hours and onwards, with no sudden changes that would typically signal the onset of cracking. This behavior aligns with expectations, as the test was stopped while the specimen remained uncracked.

At t = 31 hours the long term test was stopped and the next step of the experiment is to apply a mechanical load (short term) of 10 kN to the TSTM specimen. The Instron is displacement controlled, meaning that the displacement increases with a continuous rate while the force is allowed to decrease at the occurrence of cracks. A displacement rate of 0.001 mm per second was chosen for the mechanical test. The displacement rate determines how quickly the force increases and thus how long the total test will take. A balance between the displacement rate and photo frequency is crucial. A sufficient amount of photos is required for an accurate analysis but not too many as this will lead to redundancy and large data files. A photo was taken every 5 seconds during this tensile test. The data of the LVDTs and recorded force of the Instron, show the following results:
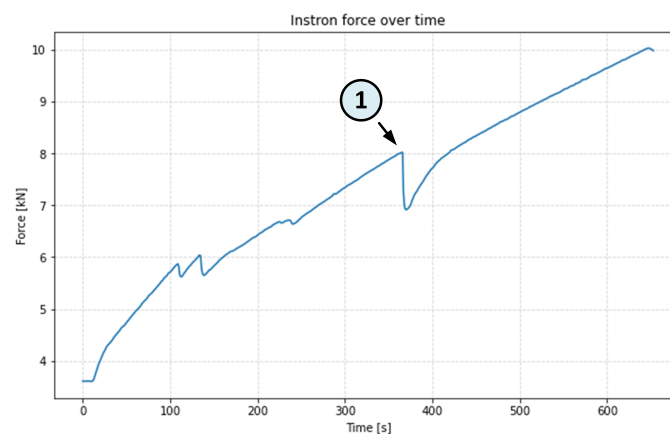

Figure 5.8: Force over time of the 10 kN mechanical test - Experiment 1

① See figure 5.10b for corresponding crack location

Figure 5.8 shows the force development over time during the mechanical test. The load starts at 3.5

kN, equivalent to where the long term test was stopped. Two cracks become apparent from this figure around t = 100 seconds. These are potentially located at the location where the dovetail and the narrow part of the specimen meet, leading to a stress concentration and therefore leading to the first cracks in the specimen. The slope at which the force progresses after these two cracks occurred is decreased compared to before. Since the displacement rate is constant throughout the test, this means that the stiffness of the specimen has decreased because of these two cracks. Some microcracks are visible at around t = 230 seconds, the force is not dropping significantly but the curve does show some disruption. Finally, a through crack between the LVDTs occurs at t = 370 seconds, indicated a significant drop in force of 1.1 kN and labelled in figure 5.8 with an encircled '1'. The force then steadily increases again until the load capacity of 10 kN has been reached at t = 650 seconds. The load versus displacement data will reveal more insights of the test and are displayed in figure 5.9a and figure 5.9b:

(a) Force versus displacement measured by the LVDTs　　　　　(b) Force versus loading grip displacement
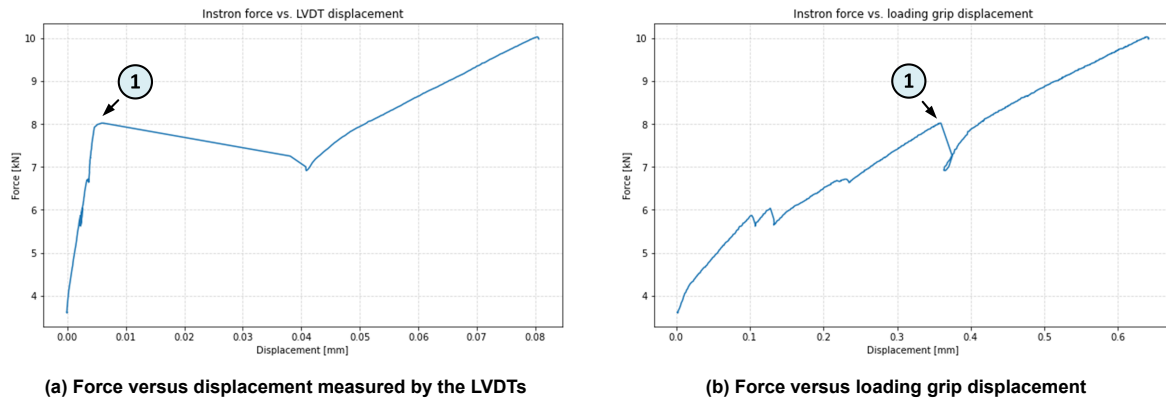
Figure 5.9: Force over time and versus displacement of the 10 kN tensile test - Experiment 1

① See figure 5.10b for corresponding crack location

Two smaller cracks formed between the LVDTs at 5.9 kN and 6.0 kN, shown in figure 5.9 and correspond with the two cracks in figure 5.8 at t = 100 seconds. The LVDT measurements in subfigure 5.9a do not show the same displacement increase as in subfigure 5.9b. The latter subfigure shows the load displacement curve of the loading grip of the Instron and this observation points out that these cracks occurred outside of the LVDT region. The through crack is again indicated with an encircled '1' in both subfigures and occurred at a load of 8.0 kN. This through crack formed between the LVDTs as the displacement in figure 5.9a suddenly increases by 0.036 mm or 36 μm. The stiffness of the element is significantly decreases comparing the slopes before and after this through crack in figure 5.9a. The latter figure als reveals the final displacement difference between the LVDTs from the start until the end of the mechanical test: 80 μm. The displacement measured by the loading grip shows that the total deformation equals 540 μm, thus indicating that most of the deformation happens outside of the LVDT region.

The final source of information regarding the evolution of cracks is the DIC analysis. This analysis will reveal the strain and therefore also displacement of the region behind the middle front plate.

DIC analysis

A DIC analysis using the software GOM Correlate 2019 is performed in order to analyze the cracks in the TSTM specimen. Two important parameters in a DIC analysis are the facet size and point distance which dictate the accuracy of the analysis and the coverage. A smaller facet size increases accuracy and computational times as well as coverage. A larger facet size increases the ability of the analysis to correlate points with larger distances between them, but the analysis will lose data near the edges. A proper ratio between the facet size and point distance for this particular software equals 2:1. The facet size to point distance ratio is set at 30 pixels and 15 pixels respectively. Figure 5.10a shows the speckle pattern applied to the TSTM specimen during the second experiment and its coverage. The coverage is satisfactory as the analyzed region fully extends to the bottom and the top and only small parts of the edges are not able to be analyzed. Figure 5.11 shows the measured strain during the first picture, the occurrence of the first crack and at the final stage of the mechanical test.
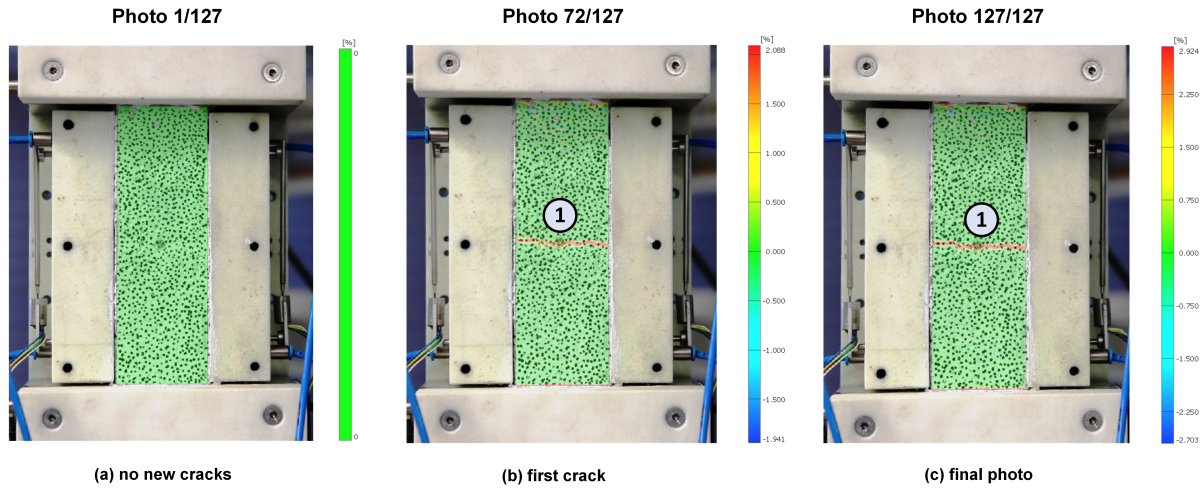
Figure 5.10: **Strain in y-direction as computed by the DIC software at different stages of the tensile test.**

The first new crack occurred at photo 72, which converts to 360 seconds after the start of the test. This corresponds with the significant drop in force in figure 5.8, which shows the force development over time. There are no other clear formations of cracks observed in the DIC analysis, however there are some red coloured regions at the top and even more at the bottom of figure 5.10b and 5.10c. This could either indicate inaccuracy of the analysis, the occurrence of a new crack or leftover plastic or aluminium tape deforming. It is expected that two cracks occur at the dovetails where the stress concentrations are located and one crack is clearly visible in the DIC analysis. Figure 5.8 and figure 5.9b show that three cracks have occurred during the mechanical test, which would indicate that the red coloured regions in figure 5.10c are no cracks. The photos also show that the aluminum tape and plastic sheeting are not completely removed on the top and bottom of the exposed area, supporting the fact that these red coloured regions are no cracks. The final and most obvious method to verify whether these red coloured regions, is using an optical microscope. This analysis will be presented in the following subsection.

The width of the through crack can be quantified using GOM by taking a longitudinal section through the middle of the specimen and analyzing the deformation along this section. By providing a reference distance in GOM, the software can correlate each pixel with a specific distance in millimeters, allowing for accurate measurement of the crack width. Figure 5.11 displays the longitudinal section. The y-axis represents the y-deformation, while the x-axis indicates the length of the analyzed region, approximately 150 mm. The point at x = 0 corresponds to the top of the area of interest, and x = 145 mm marks the bottom.
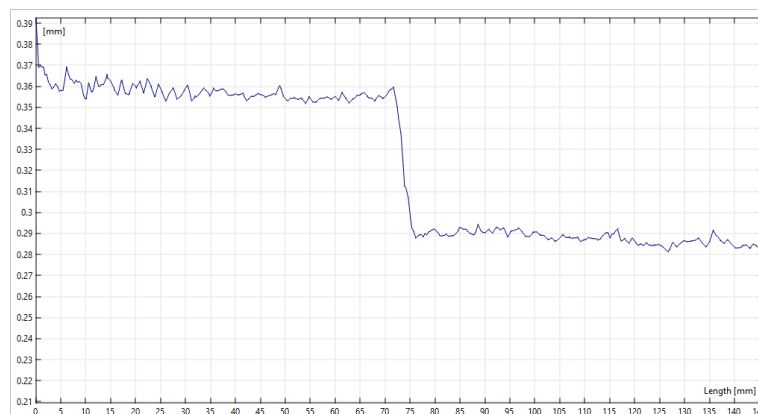

Figure 5.11: **The deformation in y-direction at the final photo of the DIC analysis.**

At x = 75 mm the deformation equals 0.288 mm and at x = 72 mm the deformation equals 0.360 mm, meaning that the crack has a width of 0.072 mm. The potential crack at the bottom of the specimen is not able to be quantified. The diagram of the y-deformation shown in figure 5.11 is of photo 127/127. To see how the crack evolves during the last stages of the test, the crack width has been determined at four photos and the result of this is shown in table 5.2.

Table 5.2: Crack width during the last stages of the tensile test

Photo no.	w_1 [mm]
112	0.066
117	0.067
122	0.067
127	0.072

Optical microscope analysis

The DIC analysis gives strong evidence of a new crack during the mechanical tensile test and shows red coloured regions on the top and bottom of the analyzed area (see figure 5.10c). To have a better understanding and be completely certain of the induced cracks, an analysis using an optical microscope can be performed. The optical microscope is able to visualize the cracks by magnifying the specimens. A VHX Digital Microscope (VHX-7100) was used with a VHX-E20 objective lens which has a magnification of 20-100x. This optical microscope analysis was performed more than five weeks after the tensile test was performed and initially did not show any signs of cracking. The reason is likely attributed to the autogenous healing capabilities of concrete and there are three reasons which support this claim:

CIRIA C766 section 2.6 discusses this phenomenon and uses a graph from BS EN 1992-3 showing that cracks of 0.2 mm without any external pressure will self-heal within a few weeks (Bamforth, 2019). The crack during the mechanical tensile test during the experiment had a width of 0.072 mm (see table 5.2) at maximum and after that the specimen was unloaded. The crack width of the unloaded specimen will be significantly smaller than 0.072 due to elasticity of the reinforced concrete element and therefore autogenous healing is certain to happen. Secondly, the mortar mix used in this research uses blast furnace slag cement (CEM III/B) and is known to slow the early age process of microstructure and strength development. Research shows that due to this characteristic, the capability of autogenous healing is significantly higher compared to Portland cement (CEM I), which also explains why no signs of cracking were observed (Van Tittelboom et al., 2012). Finally, the weighted maturity of this experiment at the start of the mechanical test is rather low (2175 °Ch). This indicates that the early age development has not yet been finished. Unhydrated cement will therefore still continue to hydrate which increases the autogenous healing capabilities of the specimen.

The adopted solution to the cracks being self-healed over time and therefore not being visible anymore, is to apply load the specimens once more, to open the cracks which had previously formed. The cracks in the specimens were then indeed able to be observed using the optical microscope. The whole speckle pattern can be visualized using three dimensional (3D) stitching and the result of this is shown in figure 5.12 on the left. The cracks are indicated using red lines and zoomed in images are shown on the right.
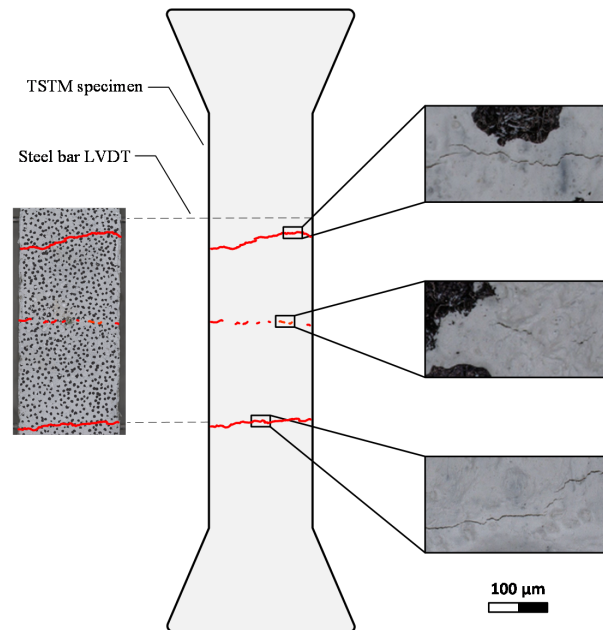
Figure 5.12: Stitched optical microscope image (left) including zoomed in images of cracks in the TSTM specimen (right)

Looking at the figure above, two clear cracks are visible at the top and bottom of the LVDT region and signs of the third crack in the middle. The top and bottom cracks were not present in the DIC strain analysis (see figure 5.10), this is explained by the Instron data obtained from opening the cracks once more. These data are presented in appendix C and figure C.2 shows the load versus the displacement measured by the LVDTs. The latter figure shows two sudden and significant increases in displacement, indicating the formation of two new through cracks between the LVDTs. This explains the top and bottom cracks in figure 5.12 not being present in the strain analysis using DIC in figure 5.10.

The second observation requiring further explanation is the less distinguishable crack in the middle compared to the more prominent top and bottom cracks. The middle crack had healed after the first tensile test, and it appears that the healing product inside the crack is stronger than the surrounding concrete. Cracks typically form at the weakest points of a tensile member, which explains why the top and bottom cracks are more pronounced, while the middle crack barely shows signs of reopening.
A plausible explanation for this behavior is the higher density and strength of the healing product compared to the original mortar. As the healing process progresses, the crack becomes filled with materials such as calcium carbonate and hydration products, resulting in a denser and more resilient zone. This increased density may prevent the healed crack from reopening under subsequent loading.
Moreover, as the healed area becomes stiffer or stronger, the stresses during reloading are likely redistributed to weaker regions of the concrete, leading to the formation of new cracks elsewhere. This redistribution of stress further supports why the healed crack remains closed while new cracks develop at different locations.

The optical microscope analysis confirmed the presence of the crack in the middle of the specimen, which was also observed in the DIC analysis (figure 5.10). The red regions seen at the top and bottom of the speckle pattern in figure 5.10c were proven not to be cracks based on the microscope images. New cracks formed during the reopening process, which indicates that the previously identified regions were not cracks, as those areas would not have allowed for new cracking.

5.2.2. Experiment 2 - one imposed deformation crack
The goal of the second experiment is to induce a single crack between the LVDTs through restrained thermal and autogenous shrinkage before applying a mechanical load to analyze the resulting crack widths. The corresponding force and temperature developments are shown in figure 5.13.
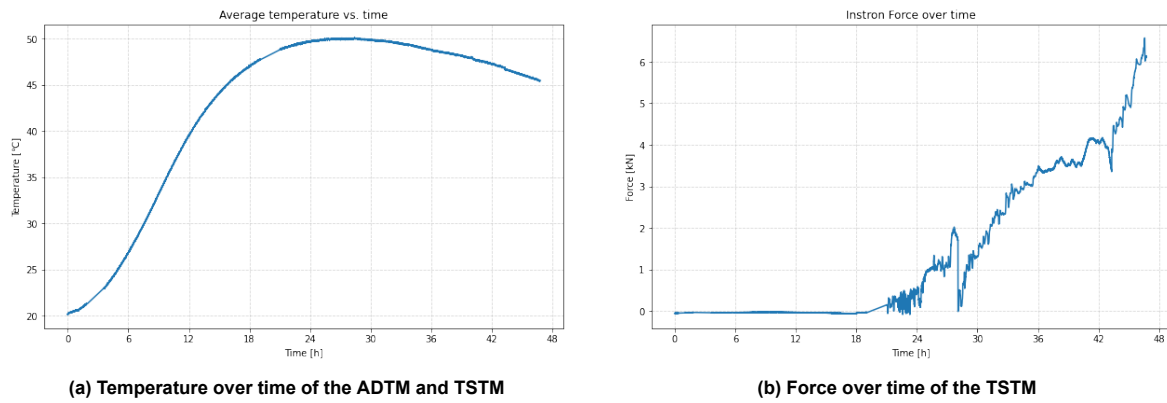
(a) Temperature over time of the ADTM and TSTM   (b) Force over time of the TSTM

Figure 5.13: Temperature and force development of the TSTM experiment started on July 8 until the first crack.

At 50 hours and 24 minutes after casting, the tensile force from the imposed thermal and autogenous shrinkage surpassed the tensile strength of the mortar in the region between the LVDTs. The plotted temperature data in Figure 5.13 does not start immediately after casting; therefore, the final points in the figure do not correspond to the true final time of 50 hours and 24 minutes. The initial hours of the test were omitted because the test was unstable during this period, and the data collected was not interpretable. Additionally, linear interpolation was applied to account for missing data between t = 2 hours and t = 4 hours, as well as between t = 19 hours and t = 21 hours when the DIC pattern was applied and no data was recorded. The temperature at which the imposed deformation crack occurred was 45.5 °C, and the weighted maturity at that time was 4036 °Ch, which is significantly higher compared to the first test (2175 °Ch).

Looking at the corresponding force development in figure 5.13b, it is observed that the force is increasing from t = 19 hours. This is the moment when strain control was active and stable. At t = 27 hours, the force drops from 2 kN to zero. Initially, the autogenous shrinkage was ought to be neglected. This would mean that the deformation is purely due to thermal differences. Using this logic, it was expected that the Instron would deliver a compressive force to counteract the thermal expansion during the heating of the mortar. Instead, a tensile load was observed already during the heating phase, the force was then brought back to zero to see whether the behaviour would continue. Then, it was realized that this phenomenon could be attributed to autogenous shrinkage which could thus not be neglected.

Another drop in the load is visible at t = 43 hours in figure 5.13b. This would suggest a crack, but instead this is due to an error which caused the strain control to be activated. This can be seen in figure 5.14a and will be further elaborated in the respective paragraph.

The force at which the specimen cracked between the LVDTs equals F = 6.573 kN and this crack should be detected by the LVDTs. Figure 5.14 illustrates the TSTM displacement as measured by the LVDTs during the whole experiment as well as during the last hours.
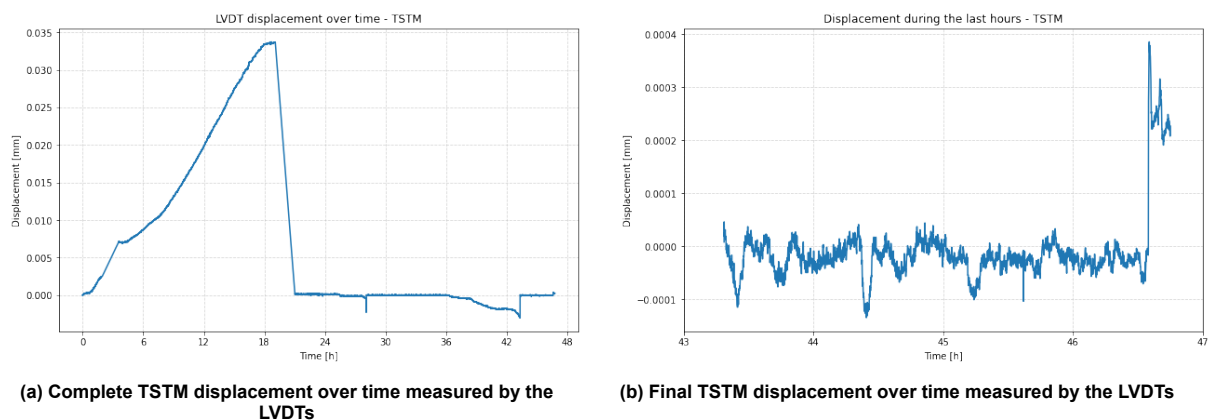

(a) Complete TSTM displacement over time measured by the LVDTs   (b) Final TSTM displacement over time measured by the LVDTs

Figure 5.14: Both the full TSTM displacement and during the last hours measured by the LVDTs.

During the first 19 hours when the TSTM was set to position control, the deformation between the LVDTs is increasing significantly during this period. It is clear that keeping the loading arm fixed does not cause the specimen to be restrained from deforming. The DIC speckle pattern has been applied at t = 19 hours and an hour later the Instron is set to strain control. The displacement was manually set to zero, explaining the jump from 0.034 mm to 0.000 mm. At t = 27 hours a decrease is visible corresponding to the force being set from 2 kN to zero shown in figure 5.13b. The deformation is correctly kept at zero apart from this sudden decrease until t = 36 hours. A load capacity had been reached during the night to prevent the force from excessive loads from occurring and to prevent sudden instability. Exceedance of the load capacity causes the Instron to set to position control and therefore the strain between the LVDTs is no longer kept at zero. A shrinkage deformation of 0.003 mm was reached in the morning (t = 43 hours) and then strain control was activated again. Figure 5.14 reveals a sudden increase in deformation along with a sudden decrease in force as seen in figure 5.13b, indicating a crack between the LVDTs. The long term test was therefore stopped as the goal for this experiment was to induce one crack between the LVDTs due to imposed deformation.

The next step of the experiment is to turn off the cryostat and to remove the front plate, revealing the DIC pattern underneath. Then, the camera is put into place with a remote attached, allowing photos to be taken at a certain frequency. The displacement rate of this test was set to 0.001 mm per second.

The 10 kN mechanical test was performed and the force over time including indicators for the occurrence of two through cracks is visualized in figure 5.15:
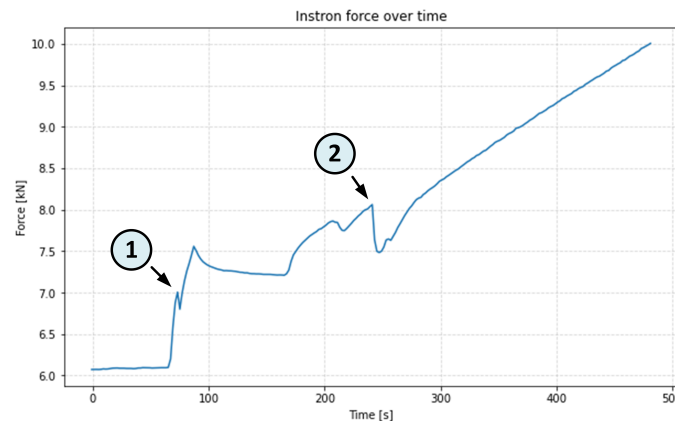

Figure 5.15: Force over time of the 10 kN mechanical test - Experiment 2

① See figure 5.17b for corresponding crack location

② See figure 5.17c for corresponding crack location

The figure above illustrates a rapid increase in load between 70 seconds and 90 seconds, with the load reaching 7.5 kN at t = 90 seconds. As this was the first experiment conducted, the optimal displacement rate had not yet been determined. The initial rate of 0.005 mm per second proved to be too rapid, prompting the test to be halted and then resumed at the correct rate of 0.001 mm per second. The first through crack, as will be made clear during the DIC analysis, occurs at 7.0 kN indicated by the encircled '1'. The second and final through-crack occurred at a load of 8.1 kN, as indicated by '2' in figure 5.15. Following this, the force dropped from 8.1 kN to 7.5 kN before gradually increasing again, reaching the test's final load of 10 kN. Minor drops in load, such as the one at t = 210 seconds, are indicative of microcracking in the specimen.

Additional insights are provided by the load-displacement data from both the LVDTs and the Instron's loading grip. These graphs are presented in figure 5.16a and figure 5.16b, respectively.
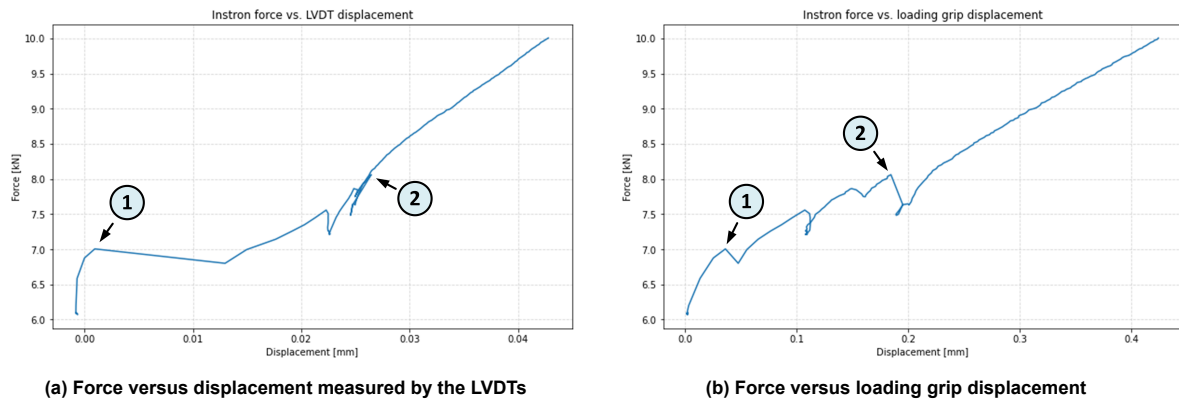
(a) Force versus displacement measured by the LVDTs

(b) Force versus loading grip displacement

Figure 5.16: Force versus displacement curves of the 10 kN tensile test - Experiment 2

① See figure 5.17b for corresponding crack location

② See figure 5.17c for corresponding crack location

In the first subfigure, figure 5.16a, an initial rapid load increase from 6.1 kN to 7.0 kN is observed. Following this, a decrease in load is accompanied by a significant increase in displacement, indicating the occurrence of a crack between the LVDTs. Based on the graph, the estimated crack width is approximately 0.013 mm (13 µm). The same crack is visible in figure 5.16b indicated with the encircled '1'.

A similar change in force and displacement can be observed, though it is important to note that the displacement scales differ between the graphs. A small load drop is visible at 7.6 kN in figure 5.16a, followed by the occurrence of a second and final through crack at 8.0 kN. Despite this, no significant increase in displacement is observed in figure 5.16a, which would typically be expected for cracks forming between the LVDTs. However, the DIC analysis (figure 5.17c) shows that the second crack occurred outside of the LVDT region, resulting in a slight displacement decrease measured by the LVDTs. Figure 5.17b displays a displacement increase, further confirming the presence of the crack at this load but outside the LVDT region. The load then gradually increases from 7.5 kN to 10.0 kN, marking the conclusion of the mechanical tensile test.

DIC analysis

For the DIC analysis of this experiment, the optimal facet size and point distance were determined to be 50 pixels and 25 pixels, respectively. The speckle pattern density was lower compared to the first experiment, requiring an increase in the facet size and point distance ratio. This increased ratio allows more points to be correlated, but it comes at the cost of reduced accuracy and limits the analysis of border regions. Figure 5.17a illustrates that the pattern quality at the top of the area of interest is poor. In contrast, the bottom of this area appears to have a satisfactory pattern, although no distinct dots are present; the software can still differentiate shades of black and white in this region.
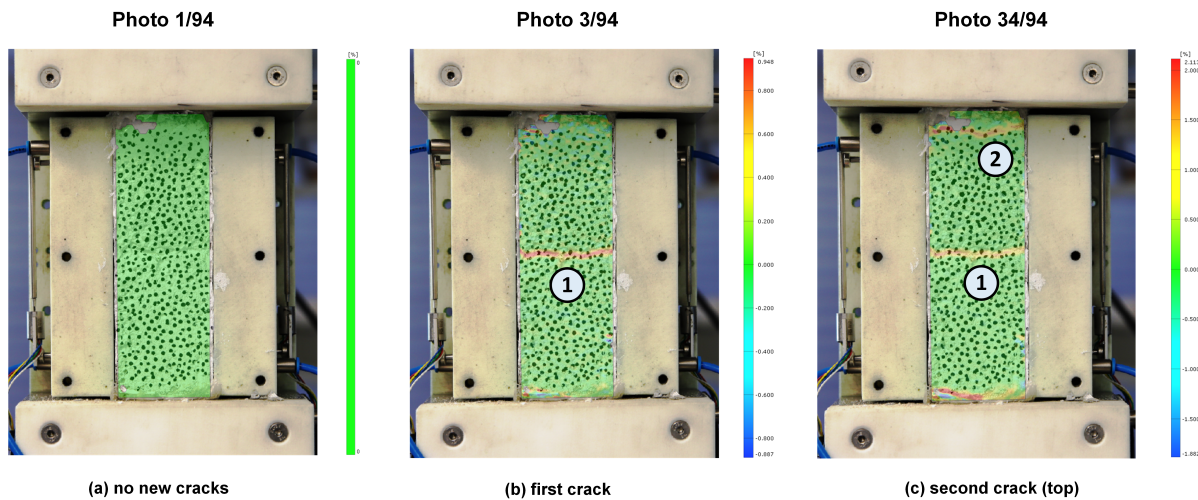
Figure 5.17: Strain in y-direction as computed by the DIC software at different cracks.

Looking at Figure 5.17c, one might assume a through crack is located at the bottom of the area of interest. However, there is leftover aluminum tape in this location, rendering the strain data unusable for further analysis. The first new crack occurs in the third photo, as shown in figure 5.17b, while the third and final crack appears in photo 34. The second crack is located outside the LVDT region, which is why there was no corresponding increase in the LVDT displacement data. The deformation in the y-direction at the final stage of the mechanical test (at 10 kN) can be computed using GOM and is presented in figure 5.18.
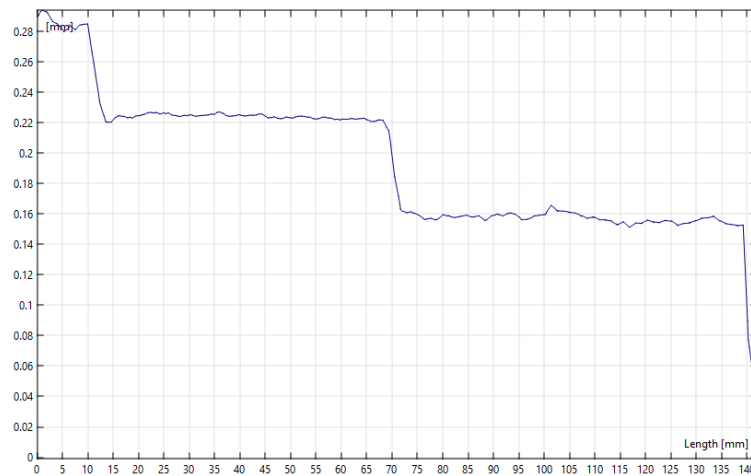
Figure 5.18: The deformation in y-direction at the final photo of the DIC analysis.

The y-axis in figure 5.18 represents the vertical deformation, while the x-axis denotes the length of the analyzed region, approximately 150 mm. The position at x = 0 corresponds to the top of the region of interest, and x = 140 mm indicates the bottom. The top and middle crack widths can be determined by the sudden jumps visible in the graph. The top crack has a width of 0.065 mm and the middle crack a width of 0.061 mm, averaging 0.063 mm. The crack widths during the final stages of the experiment have been recorded in the following table:

Table 5.3: Crack width during the last stages of the tensile test (w_1 top crack, w_2 bottom crack).

Photo no.	w_1 [mm]	w_2 [mm]	w_{avg} [mm]
79	0.062	0.055	0.059
84	0.064	0.056	0.060
89	0.062	0.059	0.061
94	0.065	0.061	0.063

Optical microscope analysis

To clarify the locations of actual cracks, an optical microscope analysis is also conducted for the second experiment. The cracks in the specimen were visible without reopening the cracks using the Instron, potentially because the load already exceeded 10 kN during the first mechanical test, causing plastic and irrecoverable strain in the steel reinforcement. A stitched image was created of the speckle pattern area and the cracks have been indicated using red lines. Figure 5.19 displays this image with zoomed in images of the individual cracks on the right of the figure.
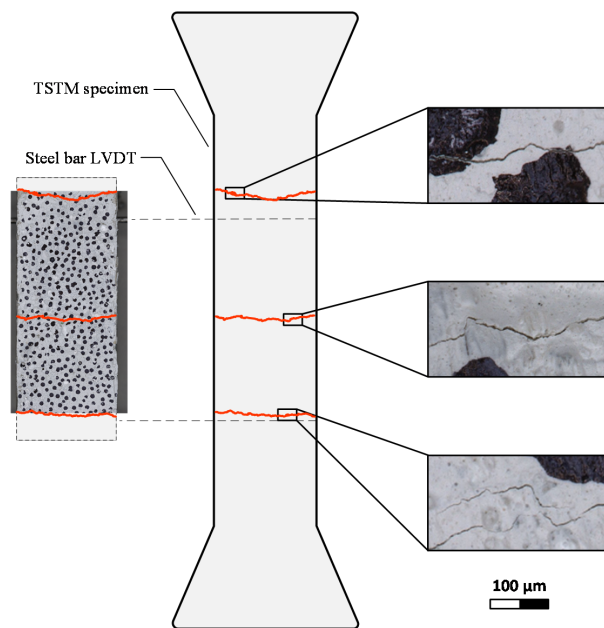
Figure 5.19: Stitched optical microscope image (left) including zoomed in images of cracks in the TSTM specimen (right)

The first observation regarding the figure above is that the maximum length for the stitched area is 100 mm. As a result, the top and bottom cracks could not be fully captured in the complete image; instead, individual images were taken to document each crack.

The crack at the top corresponds with crack 2 in the strain analysis using DIC (see figure 5.17). It is clearly visible that this crack is located just outside of the LVDT range (indicated using dotted lines in figure 5.19). The crack in the middle of figure 5.19 corresponds with crack 1 in the strain analysis using DIC.

The crack at the bottom of the specimen in figure 5.19 is not present in the DIC analysis (figure 5.17). This crack is located just above the bottom embedded bar to which the LVDT is attached while the red indicated region in the DIC analysis is well below this embedded bar. There are two possible explanations to why this crack is visible in the optical microscope analysis, but not in the DIC analysis: The first explanation is that this crack is the one which occurred due to the restrained imposed deformation during the long term test. The goal of this test was to induce one crack due to imposed deformation between the LVDTs. Since the DIC analysis shows strain relative to the first photo, it is possible that an already occurred crack does not show in the strain analysis. However, no visible crack was observed in the photos. Moreover, this crack would increase in width during the tensile test and therefore show

some strain at the last photo compared to the first photo. A more plausible explanation seems to be that the tensile test was conducted beyond the 10 kN mark which is reported in figure 5.16. The theoretical load capacity of the Instron is 10 kN, but the actual observed maximum is around 11.7 kN. The recorded data may have been stopped at 10 kN while the Instron kept increasing the displacement of the specimen to a higher. This crack might have been induced during that phase and therefore not being present in the data and DIC analysis, but does become apparent in the optical microscope analysis.

The optical microscope analysis has revealed several key findings: the first is the presence of the top and bottom of the specimen which were also present in the DIC analysis. The second finding is that the red region at the bottom of the DIC analysis is indeed not a crack, but rather the deformation of the leftover aluminium tape. The third and final finding includes the presence of a third crack just above the lower embedded bar. This crack is assumed to be formed after the data was stopped recording during the first mechanical test.

5.2.3. Experiment 3 - two imposed deformation cracks

The fraction of stress due to imposed deformation in the first experiment was relatively small as it remained in the uncracked stage. The second experiment experienced more stress due to imposed deformation and was mechanically tested when the specimen entered the crack propagation stage. The goal for the third and final experiment is to increase the fraction of imposed deformation stress even further. The TSTM specimen will be mechanically tested after two cracks have formed between the LVDTs due to restrained thermal and autogenous shrinkage. The necessary load due to imposed deformation is expected to be higher compared to the first two experiments and this was indeed the case. The temperature development along with the force during the long term test are presented in figure 5.20.

(a) Temperature over time of the ADTM and TSTM   (b) Force over time of the TSTM
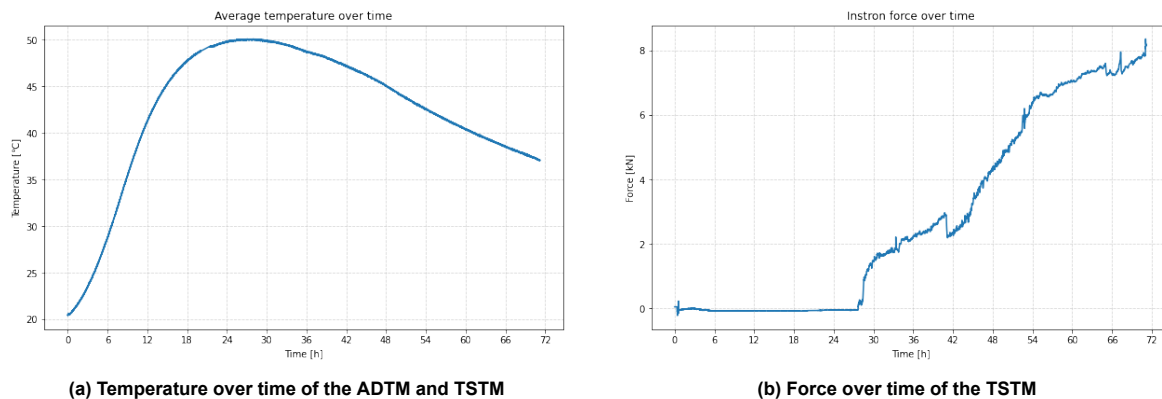
Figure 5.20: Temperature and force development of the TSTM experiment started on July 30.

The data presented in figure 5.20 indicates that the long term test was halted at a temperature of 37.01 °C, 74 hours and 50 minutes after casting (different from the figure as the initial hours are not included). The mortar had a maturity of 4445 °Ch at that moment. The initial hours of the experiment are not shown in these graphs, as no LVDT measurements were taken before the initial setting time was reached. Strain control was activated when the maximum temperature was reached. In the first and second experiment, strain control was active after the DIC pattern was applied.

Figure 5.20b shows that the force delivered by the Instron starts increasing from t = 28 hours, corresponding with the activation of strain control mode. The load then increases gradually until t = 41 hours at which a drop in the load occurs. The load drops with roughly 0.7 kN, not due to the occurrence of a through crack but rather because the manually set load capacity had been surpassed. Because of this, the strain was no longer kept at zero and manually had to be set to 0.000 mm, coinciding with the decrease in load. Afterwards, the load gradually increases again and at a load of 7.95 kN, a sudden load decrease and a displacement increase (see figure 5.21b) is visible at t = 67.5 hours. This is regarded to be the first through crack in the TSTM specimen. The second through crack follows shortly after the first one, at t = 71.3 hours. Suddenly the load decreases once more accompanied with

an increase in displacement between the LVDTs (see figure 5.21b). The force at which this second through crack occurred equals 8.36 kN. Both through cracks happened at a significantly higher tensile strength compared to the first and second experiment, but this can be attributed to the higher weighted maturity as determined in subsection 5.1.1.

The displacement measured between the LVDTs during the long term test is presented in figure 5.21. Figure 5.21a shows the whole test, while figure 5.21b shows the finals hours of the test to identify the increases in displacement due to the occurrence of the two through cracks.

(a) Complete TSTM displacement over time measured by the LVDTs

(b) Final TSTM displacement over time measured by the LVDTs
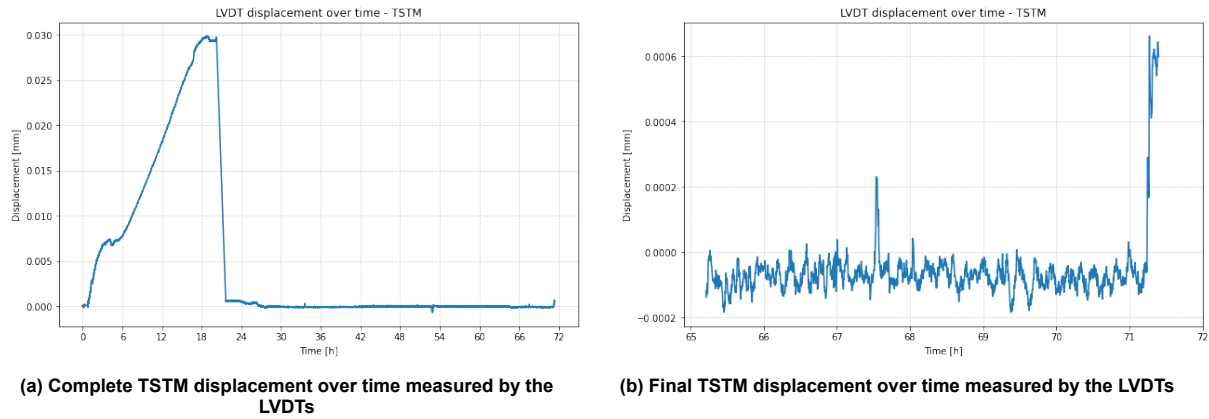
Figure 5.21: Both the full TSTM displacement and during the last hours measured by the LVDTs.

The Instron was set to position control from t = 0 to t = 20 hours and again the length between the LVDTs is not completely restrained because of this and rather shows a displacement of 30 μm, see figure 5.21a. This is a similar displacement compared to the first two experiments. The strain was then kept zero from t = 21 hours.

As mentioned before, the first through crack is considered to be formed at t = 67.5 hours and the second at t = 72.3 hours, as seen in figure 5.21b. At these points in time, the load decreases while the LVDTs detect and increase in displacement. The accuracy of the strain control (PID) can be seen from the latter figure as well, which is roughly 1 μm.

After the second crack had occurred, the test was stopped and then the mechanical test was performed. The recorded force over time data of this tensile test are presented in the figure 5.22 below:
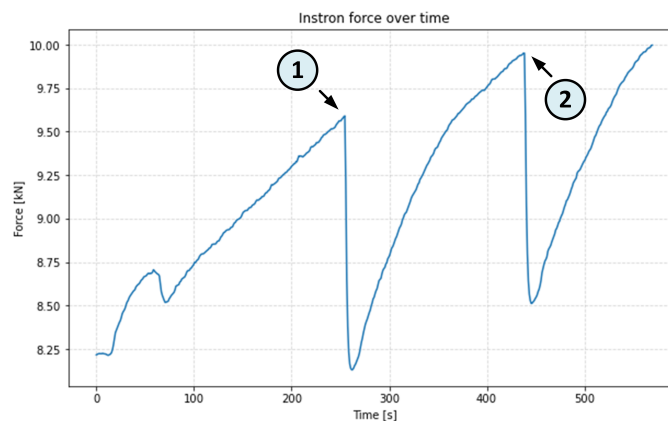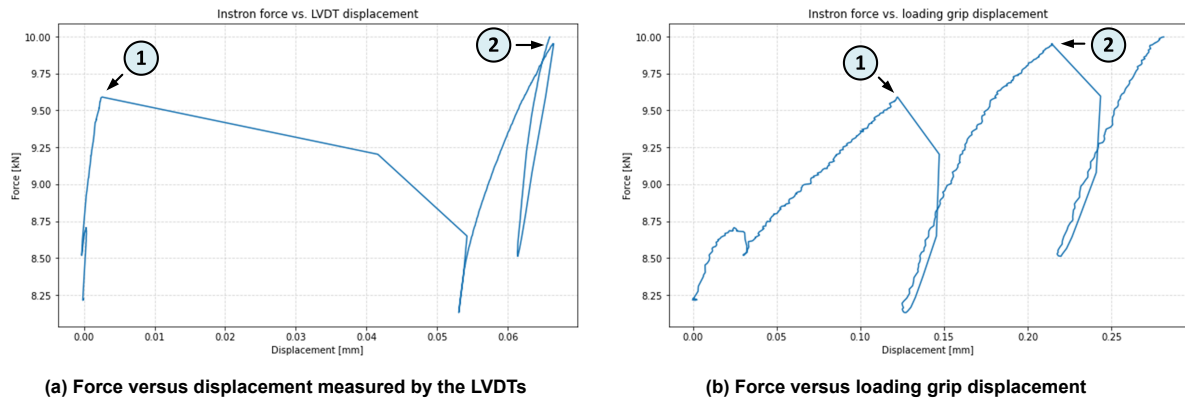

Figure 5.22: Force over time of the 10 kN mechanical test - Experiment 3

① See figure 5.24b for corresponding crack location

② See figure 5.24c for corresponding crack location

Figure 5.22 reveals the force development over time during the mechanical test, the force increases from 8.25 kN to 8.70 kN and then drops. A displacement is registered by the loading grips, but not by

the LVDTs, meaning that this crack occurred outside of the LVDT region (see figure 5.23). Next, the load increases again until F(t = 250) = 9.60 kN and then significantly drops to 8.15 kN. A displacement increase is detected by the LVDTs (see figure 5.23a), meaning that a through crack occurred between the LVDTs. This crack is indicated with an encircled '1' and its location is also indicated in the DIC analysis, see figure 5.24b. After another gradual load increase, the force drops again at F(t = 440) = 9.90 kN and marks the second through crack. Although a through crack is formed, it is not located between the LVDTs as figure 5.23a shows no increase in displacement measured by the LVDTs. Figure 5.24 confirms this, crack number 2 is located at the bottom of the exposed area but outside of the LVDT range. Finally, the load increases again and stops at 10 kN, which is the load capacity of the Instron. The total duration of the test equals 570 seconds. The load displacement curves of both the LVDTs and the loading grip are displayed in figure 5.23 below:

(a) Force versus displacement measured by the LVDTs   (b) Force versus loading grip displacement

Figure 5.23: Force versus displacement curves of the 10 kN tensile test - Experiment 3

① See figure 5.24b for corresponding crack location

② See figure 5.24c for corresponding crack location

Since the initial force of this tensile test was closer to the capacity of the Instron compared to the first two experiments, a displacement rate of 0.0005 mm per second was used (twice as slow compared to the first experiments). Figure 5.23a shows the first through crack at the location of the encircled '1'. The x-axis shows the displacement and the crack width is roughly 50 μm for the first crack. This increase in displacement is also visible in the loading grip load displacement graph. The second through crack causes a snapback from F = 9.90 kN to F = 8.50 kN as the displacement decreases in figure 5.23a. Conversely, the loading grip data shows an increase in displacement because the crack occurred outside of the LVDT range. The total displacement between the LVDTs equals 66 μm, while the total displacement between the loading grip and the bottom of the Instron equals 280 μm.

DIC analysis

For this mechanical tensile test, a frequency of 5 seconds per photo was chosen. The density of the speckle pattern is slightly less dense compared to the first experiment and more dense compared to the second experiment. Therefore, a facet size to point distance of respectively 40 pixels and 20 pixels proved to be the optimal ratio for good pattern quality over the area of interest. The strain in y-direction during the test according to the DIC analysis is shown in figure 5.24 below:
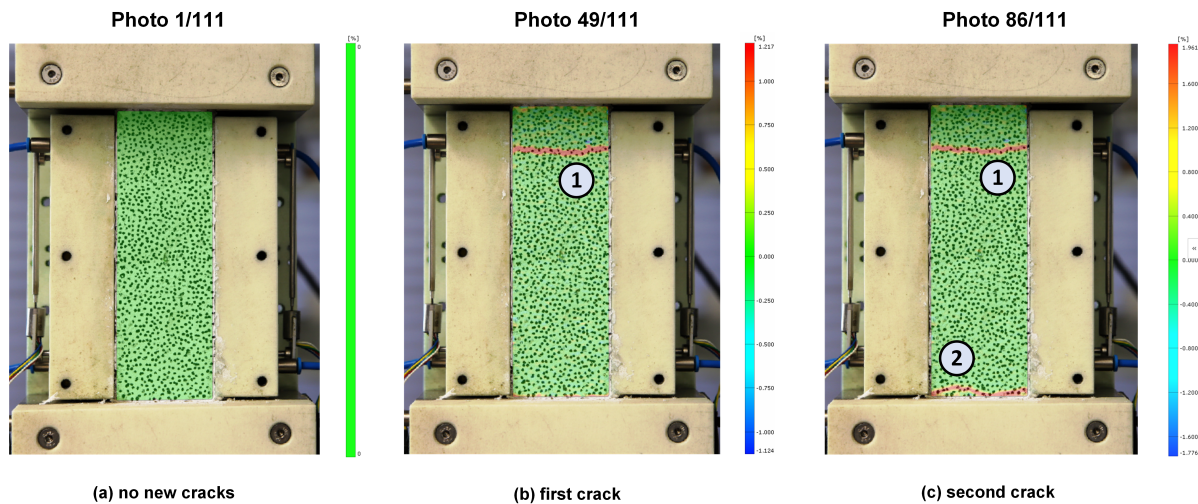
Photo 1/111   **Photo 49/111**   **Photo 86/111**

(a) no new cracks   (b) first crack   (c) second crack

Figure 5.24: Strain in y-direction as computed by the DIC software at different cracks.

Figure 5.24a shows the initial photo and the speckle pattern for the third and final experiment. The first crack shows up at photo 47 and is located in the upper region of the area of interest. The second and final crack becomes apparent from photo 86 and onwards and is located at the bottom of the area of interest. It is clear that the second crack occurred outside of the LVDT range, while the first crack formed just inside of the LVDTs. Both cracks are able to be quantified; the y-displacement graph at over the longitudinal length of the area of interest is shown in figure 5.25. This graph shows the displacement data at the final photo of the test, meaning at a force of 10 kN.
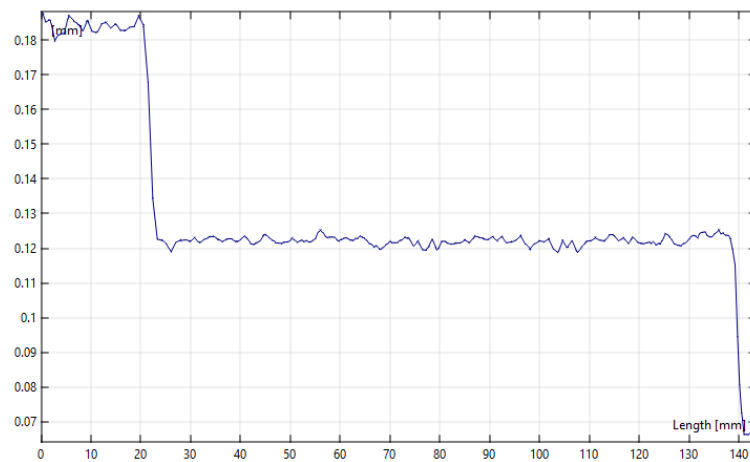
Figure 5.25: The deformation in y-direction at the final photo of the DIC analysis.

Figure 5.25 shows a jump between x = 20 and x = 22 mm corresponding with the crack on the top of the specimen. The jump between x = 138 mm and x = 140 mm corresponds with the crack at the bottom of the exposed area. The latter crack has a width of 0.058 mm, while the crack at the top of the specimen has a width of 0.064 mm. The evolution of both cracks during the final stages of the mechanical test are displayed in table 5.4 below:

Table 5.4: Crack width during the last stages of the tensile test (w_1 top crack, w_2 bottom crack)

Photo no.	w_1 [mm]	w_2 [mm]	w_{avg} [mm]
96	0.063	0.055	0.059
101	0.060	0.054	0.057
106	0.064	0.056	0.060
111	0.064	0.058	0.061

From table 5.4 it becomes clear that the first crack is slightly larger compared to the second crack. The maximum average crack width is observed in the final photo. Notably, the average crack width at photograph 96 surpasses that at photo 101.

Optical microscope analysis

Similarly to the first two experiments, the third experiment requires clarification regarding the crack locations. The results of the optical microscope analysis are presented in figure 5.26. In this specimen, the cracks were closed and not visible under the microscope, so they were reopened using the Instron.
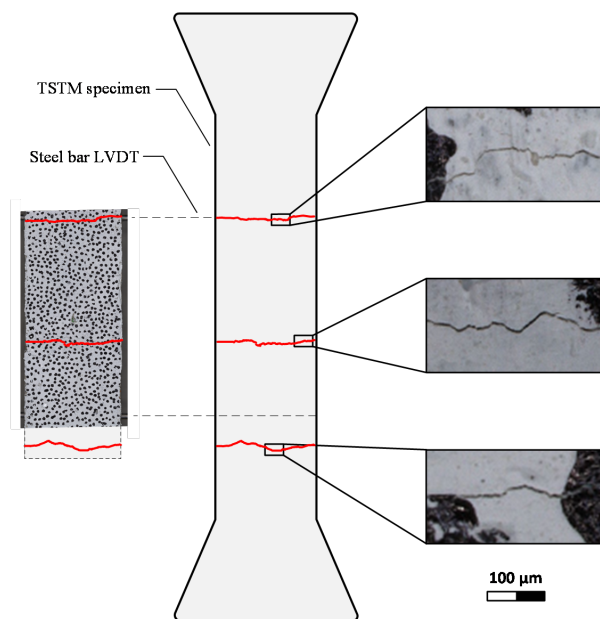
Figure 5.26: Stitched optical microscope image (left) including zoomed in images of cracks in the TSTM specimen (right)

Figure 5.26 shows that there are two cracks between the LVDT region, of which one is just on the border. The cracks on the top and bottom of the specimen are the same cracks which occurred during the DIC analysis as seen in figure 5.24. The bottom crack is outside of the LVDT region and just inside of the exposed speckle pattern.

The goal of the third experiment was to induce two cracks between the LVDTs due to restrained autogenous and thermal shrinkage. The crack located just below the middle of the specimen was not observed in the strain analysis from the DIC (figure 5.24). This absence suggests it might have occurred due to imposed deformation. However, the Instron data from the reopening of the cracks indicates otherwise. As shown in Figure C.5, there is a significant increase in displacement accompanied by a decrease in load, confirming that this displacement was indeed caused by a through crack in that region. Therefore, it is almost certain that the crack in the middle of figure 5.26 was induced during the reopening process.

Examining the spacing between the cracks in figure 5.26, it appears highly unlikely that additional through cracks exist in the exposed region where the speckle pattern is applied, especially considering

the transfer length of the threaded bar. Remarkably, two imposed deformation cracks were anticipated based on the long term test, yet the optical microscope analysis shows no visible imposed deformation cracks. Two possible explanations can account for this observation. First, the imposed deformation cracks may have healed, with the healing product being denser than the original mortar. As previously explained, this can lead to stress redistribution, potentially causing a new crack to form elsewhere rather than reopening the healed crack. However, the maturity of the specimen after the first mechanical test was relatively high (4445 °Ch), especially when compared to the first and second experiments. Therefore, it is not expected that a significant amount of unhydrated cement would be available to facilitate healing of the cracks afterwards.

The second explanation is that there are genuinely no imposed deformation through cracks present during the long-term test. The observed decreases in load and increases in displacement during this test may correspond to either microcracks or cracks located outside the exposed area of the mini-TSTM. Nonetheless, it remains valid that the fraction of stress due to imposed deformation relative to the stress from mechanical loading is greater compared to the first and second experiments.

5.3. Theoretical crack width

Three different experiments were performed, each loaded to the same final force but with a different fraction of load due to imposed deformation beforehand. Chapter 3 discussed five different design codes and guidelines which can be used to predict crack widths. NEN-EN 1992-1-1 states that stresses due to imposed deformation and mechanical loading should be summed to determine the crack width. Therefore, the final load of 10 kN may be used for calculating the predicted crack width and may then be compared to the measured crack widths. The same holds for Model Code 2010 which states the following:

"*Hence, where cracking is due to imposed deformations and loads, the steel stresses at the cracks due to loads as well as imposed deformations should be taken into account.*" (fib, 2013).

Van Breugel also states to combine stresses due to imposed deformation and mechanical loading and distinguishes crack widths during the crack propagation phase and cracks during the stabilized cracking stage.
However, NEN-EN 1992-3 and CIRIA C766 are not constructed for the combination of imposed deformation and mechanical loading. Annex M of NEN 1992-3 is used to calculate crack widths due to '*restraint of imposed deformations*' and should thus not be used for mechanical loads as well. CIRIA C766 states that it is not common practice to add restrained thermal and shrinkage deformations with structural loading. According to CIRIA C766, it does cause harm to the structural performance to not add the imposed deformation and structural loading (Bamforth, 2019). Imposed deformation is not regarded to cause reinforced concrete elements to reach the stabilized cracking stage ($\varepsilon > \varepsilon_{fdc}$) which is why NEN-EN 1992-3 and CIRIA C766 do not account for this stage.
For these reasons, NEN-EN 1992-3 and CIRIA C766 will not be included to compare the final cracks widths, but may be used to determine cracks occurring in the crack propagation stage. The results will be presented in twofold: the crack widths and predictions of the first new crack during the mechanical test and at the final stage (at 10 kN).

Two assumptions have been made in order to obtain the crack width values found in table 5.5 and table 5.7. The Eurocode expressions make use of $f_{ct,eff}$ which is the mean value of the tensile strength effective when the first cracks are expected. Usually, f_{ctm} should be used according to Eurocode, but since the cracking occurs before the mortar has reached 28 days, $f_{ctm}(t)$ has to be used. It is known that the first crack in a reinforced concrete element under pure tension happens at a lower strength than $f_{ctm}(t)$. The first assumption is the relation given in equation 3.22, which is $\sigma_{cr}(t) = 0.75 f_{ctm}(t)$. The second assumption has been made to estimate the elastic modulus of the mortar at the time of cracking. For this, the relations found in Eurocode have been used. The mean tensile strength is known using the first assumption, the characteristic compressive strength according to Eurocode follows from (CEN, 2005):

$$f_{ck} = \frac{f_{ctm}^{3/2}}{0.3}$$ (5.5)

The mean compressive strength is easily found when the characteristic compressive strength is known:

$$f_{cm} = f_{ck} + 8$$ (5.6)

The latter expression is then used to determine the elastic modulus, which is the second assumption made to calculate the theoretical crack widths.

$$E_{cm} = 22 * \left(\frac{f_{cm}}{10}\right)^{0.3}$$ (5.7)

Cracks during crack formation stage

Table 5.5 shows the measured crack widths and predictions of the first crack occurring during the DIC analysis. For Model Code 2010, it has been assumed that short term loading and the crack formation stage is applicable. The according parameters to determine the strain difference between concrete and steel can be found in figure 3.6.

Table 5.5: Measured and predicted crack widths using different structural codes and guidelines during the crack formation phase (presented values in mm).

Experiment no.	Measured	NEN-EN 1992-1-1	NEN-EN 1992-3	MC2010	CIRIA C766	Van Breugel
1	0.044	0.059	0.082	0.043	0.058	0.034
2	0.027	0.031	0.089	0.022	0.062	0.036
3	0.053	0.056	0.111	0.040	0.077	0.043

Experiment 1: zero imposed def. cracks

Experiment 2: one imposed def. crack

Experiment 3: two imposed def. cracks

These values do not immediately show the crack width differences and the magnitude of the differences. Hence, a bar plot is created in which the measured crack widths are displayed using a horizontal dotted line for each of the experiments. Figure 5.27 shows the measured crack width of the first crack occurring during the mechanical tests and the predictions of the five structural design codes and guidelines.
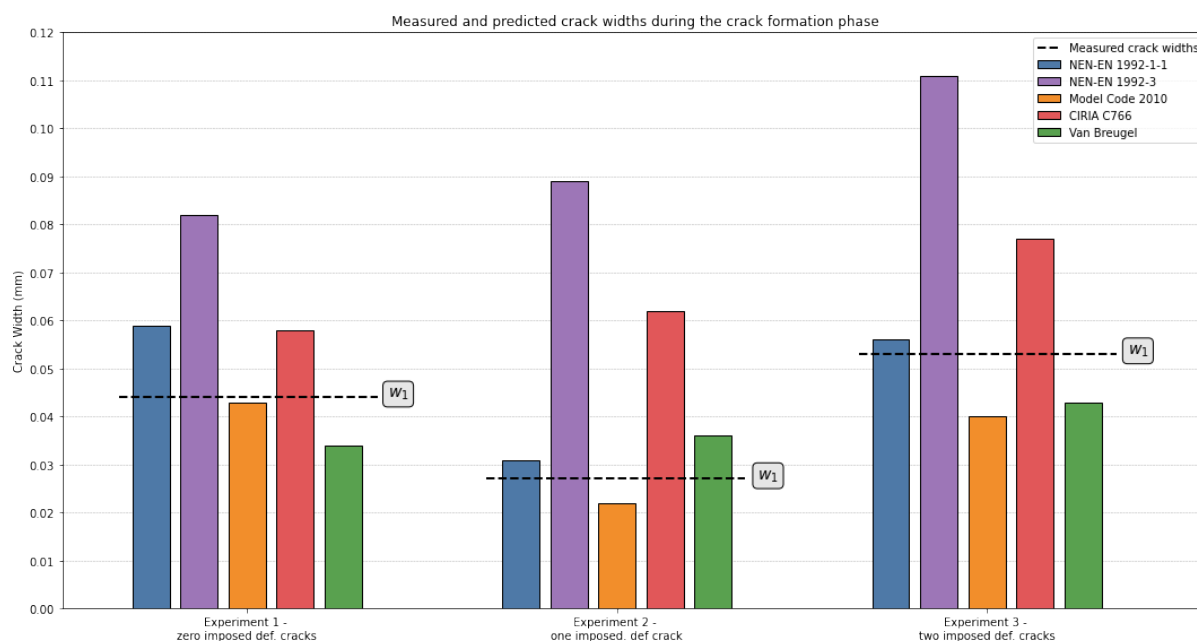
Measured and predicted crack widths during the crack formation phase

Figure 5.27: Measured and predicted crack widths using different structural codes and guidelines.

The third and final way of visualizing the results of comparing the measured and predicted crack widths is by expressing the differences compared to the measured crack widths in percentages. This has been done in 5.6, in which the measured crack widths are still expressed in mm, but the predicted crack widths are expressed in percentual differences compared to the measured crack widths.

Table 5.6: Predicted crack widths differences in percentages of the measured crack widths.

Experiment no.	Measured [mm]	NEN-EN 1992-1-1	NEN-EN 1992-3	MC2010	CIRIA C766	Van Breugel	Average
1	0.044	+34%	+86%	-2%	+32%	-23%	+25%
2	0.027	+15%	+230%	-19%	+130%	+33%	+78%
3	0.053	+6%	+109%	-25%	+45%	-19%	+23%
		+18%	+142%	-15%	+69%	-3%	

Experiment 1: zero imposed def. cracks

Experiment 2: one imposed def. crack

Experiment 3: two imposed def. cracks

Both table 5.5 and table 5.6, along with figure 5.27, provide key insights. The first notable observation is the relatively low measured crack width of the second experiment (0.027 mm). One might expect this value to fall between those of the first and third experiments (0.044 mm and 0.053 mm, respectively) or at least close to them. This discrepancy is also evident in table 5.6, where the second experiment shows a significantly higher average increase (+78%) compared to the first and third experiments (+25% and +23%).

Secondly, NEN-EN 1992-3 and CIRIA C766 appear to be the least accurate of the five predictions. NEN-EN 1992-3 exhibits inaccuracies across all three experiments, while CIRIA C766 provides relatively accurate predictions for the first and third experiments (+32% and +45%), yet is significantly off for the second experiment (+142%). It is surprising that these structural design codes, which are specifically designed to address cracking during the crack formation stage under imposed deformation, perform the worst out of all the codes and guidelines.

In contrast, Model Code 2010, NEN-EN 1992-1-1, and Van Breugel are the most accurate and consistent for the crack formation stage. Van Breugel shows the highest accuracy with an average deviation of

just -3%, though it falls short in terms of absolute differences. Model Code 2010 and NEN-EN 1992-1-1 are more consistent in this regard. MC2010 tends to underestimate crack widths, while NEN 1992-1-1 consistently overestimates them.

Model Code 2010 stands out as the most consistent and accurate of the five codes and guidelines. However, considering the primary goal of structural design codes and guidelines, which is to offer standardized procedures for design, NEN 1992-1-1 is the most suitable. It consistently and accurately predicted crack widths during the crack formation stage and never underestimated them.

Cracks at the end of the mechanical test

The crack widths at the end of the mechanical test, at a load of 10 kN, are displayed in table 5.7. It should be noted that for experiment 2 and 3, two cracks were measured and this has been included in the table. The stabilized cracking stage is assumed for the predictions of Model Code 2010, along with short term loading as the mechanical test is regarded as such. NEN-EN 1992-3 and CIRIA C766 are excluded as they do not regard cracks widths in the stabilized cracking stage.

Table 5.7: Measured and predicted crack widths using different structural codes and guidelines at 10 kN during the mechanical test (presented values in mm).

Experiment no.	Measured 1	Measured 2	NEN-EN 1992-1-1	MC2010	Van Breugel
1	0.072	-	0.098	0.095	0.066
2	0.065	0.061	0.090	0.091	0.063
3	0.064	0.058	0.064	0.079	0.052

Experiment 1: zero imposed def. cracks

Experiment 2: one imposed def. crack

Experiment 3: two imposed def. cracks

The data found in table 5.7 above is again visualized using a bar plot to easily interpret them. The dotted lines for the measurements are indicated with w_1 and w_2 and correspond with the labelled cracks in the DIC analyses (see figure 5.10, 5.17 and 5.24).
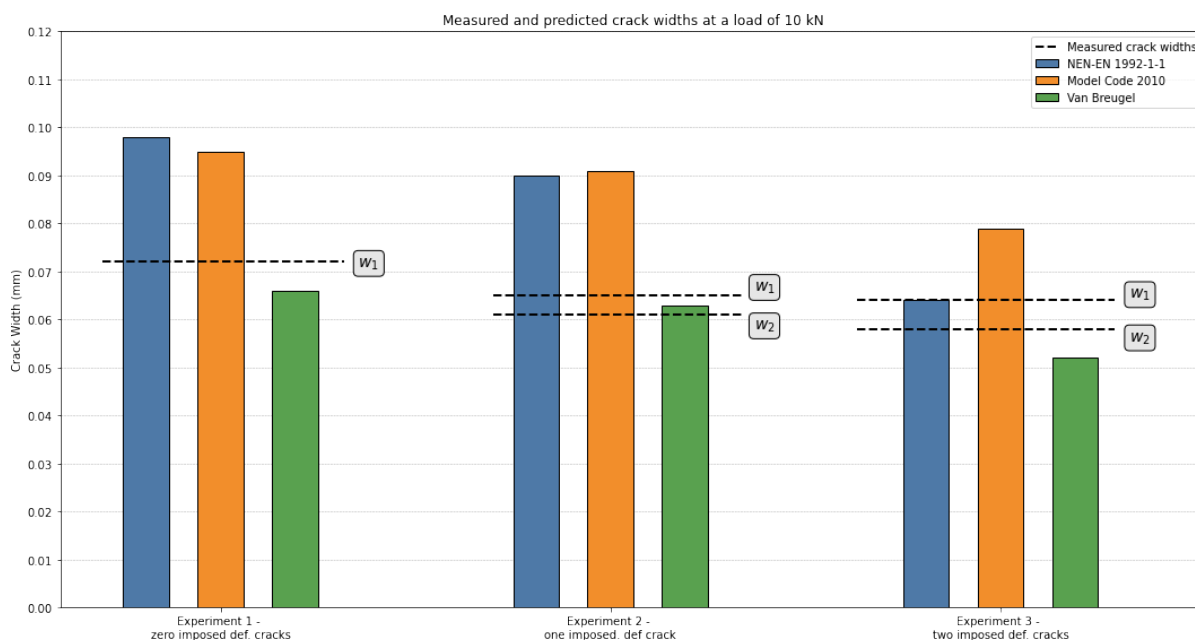

Figure 5.28: Measured and predicted crack widths using different structural codes and guidelines.

The differences between the measured and predicted crack widths will again be expressed in percentages relative to the measured crack widths. Since the second and third experiment each have two

separate measured crack widths, the differences will be compared to the average of these two measurements. Table 5.7 shows the percentual differences including an average per experiment and the average per structural design code or guideline.

Table 5.8: Predicted crack widths differences in percentages of the measured crack widths (percentages based on average crack width).

Experiment no.	Measured 1 [mm]	Measured 2 [mm]	NEN-EN 1992-1-1	MC2010	Van Breugel	Average
1	0.072	-	+36%	+32%	-8%	+20%
2	0.065	0.061	+43%	+44%	0%	+29%
3	0.064	0.058	+5%	+30%	-15%	+7%
			+28%	+35%	-8%	

Experiment 1: zero imposed def. cracks

Experiment 2: one imposed def. crack

Experiment 3: two imposed def. cracks

Tables 5.7, 5.8, and figure 5.28 provide valuable insights. Starting with Van Breugel, this structural guideline is the most accurate and consistent across the three experiments. It slightly underestimates the first and third experiments by 8% and 15%, respectively, and even perfectly predicts the second experiment when considering the average crack width. Overall, Van Breugel can be regarded as accurate and consistent, although slightly conservative in its predictions for two experiments.
Looking more generally at the final stage of the mechanical test, the crack widths are predicted with greater accuracy, with the worst prediction overestimating the width by 44%. This is considerably more precise compared to predictions during the crack formation stage, where the worst estimate was 230% off. This improvement in prediction accuracy at the mechanical test stage highlights the consistency of structural design codes at this phase.

Model Code 2010 predicted the crack widths the worst at the 10 kN stage, overestimating them by at least 30% for each experiment. This suggests that Model Code 2010 is conservative when predicting crack widths resulting from the combination of imposed deformation and mechanical loading. Interestingly, during the crack formation stage, Model Code 2010 consistently underestimated crack widths (table 5.6). This trend indicates that, while the code is conservative under mechanical loading, it is potentially unsafe when applied to the crack formation stage, as it may underestimate critical crack widths.
NEN-EN 1992-1-1 overestimated the crack widths for the first and second experiments by 36% and 43%, respectively, but was much more accurate in the third experiment (+5%). This suggests that NEN-EN 1992-1-1 may become more precise when the proportion of stress due to imposed deformation increases or when dealing with cementitious materials at higher maturities. When comparing the predictions for the crack formation stage to those at 10 kN, NEN-EN 1992-1-1 provided better predictions during the crack formation stage (+18% on average compared to +28% at 10 kN).
Tables 5.6 and 5.8 highlight Van Breugel's accuracy in both phases of the mechanical test. Van Breugel remained consistent at the 10 kN load stage and, although slightly less consistent during the crack formation stage (-23%, +33%, and -19%), it remains a reliable guideline.

The final and perhaps most interesting observation from the data is the decreasing trend in measured crack widths across the three experiments (0.072 mm, 0.063 mm, and 0.061 mm, respectively). There are two key factors that likely explain this trend. The first and most apparent reason is the variation in weighted maturity across the experiments—2175 °Ch, 4036 °Ch, and 4445 °Ch, respectively. Increased weighted maturity is linked to increased mortar stiffness, which results in less deformation under the same load, thereby limiting crack widths. Additionally, the bond stress between the steel reinforcing bars and concrete increases as the concrete compressive strength increases, as noted by Song et al. (2015). With higher weighted maturity, the mortar specimens better control crack widths.
The second potential explanation is the increasing proportion of stress due to imposed deformation relative to mechanical loading. The load due to imposed deformation before the mechanical test was

3.5 kN, 6.6 kN, and 8.7 kN, respectively, for the three experiments. All three specimens were then mechanically loaded to 10 kN, but the increasing amount of imposed deformation stress may explain the trend of decreasing crack widths.

6
Conclusion

This research primarily consists of two parts: the development of the experimental setup for a reinforced mini-TSTM experiment and the investigation of cracking behavior resulting from a combination of imposed deformation and mechanical loading. The conclusions drawn from this twofold study will be presented in this chapter.

6.1. General mortar properties

The autogenous shrinkage was deemed negligible initially. The utilized mortar mix design has a water to cement ratio of 0.50, which theoretically shows a lesser amount of autogenous shrinkage compared to lower water to cement ratios. Figure 5.5 shows the total deformation of the ADTM specimen and separated into thermal and autogenous deformation. It is clear that the autogenous shrinkage is definitely not negligible and even caused tensile stress being applied by the Instron during the heating phase of the experiment.

Liang (2024) developed the mini-TSTM, which is a scaled down version of the TSTM. The mini-TSTM can be operated by a single person and required a significantly lower working force to be executed. He found that the mini-TSTM is still accurate compared to the regular TSTM, with the downside being that coarse aggregate does not fit in the relatively small mold. In this research, different mix designs were tested to investigate autogenous shrinkage. The regular TSTM has been fitted with reinforcement, but the mini-TSTM had not yet been fitted with reinforcement. Chapter 4 discusses the development of this experimental setup, resulting in a fully functional experiment that produces useful data for future research applications.

Liang (2024) investigated the autogenous shrinkage behavior of a certain mortar mix design. He identifies four distinct phases, which are also evident in figure 5.5. However, the autogenous shrinkage exhibits considerable variability across the three experiments, and literature continues to explore methods for mitigating the uncertainty in quantifying autogenous shrinkage.

The temperature regime has been constructed assuming no autogenous shrinkage and using a conservative value for the CTE. A temperature differential of 46.7 °C was determined in order for the thermal shrinkage to cause the fully developed crack pattern to be reached. Because of the significant autogenous shrinkage and the CTE to be higher than assumed, a significantly lower temperature differential could be adopted. When two cracks occurred in the third experiment, the temperature differential was only 13.01 °C.

The tensile strength development of the mortar mix design is constructed by determining the weighted maturity of two specimens at a certain age and the stress at which the mortar cracked. Figure 5.3 shows the calibration lines for the ADTM and TSTM specimens. The results indicate that the tensile strength measured in the TSTM is higher than in the ADTM, even though both have the same weighted maturity. This difference is likely due to the first cracks consistently forming at the transitions between the dovetails and the straight part of the specimens, where stress concentrations occur. In the ADTM

specimens, these initial cracks are considered, while for the TSTM specimens, only the cracks occurring between the LVDTs are taken into account.
The calibration line for the ADTM is quite accurate with an R-value of 0.916 and the TSTM calibration is somewhat less accurate with an R-value of 0.725.

The coefficient of thermal expansion (CTE) of the mortar mix was determined by analyzing the temperature and displacement differential of the ADTM during the final three hours of two separate experiments, yielding a value of $1.2050 \cdot 10^{-5} \ °C^{-1}$. For ordinary concrete, NEN-EN 1992-1-1 suggests a standard value of $1 \cdot 10^{-5} \ °C^{-1}$. In comparison, Jeong et al. (2012) reported a higher value of $1.45 \cdot 10^{-5} \ °C^{-1}$ for mortar made with CEM I cement. The mortar mix in this research used CEM III/B, and the obtained value appears reasonable in light of this.

6.2. Experimental results

The mini-TSTM was chosen for the experimental work in order to answer the main research question. The results of chapter 5: '*Experimental results*' have lead to a sufficient amount of data to answer this main research question. The first research question, which is used to answer the main research question, outlined in chapter 1 is as follows:

> *How do the crack width predictions of structural design codes and guidelines compare to experimentally observed crack widths due to the combination of imposed deformation and mechanical loading?*

CIRIA C766 and particularly NEN 1992-3 are both inconsistent and inaccurate in predicting crack width during the crack formation stage. This is rather remarkable as they are designed specifically for imposed deformation, most often causing reinforced concrete to enter and remain in the crack formation stage. The strain difference between concrete and steel is determined based on force equilibrium between steel reinforcement and concrete according to NEN 1992-3 and CIRIA C766. However, the findings in this research suggest that relying on force equilibrium is inadequate for predicting crack widths, especially when compared to the underlying theories used by other structural codes and guidelines.
Model Code 2010, on the other hand, uses the tensile member theory and acknowledges that, unlike the theoretical model, the load during the crack formation stage is not constant. It distinguishes between crack widths during the crack formation stage, the stabilized cracking stage, and even accounts for differences between short-term and long-term loading. Among all the structural codes analyzed, Model Code 2010 is the most consistent and accurate for predicting crack widths during the crack formation stage, as reflected in its minimal absolute differences compared to the measured data (see table 5.6).
NEN-EN 1992-1-1 is also considerably consistent and accurate for the crack formation stage. It is also based on force equilibrium, but does take into account the actual steel stress for each crack. This significantly increases its accuracy compared to NEN 1992-3 and CIRIA C766.
Van Breugel may initially seem like the most accurate structural design code or guideline, as shown in table 5.6. However, while it overestimated the crack width in the second experiment, it underestimated the crack widths in the first and third experiments. Therefore, its absolute accuracy relative to the experimental measurements is less precise than it might appear at first glance.
It should be noted that the measured crack width during the crack formation stage of experiment 2 appears unexpectedly low. Given its weighted maturity and load at cracking, one would anticipate a crack width of 0.027 mm to fall between the first and third experiments (0.044 mm and 0.053 mm, respectively), or at least be closer to those values.

After the crack formation stage, the crack widths were recorded at the end of the mechanical test, with a load of 10 kN. Van Breugel's predictions for this stage were notably accurate and consistent. As shown in Table 5.8, the absolute difference in Van Breugel's predictions averaged just 8%.
In contrast, the predictions of Model Code 2010 were less accurate at this stage compared to the crack formation stage, showing averages of -15% and +35%, respectively. Model Code 2010 consistently underestimated crack widths during the crack formation stage, while overestimating them at the 10 kN

load.

NEN-EN 1992-1-1, while still relatively accurate, was slightly less so for crack widths at 10 kN compared to the crack formation stage, with average differences of +28% and +18%.

To directly answer this specific research question, the design codes and guidelines predict the crack widths, due to the combination of imposed deformation and mechanical loading, with decent accuracy when NEN-EN 1992-3 and CIRIA C766 are disregarded. It can be concluded that crack widths due the combination of loading purely based on force equilibrium during the crack formation stage, is not adequate. The other three structural design codes and guidelines either consider the actual steel stress at each crack, and/or distinguish cracking during the crack formation stage and stabilized cracking stage. While Model Code 2010 is the most consistent for the crack formation stage, it should be used cautiously due to its tendency to underestimate. Based on the experimental data, Van Breugel stands out as the most consistent and accurate for predicting crack widths under the combined effects of imposed deformation and mechanical loading.

> *How does an increase in the fraction of imposed deformation relative to mechanical loading affect crack width in reinforced concrete?*

To answer this research question, it is inadequate to analyze the crack widths during the crack formation stage. The reason for this, is that there is hardly any mechanical loading for experiment 2 and 3. The measured crack widths at the end of the mechanical test, with a load of 10 kN, can be directly used to formulate an answer to this research question. The amount of load due to imposed deformation before the mechanical test was conducted equals 3.5 kN, 6.6 kN, and 8.7 kN for experiment 1, 2 and 3 respectively. The corresponding measured crack widths, shown in table 5.7, were 0.072 mm, 0.063 mm, and 0.061 mm, with the latter two values representing the average of the two cracks recorded in the DIC analysis. Based on the amount of imposed deformation and according final crack widths, it could be said that an increase in the fraction of imposed deformation relative to mechanical loading will decrease the final crack width in reinforced concrete.

However, as mentioned in chapter 5: the weighted maturity for the individual experiments were not equal. For experiment 1, 2 and 3, the respective weighted maturities equal 2175 °Ch, 4036 °Ch, and 4445 °Ch. Both the stiffness and bond stress between the steel reinforcement and mortar are increase for increasing weighted maturities. An increased stiffness results in less deformation for a specific load compared to lower stiffnesses. A higher bond stress results in a lower transfer length. Both a decreased deformation and decreased transfer length will reduce the final crack width. Consequently, it cannot be confidently concluded that an increase in the fraction of imposed deformation relative to mechanical loading will consistently decrease the final crack width in reinforced concrete.

> *How do crack widths develop in reinforced concrete under the combination of imposed deformation and mechanical loading?*

This main research question will be answered based on the conclusions found in the two research questions discussed in this chapter. Crack widths under the combination of imposed deformation and mechanical loading were best predicted by Model Code 2010 during the crack formation stage. Model Code 2010's crack width theory is based on the tensile member diagram and includes the actual steel stress in all its stages. It has been concluded that NEN-EN 1992-3 and CIRIA C766 are inadequate for the crack formation stage, as the force equilibrium theorem does not align with the experimentally observed crack width values.

The crack widths at 10 kN of load, both due to imposed deformation and mechanical loading, were best predicted by Van Breugel. Van Breugel makes a clear division for calculating crack widths during the crack formation stage and for the stabilized cracking stage. This means that Van Breugel effectively captures the behaviour of concrete under the combination of imposed deformation and mechanical loading during the stabilized cracking stage.

EN-EN 1992-1-1 is the most commonly used structural design code for designing reinforced concrete structures in Europe and consistently overestimated the crack widths at both stages of the experiments. While the overestimation was not extreme, with a maximum of +43% and an average of +18% for the crack formation stage, and an average of +28% at a load of 10 kN, this persistent overestimation indicates a conservative approach. This conservatism may result in the specification of excessive reinforcement in concrete structures under combined imposed deformation and mechanical loading. Based on the findings of this research, CIRIA C766 and particularly NEN-EN 1992-3 should be avoided when predicting expected crack widths due to imposed deformations. Although these guidelines are specifically designed for imposed deformation, their exclusion of the actual steel stress appears to be detrimental to the accuracy of their crack width predictions.

Based on this research, it is advised to use Model Code 2010 to predict crack widths due to combined imposed deformation and mechanical loading for the crack formation stage and Van Breugel for the stabilized cracking stage. It is important to note that both structural design guidelines tend to slightly underestimate crack widths, which should be taken into account during the design process. The most crucial takeaway is that one must understand the underlying principles and theories of the individual design codes and guidelines. Based on this understanding, the most appropriate one should be selected depending on the specific circumstances.

The data in table 5.8 suggest that an increase in the fraction of imposed deformation relative to mechanical loading tends to reduce the final crack width in reinforced concrete. However, due to varying weighted maturities across the experiments, this cannot be confirmed with certainty. It is recommended to avoid restraining reinforced concrete structures during their early age as much as possible, since thermal, drying, and autogenous shrinkage may lead to cracking. Crack widths at lower maturities will likely be larger than those at higher maturities and should therefore be minimized.

7

Discussion

The reinforcement layout was designed to encourage the formation of three cracks between the LVDTs. However, it was observed that only in the first experiment were these three cracks clearly visible in the DIC analysis. Even in this case, one of the crack widths could not be quantified as it was located near the border of the area of interest. Increasing the number of visible cracks would reduce the uncertainty in the average crack width, thereby improving the accuracy of the results. This could be achieved in two ways: by adjusting the reinforcement layout to reduce the spacing between cracks, or by exposing more of the dogbone area to ensure that all cracks are captured in the DIC analysis.

In this study, threaded bars were used as reinforcement for the mortar specimens, deviating from the conventional use of regular reinforcing bars that typically possess higher yield and ultimate strengths. The decision to use threaded bars required validation of their bond strength with the mortar. To assess this, a tensile test was conducted on a reinforced specimen, resulting in the formation of three distinct cracks. This cracking pattern suggests that the threaded bar achieved good bond strength with the mortar, as the stress transfer was sufficient to induce cracking. However, it is important to note that while this tensile test provides initial validation, a pull-out test would offer a more direct and rigorous evaluation of the bond strength. A pull-out test specifically measures the force required to extract the bar from the mortar, providing a more precise assessment of the bond performance between the reinforcement and the surrounding cementitious material.

The DIC speckle pattern was created by first painting the surface of the mortar white, drying it with a heat gun, and then applying black dots using a black permanent marker. The accuracy of the DIC analysis could be improved by using smaller dots, for example, by using a spray can. This would allow for a reduction in facet size and point distance, resulting in a larger area for investigation and enhanced accuracy. However, precautions must be taken to prevent the mini-TSTM equipment, such as the mold, cryostat, and loading machine, from becoming stained with paint.

To establish a correlation between the age of the mortar and the development of strength and elastic modulus across different experiments, the weighted maturity method was employed. This method accounts for the type of cement used but does not consider activation energy. Although the Arrhenius method, which accounts for both factors, would provide greater accuracy, it necessitates an adiabatic test of the mortar mixture. Given that the primary focus of this research is on structural aspects rather than material properties, the Dutch weighted maturity method is considered sufficiently accurate for the intended analysis.

The same conclusion applies to the determination of the CTE in this research. A small interval at the end of two experiments was selected to minimize the influence of autogenous shrinkage before determining the CTE. A more accurate method for determining the CTE is described by Liang (2024), which involves applying a temperature cycle over a short period to more effectively exclude the influence of autogenous shrinkage. However, for the purposes of this research, the approach used to determine the CTE is deemed sufficiently accurate.

In this study, structural design codes and guidelines developed for concrete were employed to determine the crack width of mortar specimens. While these codes provide well-established methodologies for assessing crack behavior, it is important to recognize that they are specifically designed for con-

crete, which has different material properties and behavior compared to mortar. The application of these guidelines to mortar, therefore, introduces certain assumptions and potential limitations. For instance, differences in material composition, mechanical properties, and cracking behavior between mortar and concrete may affect the accuracy and relevance of the predicted crack widths. Nevertheless, given the absence of specific codes for mortar, using these established guidelines for concrete provides a reasonable and systematic approach to crack width estimation, though the results should be interpreted with caution.

The optical microscope analysis identified both the cracks formed due to imposed deformation and those resulting from mechanical loading. As expected, no cracks were observed due to imposed deformation in the first experiment, and one crack formed during the mechanical test. However, when the cracks were reopened for the microscope analysis, two additional through cracks were observed within the LVDT region. It remains unclear how these two additional cracks occurred at a lower load level and a higher weighted maturity compared to the initial mechanical test.

In the calculation of crack widths at a load of 10 kN, it was assumed that the specimen had reached the stabilized cracking stage, implying that no new cracks could form. However, the reopening of the specimen indicates that new cracks could still occur, suggesting that the specimen was still in the crack formation stage rather than the stabilized cracking stage. This finding raises questions about the transition between these stages and the implications for crack width predictions under combined imposed deformation and mechanical loading.

The final and most significant discussion point pertains to the limited number of experiments conducted. Due to the time required to develop the experimental setup, fewer experiments were completed, which affects the robustness of the hypothesis validation. The hypothesis is that an increase in the fraction of imposed deformation relative to mechanical loading will decrease the final crack width in reinforced concrete. This hypothesis cannot be accepted based on the current results, but the uncertainty in the results of just three experiments is significant, performing more experiments could reduce this uncertainty whereby the hypothesis can be declined, or accepted with more confidence.

8
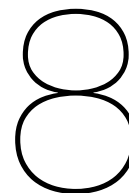
Recommendations

The first part of this research involved developing an experimental setup for the reinforced mini-TSTM. Key findings include the necessity of using threaded bars instead of regular reinforcing bars, as the latter are unsuitable for this setup. Additionally, it was determined that the reinforcing bars should be securely fixed to the end of the dovetail to prevent the dovetail from being pulled away from the reinforcing bars. The results obtained are promising, demonstrating that reliable and meaningful data can be derived from these experiments, which bodes well for future research.

The main research opportunity lies within further investigating the effect of an increase in the fraction of imposed deformation relative to mechanical loading on crack width in reinforced concrete. Due to varying weighted maturities in experiments 1, 2, and 3, the observed crack widths cannot be directly attributed to the level of imposed deformation stress. Performing the same experiments, but at the same weighted maturity would allow to confidently accept or reject the hypothesis. This can be achieved by designing the temperature profile of each experiment such that the desired amount of imposed deformation is achieved at the same weighted maturity. This will likely require optimization, as autogenous deformation is inherently unpredictable.

Ideally, if the hypothesis is accepted, a reduction factor for imposed deformation stresses could be developed. Integrating such a reduction factor into structural design codes and guidelines would lower the amount of reinforcement required to control cracks due to combined imposed deformation and mechanical loading. This advancement would represent a significant achievement in understanding imposed deformation in construction practice. By reducing the necessary amount of steel to control crack widths, designs for reinforced concrete structures would become more sustainable and cost-effective.

As discussed in section 2.2, reinforcement affects the shrinkage of concrete members. Bond stresses between reinforcing bars and concrete restrain part of the concrete's shrinkage, creating compressive stresses in the reinforcement and tensile stresses in the concrete. While this effect was not explored in this research, future studies could investigate the differences in shrinkage between reinforced and plain concrete elements. Additionally, there are significant research opportunities in examining the effects of novel reinforcing bars and cementitious materials on structural behavior and early-age properties, such as autogenous deformation.

Bibliography

Angst, M., U. Zintel, & Gehlen, C. (2019). Durable concrete structures: Cracks & corrosion and corrosion & cracks. *Proceedings of the 10th International Conference on Fracture Mechanics of Concrete and Concrete Structures*. https://doi.org/10.21012/fc10.233307

Bamforth, P. B. (2019). *CIRIA C766 - Control of cracking caused by restrained deformation in concrete*. CIRIA. https://www.ciria.org/ItemDetail?iProductCode=C766D&Category=DOWNLOAD&WebsiteKey=3f18c87a-d62b-4eca-8ef4-9b09309c1c91

Bazant, Z. P. (1972). Prediction of concrete creep effects using age-adjusted effective modulus method. *ACI Journal Proceedings*, *69*(4). https://doi.org/10.14359/11265

Bentz, D. P., Garboczi, E. J., Haecker, C. J., & Jensen, O. M. (1999). Effects of cement particle size distribution on performance properties of portland cement-based materials. *Cement and Concrete Research*, *29*(10), 1663–1671. https://doi.org/10.1016/S0008-8846(99)00163-5

Borsje, H., & Prins, P. (2002). Gewogen en geschikt bevonden. *Cement*.

CEN. (2005). *EN 1992-1-1 Eurocode 2: Design of concrete structures - Part 1-1: General rules and rules for buildings*.

Chang, Y., Qin, S., Huang, M., Hu, D., Yang, H., & Li, S. (2021). Analytical model of the bond stress-slip relationship for reinforced concrete due to splitting failure. *Construction and Building Materials*, *287*, 123025. https://doi.org/https://doi.org/10.1016/j.conbuildmat.2021.123025

Cornelissen, I. (2022). Experimental and numerical research into cracking behavior in a reinforced concrete beam subjected to a restrained imposed curvature. https://research.tue.nl/en/studentTheses/experimental-and-numerical-research-into-cracking-behavior-in-a-r

Edvardsen, C. K. (1996). Wasserdurchlässigkeit und Selbstheilung von Trennrissen in Beton. *Deutscher ausschuss für stahlbeton*, (455).

EN. (2016). *EN 196-1: Methods of testing cement – part 1: Determination of strength*.

ENCI. (2020, March). Hoogovencement CEM III/B 42,5 N-LH/SR [Technical specifications and characteristics of high furnace cement].

European Council. (2024). *Climate change: what the EU is doing*. https://www.consilium.europa.eu/en/policies/climate-change/ (Accessed on 01-03-2024).

fib. (2013). *Fib model code for concrete structures 2010* [500 p. ; 30 cm.]. Ernst, Wilhelm & Sohn. https://tudelft.on.worldcat.org/oclc/863694325

François, R., & Arliguie, G. (1999). Effect of microcracking and cracking on the development of corrosion in reinforced concrete members. *Magazine of Concrete Research*, *51*(2), 143–150. https://doi.org/10.1680/macr.1999.51.2.143

Gilbert, R. I., & Ranzi, G. (2010). Time-dependent behaviour of concrete structures. https://api.semanticscholar.org/CorpusID:136685360

Gribniak, V., Kaklauskas, G., & Bacinskas, D. (2008). Shrinkage in reinforced concrete structures: A computational aspect. *Journal of Civil Engineering and Management*, *14*(1), 49–60. https://doi.org/10.3846/1392-3730.2008.14.49-60

Gribniak, V., Kaklauskas, G., Kliukas, R., & Jakubovskis, R. (2013). Shrinkage effect on short-term deformation behavior of reinforced concrete – when it should not be neglected. *Materials and Design*, *51*, 1060–1070. https://doi.org/10.1016/j.matdes.2013.05.028

Jeong, J.-H., Zollinger, D., Lim, J.-S., & Park, J.-Y. (2012). Age and moisture effects on thermal expansion of concrete pavement slabs. *Journal of Materials in Civil Engineering*, *24*, 8–15. https://doi.org/10.1061/(ASCE)MT.1943-5533.0000342

Liang, M. (2024). *Stress evolution in early-age cementitious materials considering autogenous deformation and creep: New experimental and modelling techniques* [Dissertation]. Delft University of Technology. https://doi.org/10.4233/uuid:270173e7-6ce6-4a71-ac42-79eab09cce5f

Liang, M., Liu, C., Liang, X., Chang, Z., Schlangen, E., & Šavija, B. (2024). Effects of temperature on autogenous deformation and early-age stress evolution in cement pastes with low water to cement ratio. *Construction and Building Materials*, *411*, 134752. https://doi.org/https://doi.org/10.1016/j.conbuildmat.2023.134752

Liang, M., Luzio, G. D., Schlangen, E., & Šavija, B. (2024). Experimentally informed modeling of the early-age stress evolution in cementitious materials using exponential conversion from creep to relaxation. *Computer-Aided Civil and Infrastructure Engineering*. https://doi.org/10.1111/mice.13156

Liang, M., Ze, C., Yu, Z., Hao, C., Shan, H., Erik, S., & Branko, Š. (2023). Autogenous deformation induced-stress evolution in high-volume ggbfs concrete: Macro-scale behavior and micro-scale origin. *Construction and Building Materials*, *370*, 130663. https://doi.org/10.1016/j.conbuildmat.2023.130663

Liu, L., Ouyang, J., Li, F., Xin, J., Huang, D., & Gao, S. (2018). Research on the crack risk of early-age concrete under the temperature stress test machine. *Materials*, *11*(10). https://doi.org/10.3390/ma11101822

Lura, P. (2003, April). *Autogenous deformation and internal curing of concrete*. https://www.researchgate.net/publication/27347573_Autogenous_Deformation_and_Internal_Curing_of_Concrete

MKT. (2015, November). *Bond strength of threaded bars in cracked and uncracked concrete C20/25 - C50/60 (EN 206)* (tech. rep.) (Published by MKT, Germany. Provides mechanical properties for threaded bars in concrete.). MKT.

Moon, H., Ramanathan, S., Suraneni, P., Shon, C.-S., Lee, C.-J., & Chung, C.-W. (2018). Revisiting the effect of slag in reducing heat of hydration in concrete in comparison to other supplementary cementitious materials. *Materials*, *11*(10). https://doi.org/10.3390/ma11101847

NEN. (2011a). NEN-EN 197-1:2011 en: Cement – part 1: Composition, specifications and conformity criteria for common cements [NEN-EN 197-1:2011]. *European Committee for Standardization*.

NEN. (2011b). NEN-EN 1992-3:2006/NB:2011 Eurocode 2: Design of concrete structures – Part 3: Liquid retaining and containment structures [National Annex]. https://connect.nen.nl/standard/Detail/160908?compId=10037&collectionId=0

NEN. (2013). *Mechanical properties of fasteners made of carbon steel and alloy steel - part 1: Bolts, screws and studs with specified property classes - coarse thread and fine pitch thread* [(ISO 898-1:2013, IDT)].

NEN. (2020). *Nationale bijlage bij NEN-EN 1992-1-1+C2 Eurocode 2: Ontwerp en berekening van betonconstructies - Deel 1-1: Algemene regels en regels voor gebouwen*. CEN. https://connect.nen.nl/Standard/Detail/3625916?compId=10037&collectionId=0

Polder, R., Nijland, T., de Rooij, M., Larsen, C., & Pedersen, B. (2014). Innovation based on tradition: Blast furnace slag cement for durable concrete structures in norway? [1st concrete innovation conference, CIC2014, Oslo, Norway ; Conference date: 11-06-2014 Through 13-06-2014]. In H. Justnes (Ed.), *Proceedings of the 1st concrete innovation conference, cic2014* (pp. 1–7). COIN.

Reinhardt, H.-W. (2014). Aspects of imposed deformation in concrete structures – a condensed overview. *Structural Concrete*, *15*(4), 454–460. https://doi.org/10.1002/suco.201400014

Sarker, P. K., & McKenzie, L. G. (2009). Strength and hydration heat of concrete using fly ash as a partial replacement of cement. https://api.semanticscholar.org/CorpusID:55529569

Schiessl, P., & Raupach, M. (1997). Laboratory studies and calculations on the influence of crack width on chloride-induced corrosion of steel in concrete. *ACI Materials Journal*, *94*(1), 1–1. https://doi.org/10.14359/285

Song, X., Wu, Y., Gu, X., & Chen, C. (2015). Bond behaviour of reinforcing steel bars in early age concrete. *Construction and Building Materials*, *94*, 209–217. https://doi.org/https://doi.org/10.1016/j.conbuildmat.2015.06.060

Soutsos, M., Kanavaris, F., & Hatzitheodorou, A. (2018). Critical analysis of strength estimates from maturity functions. *Case Studies in Construction Materials*, *9*, e00183. https://doi.org/https://doi.org/10.1016/j.cscm.2018.e00183

Springenschmid, R., Breitenbücher, R., & Mangold, M. (1994). Development of the cracking frame and the temperature-stress testing machine. *Proceedings of the International RILEM Symposium*, 137–144.

Sule, M. (2003). Effect of reinforcement on early-age cracking in high strength concrete. *TU Delft Repositories*. https://repository.tudelft.nl/islandora/object/uuid:c9c89827-59c5-4e52-9e0f-69800d20ce6a?collection=research

Tang, F., Li, Z., Tang, Y., Chen, Y., & Li, H.-N. (2020). Simultaneous measurement of shrinkage and coefficient of thermal expansion of mortar based on efpi sensors with nanometer resolution. *Measurement*, *152*, 107376. https://doi.org/https://doi.org/10.1016/j.measurement.2019.107376

van der Veen, C. (1990). *Cryogenic bond stress slip relationship*. Meinema, https://repository.tudelft.nl/islandora/object/uuid:f8cc71a0-ce17-4961-949f-aa110d9288a1?collection=research

Van Tittelboom, K., Gruyaert, E., Rahier, H., & De Belie, N. (2012). Influence of mix composition on the extent of autogenous crack healing by continued hydration or calcium carbonate formation [Non Destructive Techniques for Assessment of Concrete]. *Construction and Building Materials*, *37*, 349–359. https://doi.org/https://doi.org/10.1016/j.conbuildmat.2012.07.026

van Breugel, K., Braam, C., van der Veen, C., & Walraven, J. (2011, July). *Concrete structures under imposed thermal and shrinkage deformations*.

Windisch, A. (2021). The tensile strength: The most fundamental mechanical characteristics of concrete. *Concrete Structures*, *22*, 1–4. https://doi.org/10.32970/CS.2021.1.1

Wu, H., & Gilbert, R. (2008). An experimental study of tension stiffening in reinforced concrete members under short-term and long-term loads. https://www.researchgate.net/publication/265221757_An_Experimental_Study_of_Tension_Stiffening_in_Reinforced_Concrete_Members_under_Short-Term_and_Long-Term_Loads

Xue, W., Zhang, H., Li, H., & Xu, W. (2021). Effect of early age loading on the subsequent mechanical and permeability properties of concrete and its mechanism analysis. *Journal of Materials Research and Technology*, *14*, 1208–1221. https://doi.org/https://doi.org/10.1016/j.jmrt.2021.07.051

Yilmaz, F. (2022). Crack width of reinforced concrete structures under imposed deformations. https://repository.tudelft.nl/islandora/object/uuid:a1b84a8b-d86a-44c7-bbef-8abc85a8a137?collection=education

Zeng, Q., Li, K., Fen-Chong, T., & Dangla, P. (2012). Effect of porosity on thermal expansion coefficient of cement pastes and mortars. *Construction and Building Materials*, *28*(1), 468–475. https://doi.org/https://doi.org/10.1016/j.conbuildmat.2011.09.010

Zhang, H. (2011). Chapter 4 - cement. In *Building materials in civil engineering* (pp. 46–423). Woodhead Publishing. https://doi.org/https://doi.org/10.1533/9781845699567.46

A
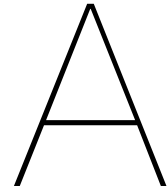
Autogenous shrinkage

This appendix includes the three graphs of the total measured ADTM deformation divided into thermal deformation and autogenous deformation for all three experiments. The thermal deformation has been calculated by determining the CTE as shown in subsection 5.1.2 and the autogenous shrinkage then follows from subtracting the thermal deformation from the total ADTM deformation.
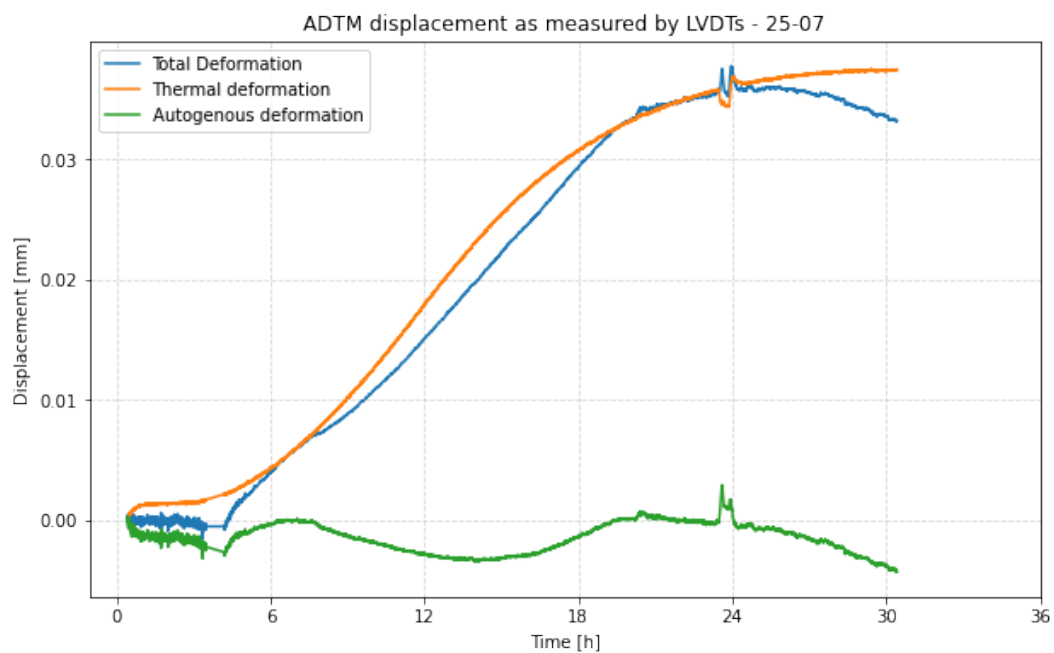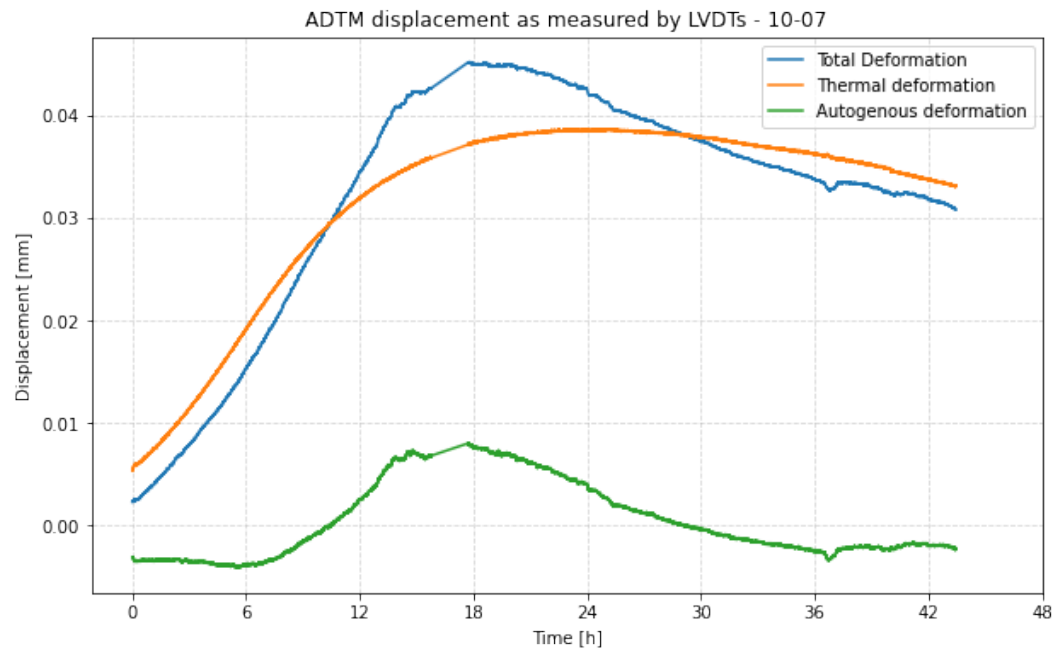

Figure A.1: Autogenous shrinkage of experiment 1

Figure A.2: Autogenous shrinkage of experiment 2
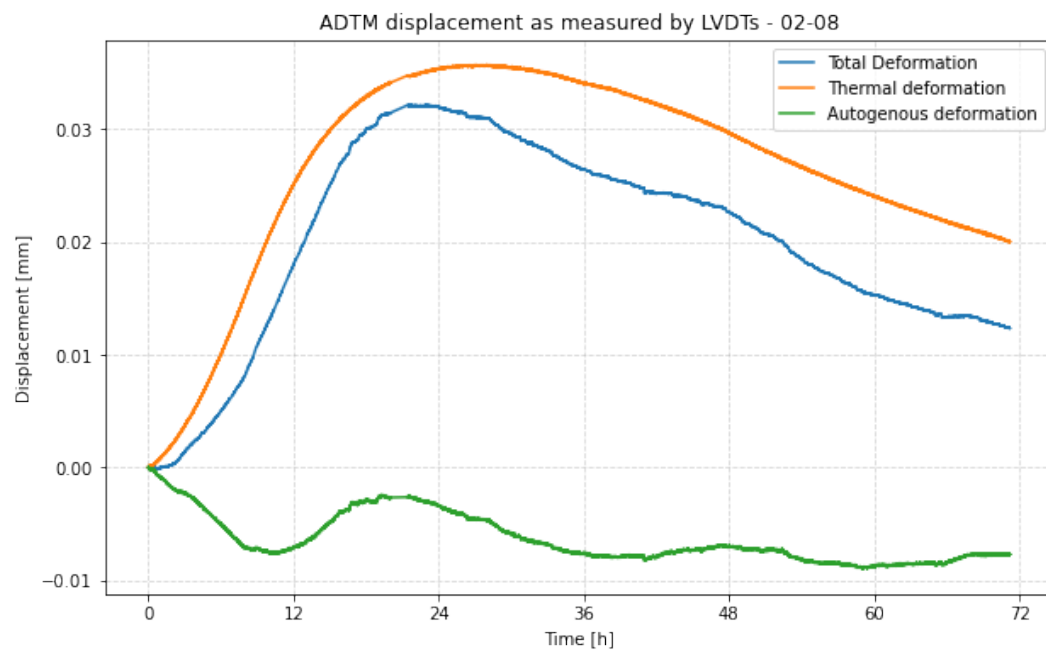
Figure A.3: Autogenous shrinkage of experiment 3

B

Crack width prediction calculations

Crack width predictions have been made for two stages during the experiments: during the crack formation stage and at a load of 10 kN after the mechanical test. NEN-EN 1992-3 and CIRIA C766 are not applicable for the final stage of the experiment. The following calculations are the prediction of each structural design code and guideline for the first experiment during the crack formation stage. The translation to the 10 kN stage is not complicated: the empirical factors of Model Code 2010 (see figure 3.6) are equal for both stages and the calculations for NEN-EN 1992-1-1 are almost identical as well, apart from the actual steel stress. Van Breugel uses a separate equation for the stabilized cracking stage, this expression is based on the crack width during the crack formation stage and the actual steel stress (see equation 3.30). Since this equation is notably different compared to the crack width during the crack formation stage, this calculation has been added to this appendix as well. The crack width values found in the calculations below can be found in table 5.5 in the row of experiment 1.

B.1. NEN-EN 1992-1-1

The maximum distance between cracks can be determined using the following equation according to NEN-EN 1992-1-1:

$$s_{r,max} = k_3 c + \frac{k_1 k_2 k_4 \emptyset}{\rho_{p,eff}}$$

(B.1)

where:

k_3 = 3.4 [-]
c = 12.5 [mm]
k_1 = 0.8 [-]
k_2 = 1.0 [-]
k_4 = 0.425 [-]
$\emptyset$ = 2.459 [mm]
$\rho_{p,eff}$ = $\frac{A_s}{A_c - A_s}$ = 0.11529 [-]
$s_{r,max}$ = 115.02 [mm]

The mortar stress at cracking for the first experiment equals:

$$\sigma_{cr} = \frac{F_{cr}}{A_c}$$

$$= \frac{5872 \ [N]}{2500 \ [mm^2]} \tag{B.2}$$

$$= 2.35 \ [N/mm^2]$$

The average tensile strength of the mortar can be determined using the relationship of Van Breugel:

$$f_{ctm}(t) = \frac{4}{3}\sigma_{cr}(t)$$

$$\tag{B.3}$$

$$= 3.13 \ [N/mm^2]$$

The characteristic tensile strength, mean tensile strength and elastic modulus are obtained using the relationships of NEN-EN 1992-1-1:

$$f_{ck} = \frac{f_{ctm}^{3/2}}{0.3}$$

$$\tag{B.4}$$

$$= 18.47 \ [N/mm^2]$$

$$f_{cm} = f_{ck} + 8$$

$$\tag{B.5}$$

$$= 26.47 \ [N/mm^2]$$

$$E_{cm} = 22 * \left(\frac{f_{cm}}{10}\right)^{0.3} * 1000$$

$$\tag{B.6}$$

$$= 29462 \ [N/mm^2]$$

The ratio between the elastic moduli of the steel and mortar, α_e is then known:

$$\alpha_e = \frac{E_s}{E_c}$$

$$\tag{B.7}$$

$$= 6.96 \ [-]$$

The steel stress at the moment of interest equals the final applied load divided by the area of steel. The applied load for the first new crack in the DIC analysis equals 8017 N and the area of steel is known because of its inner diameter:

$$\sigma_s = \frac{F_{cr}}{A_s}$$

(B.8)

$$= 281.4 \ [N/mm^2]$$

The difference in strain between the mortar and steel according to NEN-EN 1992-1-1 is therefore:

$$\varepsilon_{sm} - \varepsilon_{cm} = \frac{\sigma_s - k_t \frac{f_{ct,eff}}{\rho_{p,eff}}(1 + \alpha_e \rho_{p,eff})}{E_s}$$

(B.9)

$$= 0.0005136 \ [mm/mm]$$

Lastly, the strain difference between the mortar and steel is multiplied with the maximum distance between cracks to obtain the predicted crack width for the first experiment using NEN-EN 1992-1-1:

$$w_k = s_{r,max}(\varepsilon_{sm} - \varepsilon_{cm})$$

(B.10)

$$= 0.059 \ [mm]$$

B.2. NEN-EN 1992-3

The maximum distance between cracks can be determined using same equation as the one from NEN-EN 1992-1-1:

$$s_{r,max} = k_3 c + \frac{k_1 k_2 k_4 \emptyset}{\rho_{p,eff}}$$

(B.11)

where:

k_3	=	3.4 [-]
c	=	12.5 [mm]
k_1	=	0.8 [-]
k_2	=	1.0 [-]
k_4	=	0.425 [-]
$\emptyset$	=	2.459 [mm]
$\rho_{p,eff}$	=	$\frac{A_s}{A_c - A_s}$ = 0.11529 [-]
$s_{r,max}$	=	115.02 [mm]

The mortar stress at cracking for the first experiment equals:

$$\sigma_{cr} = \frac{F_{cr}}{A_c}$$

$$= \frac{5872 \ [N]}{2500 \ [mm^2]}$$

(B.12)

$$= 2.35 \ [N/mm^2]$$

The average tensile strength of the mortar can be determined using the relationship of Van Breugel:

$$f_{ctm}(t) = \frac{4}{3}\sigma_{cr}(t)$$

(B.13)

$$= 3.13 \ [N/mm^2]$$

The characteristic tensile strength, mean tensile strength and elastic modulus are obtained using the relationships of NEN-EN 1992-1-1:

$$f_{ck} = \frac{f_{ctm}^{3/2}}{0.3}$$

(B.14)

$$= 18.47 \ [N/mm^2]$$

$$f_{cm} = f_{ck} + 8$$

(B.15)

$$= 26.47 \ [N/mm^2]$$

$$E_{cm} = 22 * \left(\frac{f_{cm}}{10}\right)^{0.3} * 1000$$

(B.16)

$$= 29462 \ [N/mm^2]$$

The ratio between the elastic moduli of the steel and mortar, α_e is then known:

$$\alpha_e = \frac{E_s}{E_c}$$

(B.17)

$$= 6.96 \ [-]$$

The factors k_c and k are given in NEN-EN 1992-1-1 and the first one equals 1.0 for a pure tensile stress distribution. The factor k is also equal to 1.0 as the stresses are uniform throughout the cross-section. The difference in strain between the mortar and steel according to NEN-EN 1992-3 equals:

$$(\varepsilon_{sm} - \varepsilon_{cm}) = \frac{0.5\alpha_e k_c k f_{ct,eff}}{E_s}\left(1 + \frac{1}{\alpha_e \rho}\right)$$

(B.18)

$$= 0.0007157 \ [mm/mm]$$

And finally the crack width is found by multiplying the maximum spacing between two cracks with

the strain difference found above:

$$w_k = s_{r,max}(\varepsilon_{sm} - \varepsilon_{cm})$$

$$= 0.082 \; [mm]$$

(B.19)

B.3. Model Code 2010

Model Code 2010 uses the following expression to calculate crack widths:

$$w_d = 2l_{s,max}(\varepsilon_{sm} - \varepsilon_{cm} - \varepsilon_{cs})$$

(B.20)

The first part of the expression, $l_{s,max}$, is the the length over which slip between concrete and steel occurs and is calculated as follows:

$$l_{s,max} = k * c + \frac{1}{4} * \frac{f_{ctm}}{\tau_{bms}} * \frac{\varphi_s}{\rho_{s,ef}}$$

(B.21)

The factor k takes the influence of the concrete cover into consideration and may be assumed to be 1.0 according the Model Code. The average tensile strength of the mortar can be determined using the relationship of Van Breugel:

$$f_{ctm}(t) = \frac{4}{3}\sigma_{cr}(t)$$

$$= 3.13 \; [N/mm^2]$$

(B.22)

The mean bond strength between steel and concrete, τ_{bms}, for long term loading and the stabilized cracking stage equals:

$$\tau_{bms} = 1.8 * f_{ctm}$$

$$= 5.64 \; [N/mm^2]$$

(B.23)

The effective steel ratio in the cross-section is also present in both Eurocode 2 norms and equals:

$$\rho_{s,ef} = \frac{A_s}{A_c - A_s}$$

$$= 0.011529 \; [-]$$

(B.24)

The cover c = 12.5 mm and the diameter of the reinforcement ϕ_s equals 2.459 mm. Equation B.21 can then be filled in:

$$l_{s,max} = 42.1 \ [mm] \tag{B.25}$$

The relative mean strain, meaning the strain difference between concrete and steel over the length $l_{s,max}$, can be determined as follows (note that the shrinkage equals zero, as the mechanical test is regarded as a short term test, $\eta_r / = /0$):

$$\varepsilon_{sm} - \varepsilon_{cm} - \varepsilon_{cs} = \frac{\sigma_s - \beta * \sigma_{sr}}{E_s} - \eta_r * \varepsilon_{sh} \tag{B.26}$$

The steel stress at the moment of interest equals the applied load when the crack occurred divided by the area of steel.

$$\sigma_s = \frac{F_{cr}}{A_s}$$
$$\tag{B.27}$$
$$= 281.4 \ [N/mm^2]$$

The coefficients β and η_r depend on the load duration and stage of the tensile member diagram, for short term loading in the crack formation stage they equal to 0.6 and 0 respectively. The maximum steel stress in a crack in the crack formation stage, for pure tension, is:

$$\sigma_{sr} = \frac{f_{ctm}}{\rho_{s,ef}} \left(1 + \alpha_e \rho_{s,ef} \right)$$
$$\tag{B.28}$$
$$= 296.6 \ [N/mm^2]$$

The strain difference between concrete and steel is then equal to:

$$\varepsilon_{sm} - \varepsilon_{cm} - \varepsilon_{cs} = \frac{\sigma_s - \beta * \sigma_{sr}}{E_s} - \eta_r * \varepsilon_{sh}$$
$$\tag{B.29}$$
$$= 0.0005045 \ [mm/mm]$$

Finally, the crack width for the first experiment predicted by Model Code 2010 is known:

$$w_d = 2l_{s,max}(\varepsilon_{sm} - \varepsilon_{cm} - \varepsilon_{cs})$$
$$\tag{B.30}$$
$$= 0.043 \ [mm]$$

B.4. CIRIA C766

The approach to directly calculate crack widths according to CIRIA C766 is almost identical to NEN-EN 1992-3. The maximum distance between cracks can be determined using:

$$s_{r,max} = k_3 c + \frac{k_1 k_2 k_4 \emptyset}{\rho_{p,eff}}$$ (B.31)

where:

k_3	=	3.4 [-]
c	=	12.5 [mm]
k_1	=	0.8 [-]
k_2	=	1.0 [-]
k_4	=	0.425 [-]
$\emptyset$	=	2.459 [mm]
$\rho_{p,eff}$	=	$\frac{A_s}{A_c - A_s}$ = 0.11529 [-]
$s_{r,max}$	=	115.02 [mm]

The strain difference between the reinforcing steel and mortar is not determined with the mean tensile strength of the mortar, but rather with 70% of the mean tensile strength ($f_{ctk,0.05}$):

$$(\varepsilon_{sm} - \varepsilon_{cm}) = \frac{0.5\alpha_e k_c k f_{ctk,0.05}}{E_s}\left(1 + \frac{1}{\alpha_e \rho}\right)$$ (B.32)

The mortar stress at cracking for the first experiment equals:

$$\sigma_{cr} = \frac{F_{cr}}{A_c}$$

$$= \frac{5872\ [N]}{2500\ [mm^2]}$$ (B.33)

$$= 2.35\ [N/mm^2]$$

The average tensile strength of the mortar can be determined using the relationship of Van Breugel:

$$f_{ctm}(t) = \frac{4}{3}\sigma_{cr}(t)$$ (B.34)

$$= 3.13\ [N/mm^2]$$

The characteristic tensile strength, mean tensile strength and elastic modulus are obtained using the relationships of NEN-EN 1992-1-1:

$$f_{ck} = \frac{f_{ctm}^{3/2}}{0.3}$$ (B.35)

$$= 18.47\ [N/mm^2]$$

$$f_{cm} = f_{ck} + 8$$

$$= 26.47 \ [N/mm^2]$$

(B.36)

$$E_{cm} = 22 * \left(\frac{f_{cm}}{10}\right)^{0.3} * 1000$$

$$= 29462 \ [N/mm^2]$$

(B.37)

The ratio between the elastic moduli of the steel and mortar, α_e is then known:

$$\alpha_e = \frac{E_s}{E_c}$$

$$= 6.96 \ [-]$$

(B.38)

The factors k_c and k are given in NEN-EN 1992-1-1 and the first one equals 1.0 for a pure tensile stress distribution. The factor k is also equal to 1.0 as the stresses are uniform throughout the cross-section. The difference in strain between the mortar and steel according to CIRIA C766:

$$(\varepsilon_{sm} - \varepsilon_{cm}) = \frac{0.5\alpha_e k_c k f_{ct,eff}}{E_s}\left(1 + \frac{1}{\alpha_e \rho}\right)$$

$$= 0.0005010 \ [mm/mm]$$

(B.39)

The crack width for the first experiment according to CIRIA is found by simply multiplying this strain difference with the maximum distance between two cracks:

$$w_k = s_{r,max}(\varepsilon_{sm} - \varepsilon_{cm})$$

$$= 0.058 \ [mm]$$

(B.40)

B.5. Van Breugel

Van Breugel's method starts with determining the mean crack width in the crack formation stage:

$$w_{m0} = 2 * \left(\frac{0.4\text{\O}}{f_{cm,cube}E_s} * \left(\frac{\sigma_{cr}}{\rho}\right)^2 * (1 + \alpha_e \rho)\right)^{0.85}$$

(B.41)

The mortar stress at cracking for the first experiment equals:

$$\sigma_{cr} = \frac{F_{cr}}{A_c}$$

$$= \frac{5872 \ [N]}{2500 \ [mm^2]} \tag{B.42}$$

$$= 2.35 \ [N/mm^2]$$

The average tensile strength of the mortar can be determined using the relationship of Van Breugel:

$$f_{ctm}(t) = \frac{4}{3}\sigma_{cr}(t) \tag{B.43}$$

$$= 3.13 \ [N/mm^2]$$

The characteristic tensile strength, mean tensile strength and elastic modulus are obtained using the relationships of NEN-EN 1992-1-1:

$$f_{ck} = \frac{f_{ctm}^{3/2}}{0.3} \tag{B.44}$$

$$= 18.47 \ [N/mm^2]$$

$$f_{cm} = f_{ck} + 8 \tag{B.45}$$

$$= 26.47 \ [N/mm^2]$$

$$E_{cm} = 22 * \left(\frac{f_{cm}}{10}\right)^{0.3} * 1000 \tag{B.46}$$

$$= 29462 \ [N/mm^2]$$

The ratio between the elastic moduli of the steel and mortar, α_e is then known:

$$\alpha_e = \frac{E_s}{E_c} \tag{B.47}$$

$$= 6.96 \ [-]$$

A minor difference compared to the other structural codes and guidelines is that Van Breugel does not take the effective steel ratio, but just the regular steel ratio:

$$\rho_{s,ef} = \frac{A_s}{A_c - A_s}$$

(B.48)

$$= 0.011398 \; [-]$$

$$w_{m0} = 2 * \left(\frac{0.4\text{\O}}{f_{cm,cube} E_s} * \left(\frac{\sigma_{cr}}{\rho} \right)^2 * (1 + \alpha_e \rho) \right)^{0.85}$$

(B.49)

$$= 0.034 \; [mm]$$

Next, the mean crack spacing should be determined and it equals:

$$\sigma_{s,cr} = \sigma_{cr} \left(\frac{1}{\rho} + \alpha_e \right)$$

(B.50)

$$= 222.4 \; [N/mm^2]$$

$$l_m = 1.8 w_{m0} \frac{E_s}{\sigma_{s,cr}}$$

(B.51)

$$= 56.5 \; [mm]$$

Now the mean crack width in the stabilized cracking stage can be determined:

$$\sigma_s = \frac{F_{cr}}{A_s}$$

$$= \frac{10000 \; [N]}{6 * \frac{1}{4}\pi * 2.459^2 \; [mm^2]}$$

(B.52)

$$= 350.9 \; [N/mm^2]$$

$$w_{mv} = 1.8 w_{m0} \left(\frac{\sigma_s}{\sigma_{s,cr}} - 0.5 \right)$$

(B.53)

$$= 0.066 \; [mm]$$

C

Crack reopening - Instron data

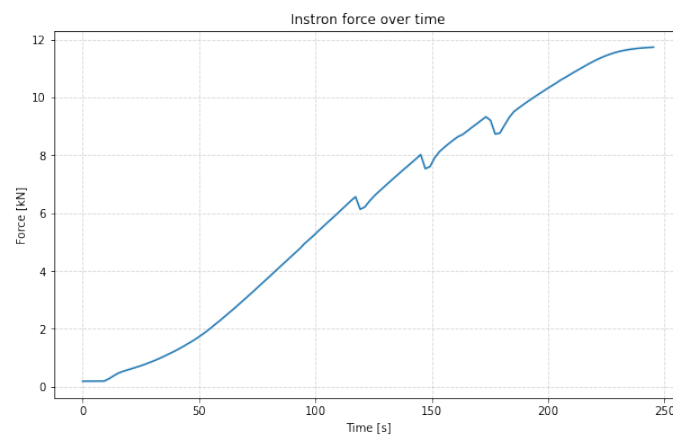## C.1. Experiment 1 - Zero imposed deformation cracks

Figure C.1: Force over time during the reopening of the TSTM cracks
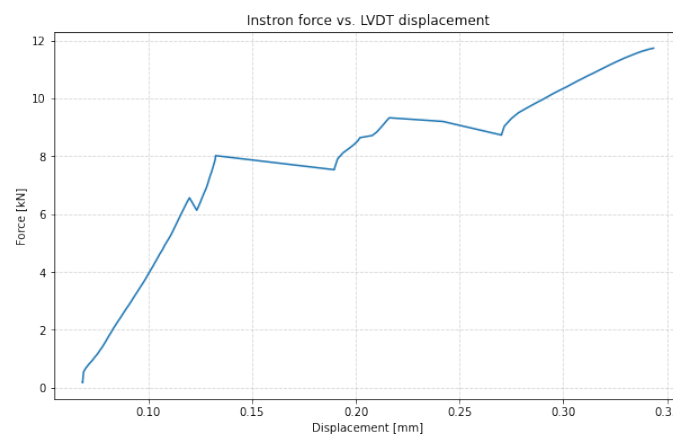

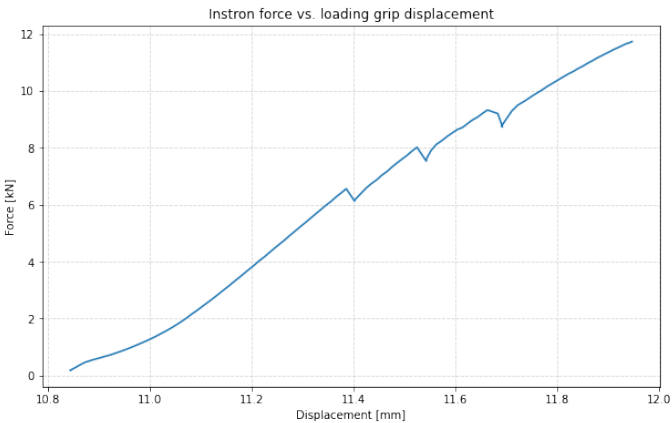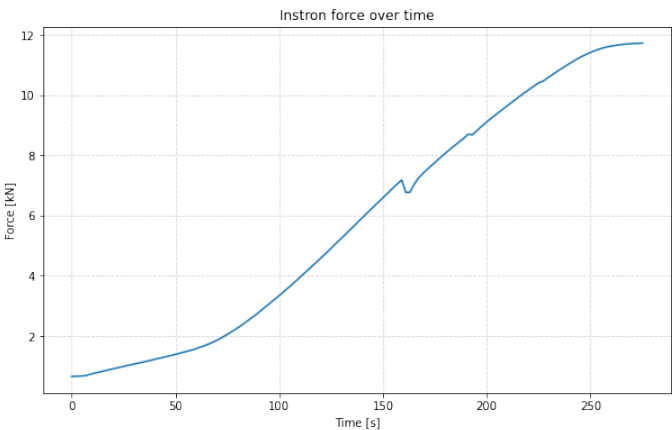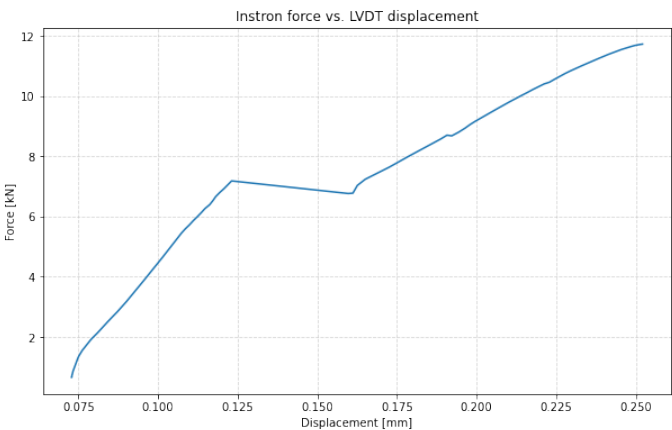**Figure C.2: Load vs LVDT displacement during the reopening of the TSTM cracks**

Figure C.3: Load vs loading grip displacement during the reopening of the TSTM cracks

C.2. Experiment 3 - Two imposed deformation cracks

Figure C.4: Force over time during the reopening of the TSTM cracks

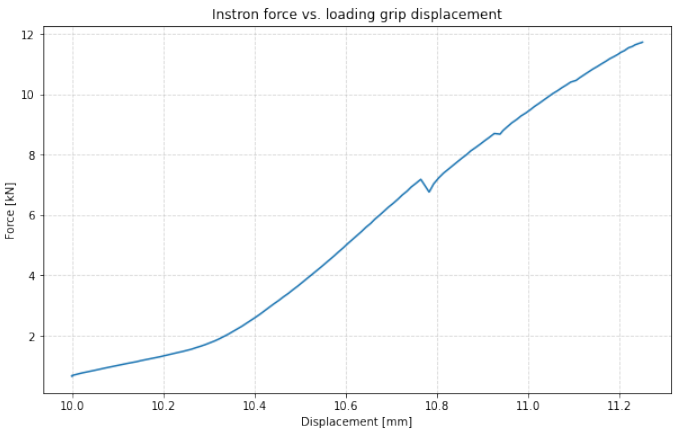**Figure C.5: Load vs LVDT displacement during the reopening of the TSTM cracks**

Figure C.6: Load vs loading grip displacement during the reopening of the TSTM cracks